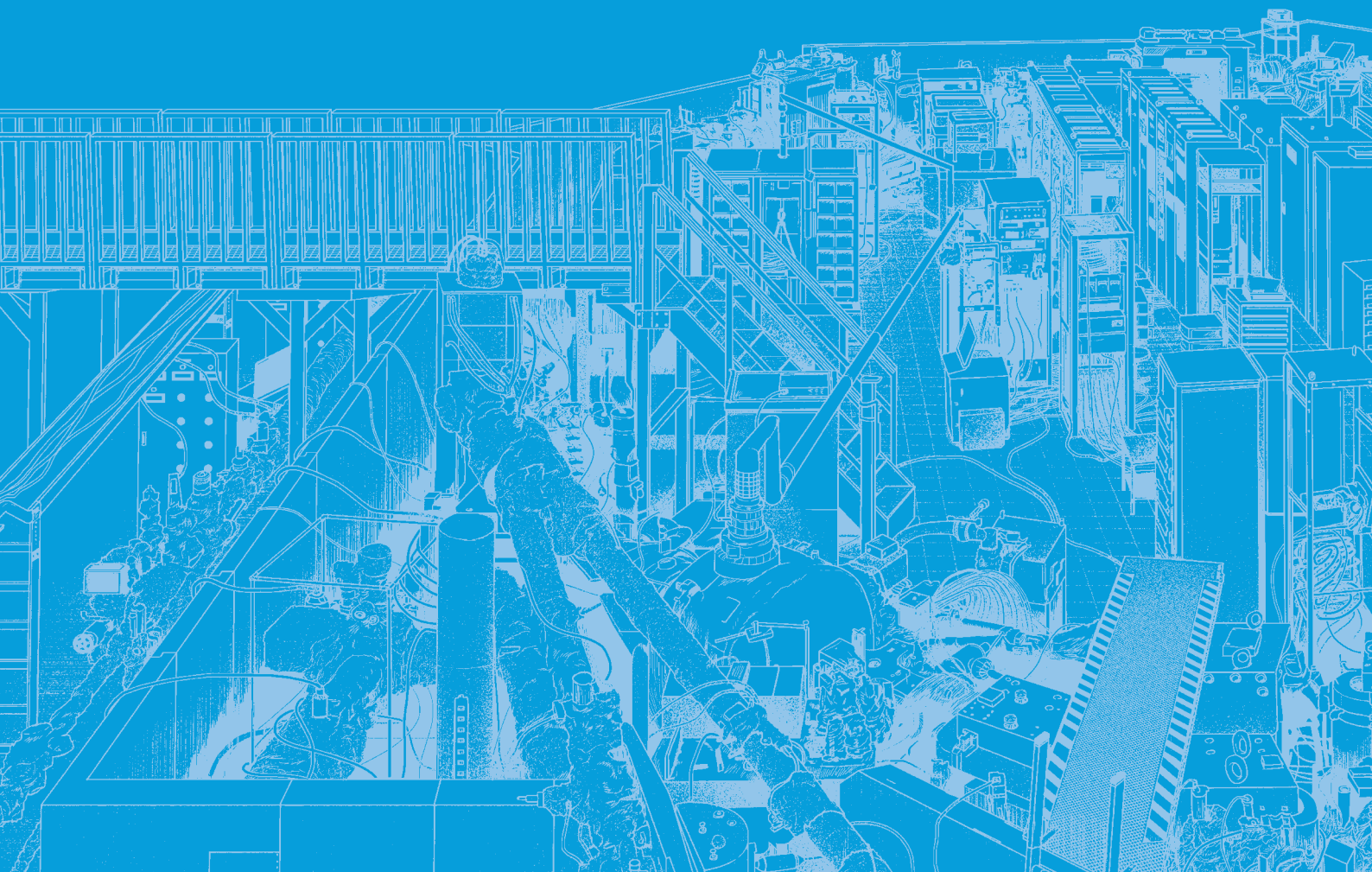


III-2

Material Sciences





BL6B

Anisotropy in the Far-Infrared Absorption Davydov Doublet of the Single-Crystal Pentacene

Y. Nakayama^{1,2}, K. Yamauchi¹, Y. Baba¹ and J. Miyamoto¹¹Department of Pure and Applied Chemistry, Tokyo University of Science, Noda 278-8510, Japan²Institute for Molecular Science (IMS), Okazaki 444-8585, Japan

Accurate knowledge of the vibrational properties of solid-state molecules is a crucial demand to understanding polaronic charge carrier transport phenomena in organic semiconductors [1], and thus the vibrational characteristics of pentacene have been studied extensively. For instance, Pinterić *et al.* recently reported their very fine results on temperature-dependent variation of the infrared absorption properties of the pentacene single-crystals (PnSCs) to reveal influences of the electron-phonon couplings to the excitonic characters [2]. Nevertheless, a complete understanding of the vibrational characteristics peculiar to the single-crystal phase of this molecule has not yet been achieved. In the present work, we focused on two unique properties for the single-crystals of pentacene, that is, the orientation dependence and vibrational Davydov splitting, and attempted to clarify these characteristics by azimuthal-angle (ϕ) dependent analyses of the Fourier transform infrared absorption (FT-IR) spectroscopy.

Details for the samples measured and experimental conditions were reported elsewhere [3]. The FT-IR measurements were conducted at BL6B of UVSOR. All the results presented here were obtained by using a Si bolometer and at room temperature.

Figure 1(a) shows the IR absorbance of PnSC. As seen in Fig. 2(a), the peak positions of these two were independent of ϕ , while the intensities of these were complementary to each other. Although these two peaks were originally assigned to two individual vibrational modes [4], present results showing a good agreement of

experimental “major”/“minor” intensity ratios with the theoretical calculation (Fig. 2(b)) strongly suggest that these two peaks were originated from the Davydov splitting of one vibrational mode.

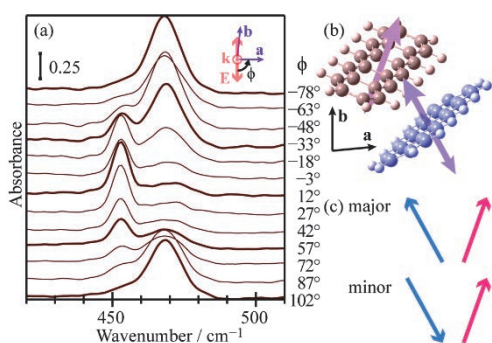


Fig. 1. (a) IR absorbance of PnSC depending on ϕ . (b) Molecular orientation and transition dipole directions of the vibration mode (#15) for the PnSC(001) surface molecules. (c) Relationships of the transition dipoles for the “major” and “minor” Davydov components.

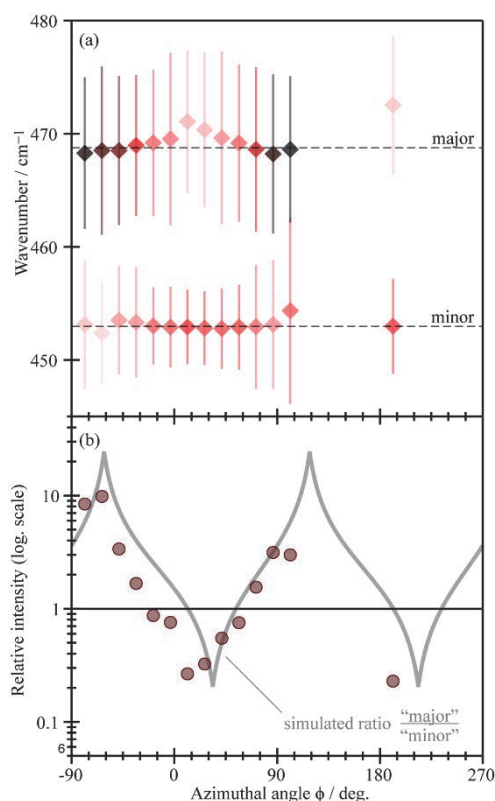


Fig. 2. (a) Wavenumber positions of the two peaks shown in Fig. 1(a) plotted as a function of ϕ . The peak intensity is indicated as the color tone (light: small; dark: large). (b) Intensity ratios of the two peaks (“major”/“minor”) plotted as circle symbols. The simulated intensity ratio of the two Davydov components for a vibrational mode with a transition dipole directions perpendicular to the molecular plane is also drawn with a gray curve.

- [1] V. Coropceanu *et al.*, *Chem. Rev.* **107** (2007) 926.
 [2] M. Pinterić *et al.*, *J. Mater. Chem. C* **10** (2022) 5582.
 [3] Y. Nakayama *et al.*, *Vib. Spectrosc.* **132** (2024) 103681.
 [4] K. Michaelian *et al.*, *Vib. Spectrosc.* **58** (2012) 50.

Change in Positron Lifetime of Deformed Pure Iron before and after Unloading Tensile Stress

M. Fujinami¹, R. Awaji¹, H. Abe¹, A. Yabuuchi², T. Hirade³, N. Oshima⁴ and Y. Taira⁵

¹Department of Applied Chemistry and Biotechnology, Chiba University, Chiba 263-8522, Japan

²Institute for Integrated Radiation and Nuclear Science, Kyoto University, Kumatori 590-0494, Japan

³Nuclear Science and Engineering Center, Japan Atomic Energy Agency, Tokai 319-1195, Japan

⁴National Institute of Advanced Industrial Science and Technology, Tsukuba 305-8568, Japan

⁵UVSOR Synchrotron Facility, Institute for Molecular Science, Okazaki 444-8585, Japan

The study of lattice defects in metals formed by plastic deformation is important for controlling metals' mechanical properties. Positron annihilation lifetime spectroscopy (PALS) is a powerful tool for investigating vacancy-type defects in metals [1]. However, measuring the positron lifetime of metals during deformation using a conventional PALS technique is difficult. Therefore, in most previous studies, the positron lifetimes of deformed metals were measured after the deformation stress was unloaded. The characteristics of defects in metals may change due to the unloading of deformation stresses. In this study, we measured the positron lifetime of pure iron using a gamma-ray-induced PALS (GiPALS) technique [2], which can easily measure the positron lifetime of metals during deformation.

As shown in Fig. 1, we installed a small tensile tester at the BL1U beamline. A well-annealed pure iron tensile test piece with a purity of 99.99 % was attached to the tensile tester. The thickness and gauge width of the test piece were 3 mm and 6 mm, respectively. Positron lifetimes were measured while the test piece was being elongated. Furthermore, positron lifetimes after elongation to ~7 % nominal strain were measured, both before and after tensile stress unloading.

The mean positron lifetime of pure iron investigated by in-situ measurements during tensile deformation increased with increasing nominal strain. The GiPALS technique was shown to be an easy way to measure changes in the positron lifetime of metals during deformation. Figure 2 shows the results of a two-component analysis of the positron lifetime of pure iron elongated to ~7 % nominal strain, measured before and after tensile stress unloading. The defect component intensity, I_2 (intensity of the longer positron lifetime component), increases significantly by unloading the tensile stress. Furthermore, the positron lifetime of the defect component (the longer positron lifetime component) also changes significantly. This indicates that the defects were formed by the unloading of tensile stress. In other words, the defect structure in structural materials actually used under stress cannot be revealed by observation after the stress is unloaded. One needs to recognize the importance of measuring lattice defects under actual usage conditions of the material.

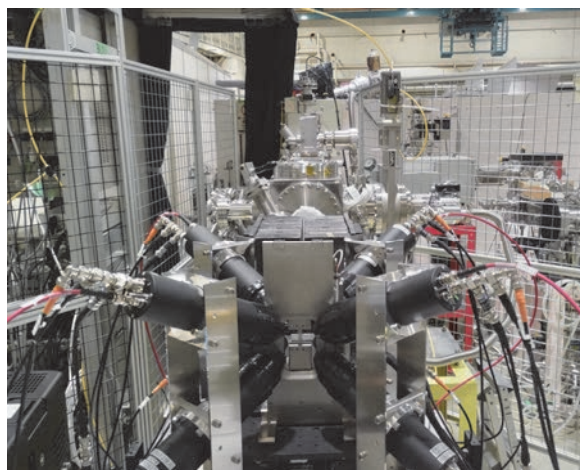


Fig. 1. Photo of a small tensile tester installed at the BL1U beamline. A tensile test piece is attached to the center of the eight scintillation detectors.

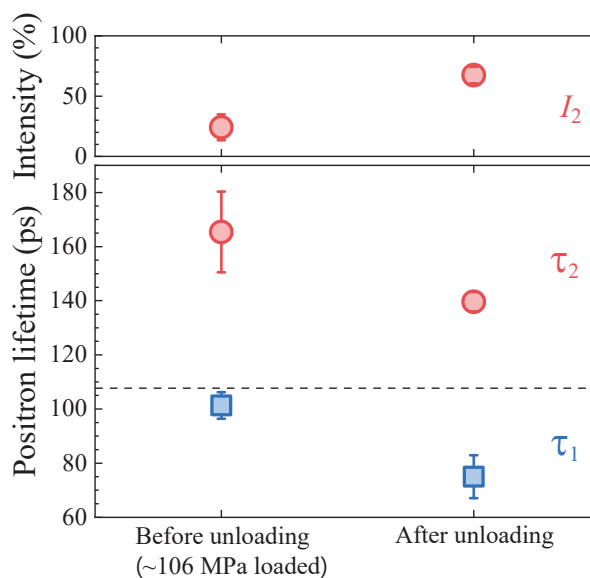


Fig. 2. Positron lifetimes of pure iron elongated to ~7 % nominal strain. The left and right sides were measured before and after tensile stress unloading, respectively.

[1] R. W. Siegel, *Annu. Rev. Mater. Sci.* **10** (1980) 393.

[2] Y. Taira *et al.*, *Rev. Sci. Instrum.* **93** (2022) 113304.

BLIU

Changes of the Gamma-ray Induced Positron Annihilation Lifetimes for CeO₂ by Desorption and Re-adsorption of Surface Adsorption Species

S. Dohshi¹, K. Maeda¹, Y. Taira² and T. Hirade³

¹Osaka Research Institute of Industrial Science and Technology 2-7-1, Ayumino, Izumi, Osaka 594-1157, Japan

²UVSOR Synchrotron Facility, Institute for Molecular Science, Okazaki 444-8585, Japan

³Japan Atomic Energy Agency, Ibaraki 319-1195, Japan

Cerium oxide (CeO₂) catalyst utilizes active oxygen species adsorbed on the surface oxygen defects to oxidize toluene. Temperature programmed desorption measurements have reported that active oxygen species (O₂) adsorbed on oxygen defects of cerium oxide surface desorbs at 150 °C, which initiates the oxidation reaction of toluene [1].

Gamma-ray-induced positron annihilation lifetime spectroscopy (GiPALS) measurements were conducted on CeO₂ at room temperature in air. The lifetime components attributed to the surface were consistent with those of defect-free surface determined by first principles calculations. Active oxygen species adsorb on the surface oxygen defects before temperature programmed desorption, resulting in few trapped positrons in these defects. However, after temperature programmed desorption, the adsorbed active oxygen species are expected to desorb, resulting in the emergence of oxygen defects on the surface and the creation of new positron trapping sites.

This study investigated the positron annihilation lifetimes of two operations: (1) the removal of surface adsorbed species by heating CeO₂ under an argon flow, and (2) the subsequent re-adsorption of surface adsorbed species under a water vapor-containing air flow.

The pellet sample with 20 mm in diameter and 10 mm in thickness were prepared using CeO₂ nanoparticles with a primary particle size of ca. 2 nm. In this experiment, the pellets were heated in a quartz tube at a rate of 5 °C/min using a jacket heater under argon (purity: 99.999%) flow to 200 °C and held for 2 h. After cooling under argon flow, a GiPALS measurement was performed. Subsequently, air containing water vapor was flowed through at a rate of 200 mL/min for 1 h at room temperature, followed by another GiPALS measurement.

We have set up a gamma-ray spectroscopy system at the laser-Compton scattering (LCS) beamline of BLIU at UVSOR-III [2], and measured the lifetime of the annihilation gamma-rays at room temperature using BaF₂ scintillation detector. We used the software Lifetime9 (LT9) to analyze the spectra.

Figure 1 shows the positron annihilation lifetime

spectra of CeO₂ measured under different conditions. The positron annihilation lifetime becomes longer when CeO₂ was heated at 200 °C. Previous research has shown that heating CeO₂ at this temperature causes the desorption of active oxygen species adsorbed on oxygen defects on the surface, while lattice oxygen remains unaffected [1]. In short, the longer positron annihilation lifetime is believed to result from the emergence of oxygen defects on the surface caused by the desorption of active oxygen species. Additionally, the positron annihilation lifetime spectrum was observed to return to its original state when air containing water vapor was introduced, possibly due to the re-adsorption of oxygen and/or water vapor on the surface oxygen defects.

In the next fiscal year, we plan to conduct a detailed study on the adsorption species present on the oxygen defects on the surface.

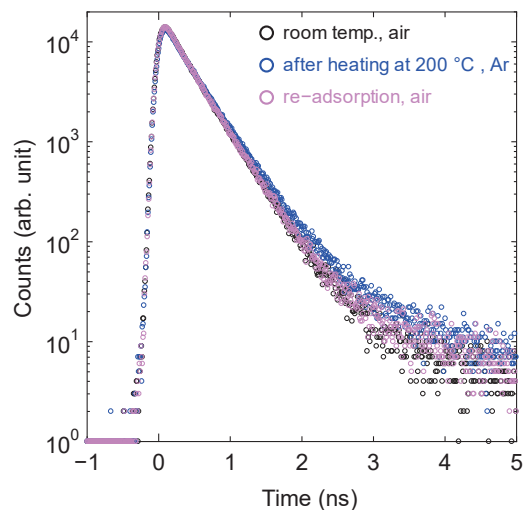


Fig. 1. Positron annihilation lifetime spectra of CeO₂ measured under different conditions. (a) at room temperature in air, (b) after heating at 200 °C for 2 h in Ar, (c) re-adsorption of surface adsorbed species under a water vapor-containing air flow for 1 h.

- [1] L. Wang *et al.*, Catal. Sci. Technol. **6** (2016) 4840.
 [2] Y. Taira *et al.*, Rev. Sci. Instrum. **84** (2013) 053305.

GiPALS Study of $\text{Ca}_2\text{MgSi}_2\text{O}_7:\text{Eu,Dy}$ Long-Persistent Phosphorescence Phosphors

M. Kitaura¹, H. Masai², S. Watanabe³ and Y. Taira^{4,5}

¹Faculty of Science, Yamagata University, Yamagata 990-8560, Japan

²Department of Materials and Chemistry, National Institute of Advanced Industrial Science and Technology, Ikeda 563-8577, Japan

³Innovative Technology Laboratories, AGC Inc., Yokohama 230-0045, Japan

⁴UVSOR Synchrotron Facility, Institute for Molecular Science, Okazaki 444-8585, Japan

⁵School of Physical Sciences, The Graduate University for Advanced Studies, Okazaki 444-8585, Japan

Multinary compounds have been widely used as commercial products. These compounds are difficult to obtain stoichiometric compositions. Especially, the addition of impurities causes non-stoichiometric compositions, because it requires defects such as vacancies or interstitials for charge compensation when they are incorporated into host materials. Such a non-stoichiometry affects physical and chemical properties of multinary compounds.

Gamma-ray-induced positron annihilation lifetime spectroscopy (GiPALS) is an atomic scale micro-probe to observe vacancy-type defects in solids [1]. GiPALS studies of multicomponent garnet scintillators activated with Ce^{3+} ions have been performed so far to investigate the mechanism on the occurrence of a persistent phosphorescence in the Ce^{3+} 5d-4f emission [2,3]. It was turned out that the persistent phosphorescence occurs under non-stoichiometric compositions due to the introduction of Al vacancy at 16a and 24d sites. This finding was significant to improve luminescence properties of the multicomponent garnet scintillators. In contrast, non-stoichiometry compositions may be favorable for long persistent phosphorescence phosphors, but it remains unclear whether non-stoichiometry is indispensable for the long persistent phosphorescence.

$\text{Ca}_2\text{MgSi}_2\text{O}_7:\text{Eu,Dy}$ is known to be long persistent phosphorescence phosphors. In this material, it was pointed out that oxygen and magnesium vacancies are introduced as native defects which work as electron and hole reservoirs [4,5]. Because of charge compensation, such vacancy-type defects may be introduced more by the codoping of Dy ions at the Ca site. A positron probe such as GiPALS is a unique tool to investigate the existence of the vacancy-type defects. In the present study, GiPALS experiment was performed to demonstrate whether they are included in $\text{Ca}_2\text{MgSi}_2\text{O}_7:\text{Eu,Dy}$.

The GiPALS spectrum of a $\text{Ca}_2\text{Mg}_2\text{SiO}_7:\text{Eu,Dy}$ is shown in Fig. 1. The spectrum consists of two exponential decay components, as indicated by broken lines. The positron annihilation lifetimes τ_i and relative intensities I_i of the two components are listed in Table 1. The relative intensities of two components are comparable. The bulk lifetime was analyzed by

assuming the two-state trapping model in which positrons annihilate at the bulk and defect states. The bulk lifetime was determined to be 265 ± 8 ps. This value was different from the bulk lifetime ($=232$ ps) determined by a first principles calculation based on the density-functional theory. The short lifetime component may not be simply linked to the positron annihilation at the bulk state. Further investigations are needed to identify the origins of the short and long lifetime components in $\text{Ca}_2\text{MgSi}_2\text{O}_7:\text{Eu,Dy}$.

A part of this study was financially supported by JSPS KAKENHI grant (No. 21H05546).

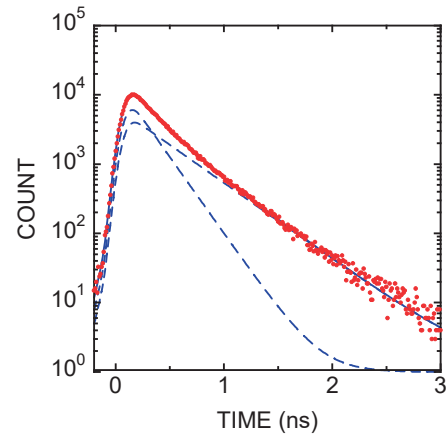


Fig. 1. GiPALS spectrum of a $\text{Ca}_2\text{MgSi}_2\text{O}_7:\text{Eu,Dy}$ crystal measured at 300 K.

Table 1. Positron annihilation lifetimes and relative intensities obtained from the curve-fit analysis of GiPALS spectrum for a $\text{Ca}_2\text{MgSi}_2\text{O}_7:\text{Eu,Dy}$.

τ_1 (ps)	I_1 (%)	τ_2 (ps)	I_2 (%)
197 ± 5	48.6 ± 1.5	395 ± 5	51.4 ± 1.5

[1] Y. Taira *et al.*, Rev. Sci. Instrum. **33** (2006) 1.

[2] M. Kitaura *et al.*, Appl. Phys. Express **13** (2020) 085505.

[3] M. Kitaura *et al.*, Opt. Mater.: X **14** (2022) 100156.

[4] J. Holsa *et al.*, J. Rare Earths **29** (2011) 1130.

[5] H. Duan *et al.*, J. Phys. D: Appl. Phys. **49** (2016) 025304.

BLIU

Gamma-ray Induced Positron Annihilation Lifetime Spectroscopy of As-Doped CdTe

T. Sumi¹, M. Kitaura¹, A. Nagaoka², Y. Taira^{3,4}, H. Masai⁵ and K. Kimura⁶

¹Faculty of Science, Yamagata University, Yamagata 990-8560, Japan

²Faculty of Engineering, University of Miyazaki, Miyazaki 889-2192, Japan

³UVSOR Synchrotron Facility, Institute for Molecular Science, Okazaki 444-8585, Japan

⁴School of Physical Sciences, The Graduate University for Advanced Studies, Okazaki 444-8585, Japan

⁵Department of Materials and Chemistry, National Institute of Advanced Industrial Science and Technology, Ikeda, Osaka 563-8577, Japan

⁶Department of physical Science and Engineering, Nagoya Institute of Technology, Nagoya 466-8555, Japan

Cadmium tellurides (CdTe) attract much attention as a solar cell substance. Group V (P, As, Sb) doping is an effective manner to improve carrier concentration and mobility in CdTe, realizing in high conversion efficiency over 20 % [1]. Despite the accumulation of experimental and theoretical studies conducted in the past, the physical mechanism of group V doping has not yet been cleared. Group V doping introduces various types of defects such as interstitials, vacancies, and complexes, owing to the charge compensation for them. However, detailed information on the correlation between these defects and group V doping is not available, because the formation of defects by group V doping is influenced by chemical environments in material synthesis and crystal growth.

Native defects in CdTe have been identified by theoretical calculations. According to defect formation energies [2], the vacancy at the Cd site (V_{Cd}) and the As atom at the Cd site (As_{Cd}) are stable as isolated native defects. V_{Cd} - As_{Cd} defect complexes was also stable under the Cd-rich condition, but it became unstable under the Te-rich condition. It is never easy to optimize defect properties to obtain the CdTe based photovoltaic device with high conversion efficiency.

Positron annihilation lifetime spectroscopy (PALS) is a unique experimental technique that can observe charged vacancies such as V_{Cd} defects in CdTe. PALS studies have been performed for undoped and impurity-doped CdTe [3]. To our knowledge, PALS experiment has not yet reported for As-doped CdTe. It is worthwhile to investigate whether isolated V_{Cd} and/or As_{Cd} defects are changed in As doping. In the present study, gamma-ray induced positron annihilation lifetime spectroscopy (GiPALS) was performed using As-doped CdTe polycrystal, which was synthesized in sealed quartz ampoules from high-temperature melt of As-doped CdTe. The amount of the As impurity was determined to be $5 \times 10^{17} \text{ cm}^{-3}$. The positron annihilation lifetime was analyzed using the program LT9 [4].

Figure 1 shows the GiPALS spectrum of the As-doped CdTe polycrystal, which was measured at 300 K. The GiPALS spectrum is reproduced by the sum of exponential decay functions. The lifetimes were determined to be $123 \pm 37 \text{ ps}$ and $294 \pm 2 \text{ ps}$ by the curve

fit analysis. The intensity of the long lifetime component ($=4.4 \pm 1.6 \%$) is larger than that of the short lifetime component ($=95.6 \pm 1.6 \%$). Assuming the two-state trapping model of bulk and defect states, the positron annihilation lifetime at the bulk state was determined to be $277 \pm 14 \text{ ps}$, which was in good agreement with the bulk lifetime ($=278 \text{ ps}$) calculated by a first-principles calculation based on the density-functional theory. The lifetime of the long lifetime component was almost agreement with the calculated positron annihilation lifetime for the V_{Cd} defect ($=300 \text{ ps}$). The long lifetime component is assigned to the positron annihilation at the V_{Cd} defect. Further experimental and theoretical studies are required to investigate the effect of As-doping on defects in CdTe.

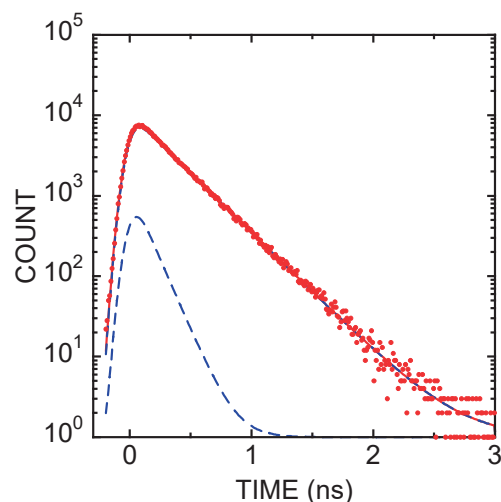


Fig. 1. GiPALS spectrum of As-doped CdTe polycrystals, measured at 300 K.

- [1] W. K. Metzger *et al.*, Nat. Energy **4** (2019) 837.
- [2] A. Nagaoka *et al.*, J. Am. Chem. Soc. **145** (2023) 9191.
- [3] M. R. Elsharkawy *et al.*, Appl. Phys. Lett. **108** (2016) 242102.
- [4] J. Kansy and D. Giebel, J. Phys.: Conf. Ser. **265** (2011) 012030.

Study on Evaluation of Material Defects by Positron Annihilation Method Using Ultrashort Pulsed Gamma Rays

Y. Takashima^{1,2}, N. Kishimoto² and Y. Taira³

¹Synchrotron Radiation Research Center, Nagoya University, Nagoya 464-8603, Japan

²School of Engineering, Nagoya University, Nagoya 464-8603, Japan

³UVSOR Synchrotron Facility, Institute for Molecular Science, Okazaki 444-8585, Japan

The positron annihilation method (PAS), which is effective in diagnosing defects in materials, is a method to estimate the type and amount of defects by irradiating positrons to the material and measuring the gamma rays generated by annihilation with electrons in the material. The positron annihilation method using gamma rays (GiPAS) generated by Compton scattering of a laser with the circulating electrons in a storage ring makes it possible to evaluate defects inside metallic materials with a thickness of a few millimeters.

The specimen to be evaluated in this study is interstitial-free (IF) steel, which is widely used as steel sheets for automobiles. From the viewpoint of safety as an automotive steel plate, it is extremely important to understand the formation and growth process of defects that occur during plastic deformation.

Gamma ray induced positron annihilation lifetime spectroscopy (GiPALS) on IF steels subjected to 10% nominal strain was performed at UVSOR in 2021 and reported the existence of single vacancy-type lattice defects [1,2]. In this study, positron lifetime measurements for IF steels subjected to 5%, 10%, and 15% tensile strain were performed to clarify the mechanism of void formation from single vacancy-type defects during plastic deformation and to gain insight into strain-induced changes of defects.

The experiment was conducted at BLIU of UVSOR. The gamma rays generated by the collision of a short-pulse laser with an electron beam orbiting in the storage ring were irradiated onto IF steels, and the two gamma rays generated by positron annihilation at 180 degrees were detected by four opposing pairs of BaF₂ detectors. The positron annihilation lifetime was measured by capturing the signals from the detectors into an oscilloscope. Figure 1 shows the photographs of the experimental setup.

In order to investigate the growth process of defects when IF steel is subjected to strain, GiPALS measurements were performed on IF steel with 0%, 5%, 10%, and 15% strain introduced. The IF steels were provided by Professor Adachi, Assistant Professor Chen and Mr. Sawai of the Graduate School of Engineering, Nagoya University. The obtained data were analyzed using LT9, an analysis software mainly used for positron lifetime analysis. As a preliminary analysis, fitting was performed on a function with a two-component lifetime.

Table 1 shows the preliminary results. It was observed

that the first component of lifetime τ_1 increased as the amount of strain increased. No significant change was observed in the second component of lifetime τ_2 . From these results, it can be inferred that the effect on the τ_1 component may increase as the amount of strain increases. Future work may include analysis of different lifetime components by fitting with three or more lifetime value components, removal of defects by annealing prior to tensile testing, and measurement of samples exposed to even greater strain.

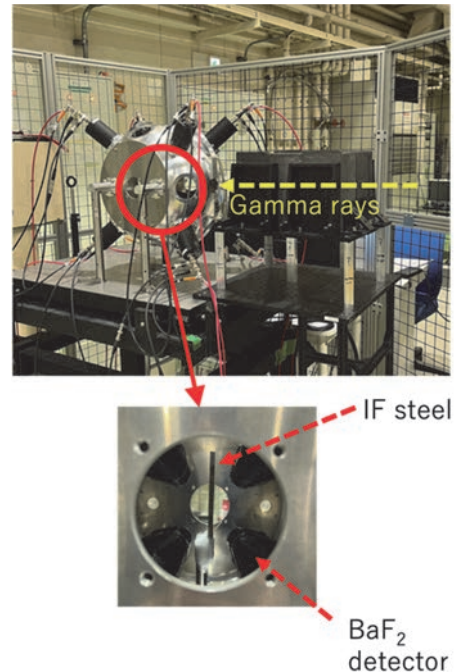


Fig. 1. Photographs of the experimental setup.

Table 1. Lifetime components τ_1 and τ_2 for IF steel with 0 %, 5 %, 10 %, and 15 % strain introduced.

	0%	5%	10%	15%
τ_1 (ps)	99.6 ±1.4	107 ±3.0	120 ±3.5	129 ±3.6
τ_2 (ps)	203 ±4.2	188 ±4.1	198 ±6.2	205 ±9.0

[1] R. Yamamoto, Master thesis of Graduate School of Engineering, Nagoya University (Feb. 2022).

[2] Y. Taira *et al.*, Rev. Sci. Instrum. **93** (2022) 113304.

Change in Positron Lifetime of Tungsten Caused by Electrolytic Hydrogen Charging

A. Yabuuchi¹, T. Hirade², R. Awaji³, M. Fujinami³,
N. Oshima⁴, K. Saito⁵, K. Takai⁵ and Y. Taira⁶

¹Institute for Integrated Radiation and Nuclear Science, Kyoto University, Kumatori 590-0494, Japan

²Nuclear Science and Engineering Center, Japan Atomic Energy Agency, Tokai 319-1195, Japan

³Department of Applied Chemistry and Biotechnology, Chiba University, Chiba 263-8522, Japan

⁴National Institute of Advanced Industrial Science and Technology, Tsukuba 305-8568, Japan

⁵Department of Engineering and Applied Sciences, Sophia University, Tokyo 102-8554, Japan

⁶UVSOR Synchrotron Facility, Institute for Molecular Science, Okazaki 444-8585, Japan

Tungsten is a candidate material for plasma-facing walls in fusion reactors. The presence of vacancies in tungsten will trap tritium, fuel for fusion reactors. Incorporating tritium into tungsten is problematic from the standpoints of radioactivity management and the economics of power reactors. A study based on theoretical calculations by Ohsawa *et al.* claims that hydrogen induces the formation of vacancies in tungsten [1]. This study investigated hydrogen-induced vacancies in tungsten using gamma-ray-induced positron annihilation lifetime spectroscopy (GiPALS) [2].

Eight 10 mm square samples were cut from a 0.8-mm-thick tungsten plate with a purity of 99.999%. They were then annealed in a vacuum at around 2200 °C for 15 min using an electron bombardment heating technique. The annealed samples were preliminarily measured by conventional positron annihilation lifetime spectroscopy using a ²²Na positron source sealed with Kapton foils. Four of the eight samples were immersed in 0.1 mol/L NaOH solution containing 5 g/L NH₄SCN as cathode, and electrolytic hydrogen charging was performed for 10 days with a current density of 5 mA/cm². The uncharged and hydrogen-charged samples were measured using the GiPALS technique to obtain positron annihilation lifetime spectra. Four sheets of samples were stacked in each measurement to acquire a sufficient counting rate.

Figures 1 and 2 show positron annihilation lifetime spectra of uncharged and hydrogen-charged samples. Positron lifetime components other than the defect-free bulk component were observed in both samples. Therefore, both spectra were analyzed by fitting with two positron lifetime components. Comparing the preliminary analysis results shown in Figs. 1 and 2, the positron lifetime of the second component (the longer lifetime component) becomes shorter by hydrogen charging while its intensity increases. This change may result from mixing the second component with positron lifetime components of vacancies or vacancy-hydrogen complexes with positron lifetimes of less than 200 ps. However, the origin of the longer positron lifetime component observed in the uncharged sample must be elucidated to show the change caused by the hydrogen charging clearly. The GiPALS measurement found for

the first time the longer positron lifetime component (342 ps ± 39 ps) observed in the uncharged sample. This longer positron lifetime is close to the positron lifetime of Kapton (~380 ps) and could not be detected by a conventional ²²Na source method because it is indistinguishable from the source component.

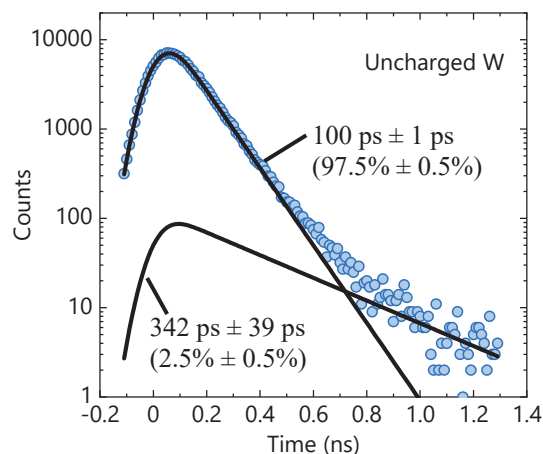


Fig. 1. Positron annihilation lifetime spectrum of the uncharged sample.

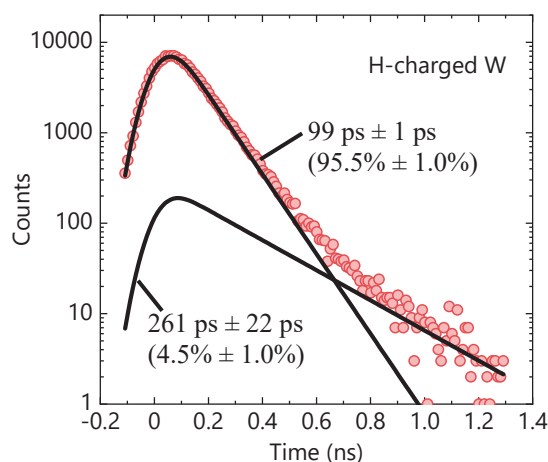


Fig. 2. Positron annihilation lifetime spectrum of the H-charged sample.

[1] K. Ohsawa *et al.*, J. Nucl. Mater. **458** (2015) 187.

[2] Y. Taira *et al.*, Rev. Sci. Instrum. **93** (2022) 113304.

Attempts for Intermolecular Phonon Measurement of High Mobility Organic Semiconductors by Terahertz Absorption Spectroscopy

K. Yamauchi¹, Y. Baba¹ and Y. Nakayama^{1,2}

¹Department of Pure and Applied Chemistry, Tokyo University of Science, Noda 278-8510, Japan

²Institute for Molecular Science (IMS), Okazaki 444-8585, Japan

Intramolecular and intermolecular vibrations are factors that reduce charge carrier mobility in organic semiconductors, and thus transport characteristics in the organic electronic devices are strongly affected by molecular vibrations. Therefore, understanding and controlling of the molecular vibrations are essential for highly efficient organic semiconductor devices. Our group previously elucidated intramolecular vibrational properties on the single crystal pentacene, which is known as a p-type organic semiconductor exhibiting considerable charge carrier mobility, in far- to mid-infrared range at BL6B, UVSOR [1-4]. In this study, we tried to identify intermolecular vibrations, which are predicted to appear in the THz region [5-7], by performing infrared absorption spectroscopy measurements in a lower wavenumber range on the single crystals of representative organic semiconductors dinaphthothienothiophene (DNTT), pentacene (Pn), and rubrene (Rub).

Single crystals of DNTT, Pn, and Rub were prepared by physical vapor transport and were fixed onto diamond substrates. Infrared absorption spectroscopy measurements were performed using a Si bolometer (General Purpose 4.2 K Bolometer, IRLabs, Inc.), a wire grid beam splitter capable of detecting in the 0 - 120 cm^{-1} measurement range, and in a transmission configuration in a high vacuum (10^{-5} Pa) chamber. Measurements were also performed on a diamond substrate without the molecular crystal as a reference sample. For the Fourier transform, the Blackman function was used to correct the integration range.

Figure 1 shows the IR signal intensity through each sample (diamond, DNTT/diamond, Pn/diamond, and Rub/diamond). The intensity dropped sharply below 20 cm^{-1} and above 100 cm^{-1} , indicating that the substantial region in these measurements was 20 – 100 cm^{-1} . From the data shown in Fig. 1, the absorbance of each molecular crystal sample was determined using the Lambert-Beer formula as shown in Fig. 2, where the light intensity transmitted through the diamond substrate without and with the molecular crystals was assigned to I_0 and I , respectively. No peaks were seen in the measured wavenumber region for any of the molecular samples, and thus intermolecular vibrations could not be identified. This may be ascribed to the insufficient transmittance of the THz photon through

the organic semiconductor single crystal samples relative to that through the diamond substrate. Another possible cause is the low intensity of the incident THz light itself.

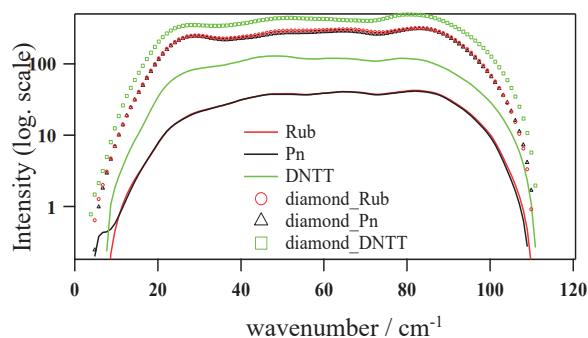


Fig. 1. THz transmission intensity of each sample.

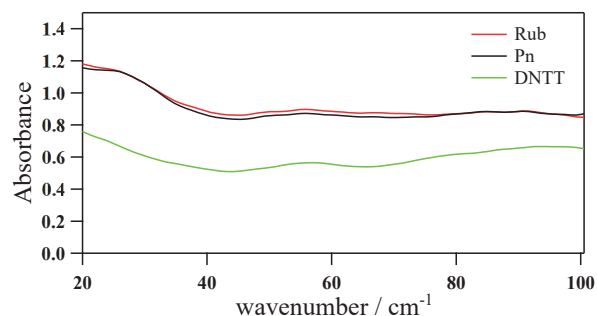


Fig. 2. THz absorbance of each molecular single crystal sample obtained using the Lambert-Beer formula for the transmission signals shown in Fig. 1.

- [1] Y. Nakayama *et al.*, Vib. Spectrosc. **132** (2024) 103601.
- [2] Y. Nakayama *et al.*, UVSOR Activity Report **50** (2023) 104.
- [3] J. Miyamoto *et al.*, UVSOR Activity Report **49** (2021) 91.
- [4] Y. Nakayama, J. Miyamoto, UVSOR Activity Report **48** (2021) 83.
- [5] A. Girlando *et al.*, Phys. Rev. B: Condens. Matter **82** (2010) 035208.
- [6] A. Girlando *et al.*, J. Chem. Phys. **135** (2011) 084701.
- [7] G. Schweicher *et al.*, Adv. Mater. **31** (2019) 1902407.

BL2A

Local Structure of Catalytically Active Mo-Carbide Species on H-MFI Zeolites for Methane Aromatization at High Pressure

K. Kuramochi¹, A. Kosuge², Y. Sonobe¹, Y. Uchimura¹ and H. Aritani²

¹Advanced Science Research Laboratory, Saitama Institute of Technology, Fukaya 369-0293, Japan

²Graduate School of Engineering, Saitama Institute of Technology, Fukaya 369-0293, Japan

As a typical catalyst for GTL (Gas-To-Liquid), molybdenum- modified H-MFI zeolite (Mo/H-MFI) shows high MTB (Methane To Benzene; $6\text{CH}_4 \rightarrow \text{C}_6\text{H}_6 + 9\text{H}_2$) reactivity for methane dehydroaromatization at 973–1073 K. Although the MTB process using a highly active catalyst is an innovative reaction one for direct conversion from natural gas into petroleum resources, definite deactivation of the catalyst during the reaction is a fatal drawback. And thus, clarification of the deactivation factor over the Mo/H-MFI catalysts is one of the important points for study. A cause of the deactivation strongly depends on both coke deposition onto strong acid sites over H-MFI, as well as structural deactivation of carbonized Mo species.[1] One of the most important subjects for catalytically high and durable activity is the elucidation of active Mo-carbide (MoC_x) sites. Recently, it has been found that the reaction at high pressure (up to 0.2 MPa) achieved both high activation and suppression of deactivation. As a result, a revolutionary improvement in the MTB reaction can be expected. In this study, Mo L_{III} -edge XANES is applied to characterize the active MoC_x species on Mo/H-MFI after the MTB reaction under 0.1–0.2 MPa.

Mo(5wt%)/H-MFI ($\text{Si}/\text{Al}_2=23\text{--}50$) catalysts were prepared as described in the previous paper.[1] Each catalyst (0.5 g) has been pre-reduced with $\text{CO}(2\%)\text{-He}$ at 1023 K for 1 h. The reactivity of methane dehydroaromatization was evaluated by the reaction with $\text{CH}_4(20\%)\text{+H}_2(2\%)\text{+He}$ at 1023 K under 0.10–0.20 MPa. Mo L_{III} -edge XANES spectra were obtained in BL2A of UVSOR-III in a total-electron yield mode using InSb double-crystal monochromator. A REX-2000 (Rigaku) software was employed for normalization of each XANES spectrum.

As a result of the catalytic MTB activity over Mo/H-MFI ($\text{Si}/\text{Al}_2=23$ and 50), the reactivity increased with increasing the pressure (up to 0.20 MPa) of the MTB reaction over both catalysts. A remarkable effect of suppression on deactivation was shown in $\text{Si}/\text{Al}_2=50$ reacted under high pressure. Fig. 1 shows the Mo L_{III} -edge XANES spectra of Mo/H-MFI catalysts after MTB reaction at 1023 K under 0.10–0.20 Pa. In case of Mo/H-MFI ($\text{Si}/\text{Al}_2=23$) catalysts shown in the top of Fig. 1, XANES spectra of reference compounds ($\alpha\text{-Mo}_2\text{C}$, $\beta\text{-Mo}_2\text{C}$, and Mo metal) are also shown. After the reaction under 0.10 MPa (atmospheric pressure), it is likely that $\alpha\text{-Mo}_2\text{C}$ (cubic) species are formed after MTB reaction. In contrast, $\beta\text{-Mo}_2\text{C}$ (orthorhombic) like species are possibly formed after

the reaction under 0.15–0.20 Pa. Since the $\beta\text{-Mo}_2\text{C}$ phase can be formed by the deep carburization of the $\alpha\text{-Mo}_2\text{C}$, [2] formation of $\beta\text{-Mo}_2\text{C}$ species is suggested to be one of the factors for the high activity imparted by the reaction under high pressure. In case of Mo/H-MFI ($\text{Si}/\text{Al}_2=50$) catalysts shown in the bottom of Fig. 1, α - and β - phases are possibly formed after the reaction under 0.10 MPa. Under high pressure (0.15–0.20 MPa), it is concluded the $\beta\text{-Mo}_2\text{C}$ species are formed after the reaction. From the XANES results, it is concluded that reductively carbonized Mo species to $\beta\text{-Mo}_2\text{C}$ is one of a key role in high MTB reactivity. For deep reduction, H_2 co-feed with CH_4 needs for high MTB reactivity.

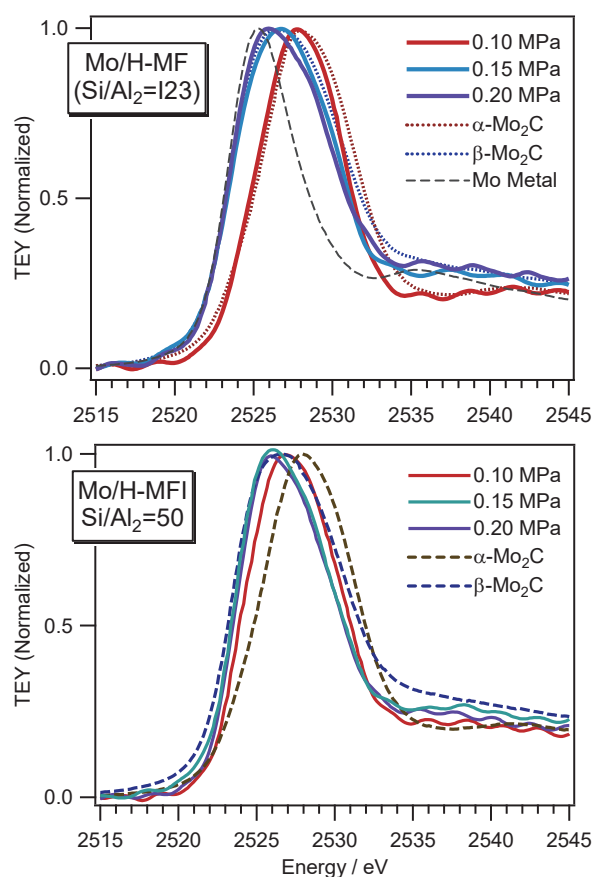


Fig. 1. Mo L_{III} -edge XANES spectra of Mo/H-MFI ($\text{SiO}_2/\text{Al}_2\text{O}_3=23$ [top] and 50 [bottom]) catalysts after MTB reaction at 1023 K under 0.10–0.20 Pa.

[1] H. Aritani *et al.*, J. Environ. Sci. **21** (2009) 736.

[2] K. Wu *et al.*, Ind. Eng. Chem. Res. **58** (2019) 20270.

X-ray Absorption Near Edge Structure Analysis of Deintercalation of Ni-Al Layered Double Hydroxide Dense Bodies

H. Murata, K. Yone and A. Nakahira

Department of Materials Science, Osaka Metropolitan University, Sakai 599-8531, Japan

Layered double hydroxides (LDH) are crystalline hydroxides which contain divalent and higher valence cations in the hydroxide layers. The higher valence cations cause intercalation of counter anions between the hydroxide layers as charge compensation. These intercalated anions lead to variety of applications such as ion-exchange hosts, ion-conductor and electrochromic device. [1-3] LDHs are available in various forms, such as nano-particles, powders, and thin films. Since LDHs decompose at high temperature, dense bodies cannot be obtained by usual sintering.

Hydrothermal hot-pressing method (HHP) is one of the low-temperature sintering techniques. In this method, a green body containing a small amount of aqueous solution is compressed and heated. The aqueous solution is then released from the green body with the dissolution and re-precipitation of the samples, which connects particles. This method produce dense bodies of thermally unstable materials such as zeolite. [4]

In this study, dense bodies of Ni-Al LDH were prepared by HHP and their deintercalation behaviors were investigated using X-ray absorption near edge structure (XANES).

Ni-Al LDH dense bodies were prepared by the hydrothermal hot-pressing method. A starting material was Ni-Al LDH powder synthesized from aqueous solutions by the co-precipitation method. This starting material was mixed with 5 mol/L NaOH aqueous solution, which is 20 wt% of the starting material. The samples were compressed at 40 MPa and 150 °C for 2 h. The deintercalation of the samples were performed by heat treatment at 300 °C for 2 h.

Obtained dense bodies were characterized by Archimedes method, X-ray diffraction (XRD), Fourier transform infrared spectroscopy (FT-IR) and X-ray absorption near edge structure (XANES). Ni-L₃ and Al-K XANES were collected by the total electron yield method with sample current and the partial fluorescent method using a silicon drift detector. Samples were mounted on metal plates using carbon tape.

The HHP process produced translucent dense bodies of Ni-Al LDH. XRD patterns of the samples shows a strong preferred orientation along 00 l reflections, which means that layered structure is well aligned in the dense bodies. Comparing with density by Archimedes method and crystalline density calculated from lattice parameters, the obtained Ni-Al LDH dense bodies

achieved full density (over 95 %). The shape of the dense bodies was maintained after heating at 300°C. The XRD patterns of the samples after heat treatment were assigned to low crystallinity rocksalt-type NiO.

Figure 1 shows Ni-L₃ and Al-K XANES spectra of the samples. Ni in the samples were maintained Ni²⁺ at octahedral site after thermally deintercalation. On the other hand, the Al-K XANES of the thermally deintercalated samples have additional shoulder peak at lower energy than the white line. This is attributed to Al³⁺ at tetrahedral site. Therefore, Al³⁺ plays an important role in deintercalation of LDH.

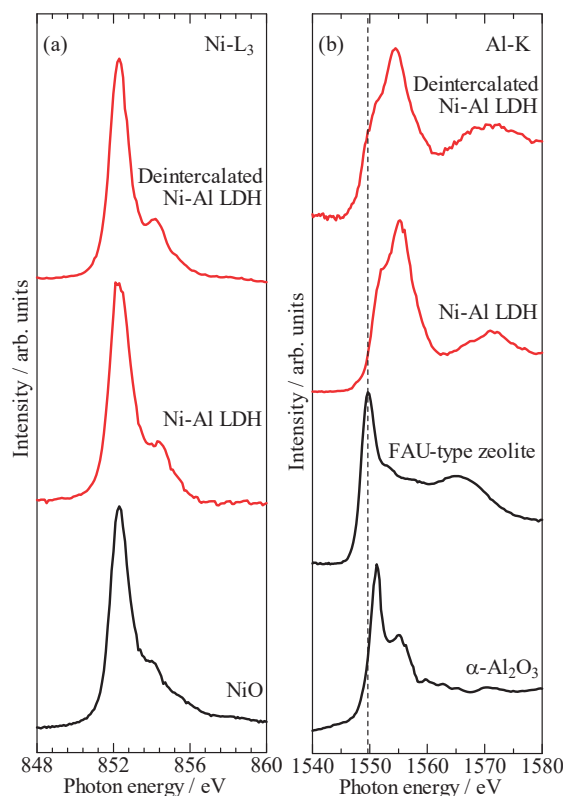


Fig. 1. (a) Ni-L₃ and (b) Al-K XANES of Ni-Al LDH dense bodies.

- [1] G. Mishra *et al.*, *Appl. Clay Sci.* **153** (2018) 172.
- [2] K. Tadanaga *et al.*, *Adv. Mater.* **22** (2010) 4401.
- [3] P. Koilraj *et al.*, *ACS Appl. Nano Mater.* **3** (2020) 6552.
- [4] A. Nakahira *et al.*, *J. Am. Ceram. Soc.* **90** (2007) 2322.

BL2A

Local Structure Investigations of Zincate Spinels

S. Yoshioka¹, E. Kobayashi² and K. Okudaira³

¹*Department of Applied Quantum Physics and Nuclear Engineering, Kyushu University, Fukuoka 819-0395, Japan*

²*Kyushu Synchrotron Light Research Center, Saga 841-0005, Japan*

³*Graduate school of Advanced Integration Science, Chiba University, Chiba 263-8522, Japan*

Spinel oxides with the general formula AB_2O_4 can be formed with various kinds of divalent A and trivalent B cations. Owing to their unique mechanical, electronic, and magnetic properties, the spinel oxides have gained considerable attention not only from the fundamental research fields but also from the industrial application point of view. Some spinel compounds such as $MgAl_2O_4$ accommodate large degrees of cationic disorder. $MgAl_2O_4$ spinel shows relative higher inversion degree $i = 0.15$ to 0.35 , whereas zincate spinels such as $ZnAl_2O_4$ generally show small amount of cationic disorder degrees. However, their local structures have not been fully understood. X-ray absorption spectroscopy (XAS) is a powerful structure characterization method that uses an X-ray probe to reveal local atomic coordination and electronic structures. In this study, we focus on the local structures around Zn in zincate spinels, $ZnAl_2O_4$ and $ZnFe_2O_4$.

Polycrystalline sample of $ZnAl_2O_4$ and the single crystal of $ZnFe_2O_4$ sample were used in this study. Zn $L_{2,3}$ -edge XANES measurements were performed on BL2A beamline at UVSOR Synchrotron Facility, Okazaki, Japan, using the partial fluorescence yield method. A $KTiOPO_4$ double-crystal monochromator gives Zn $L_{2,3}$ -absorption edges in the energy regions 1010–1070 eV. The measurements of Zn $L_{2,3}$ -edge XANES spectra were carried out in vacuum at a pressure and temperature of 1×10^{-4} Pa and $20^\circ C$, respectively. Fluorescence X-rays of Zn $L\alpha$ were collected utilizing an energy-dispersible silicon drift detector.

The Zn $L_{2,3}$ -edge XANES spectra for $ZnAl_2O_4$ and $ZnFe_2O_4$ are shown in Fig. 1. The spectrum of powder ZnO was also shown as reference spectra. The intensity of each spectrum was normalized to a value of 1 at the photon energy of 1065 eV after the removal of the background intensity. The spectra of both spinels show clear difference from that of ZnO. The Zn $L_{2,3}$ -edge XANES of $ZnAl_2O_4$ have peaks A – D as well as that of $ZnFe_2O_4$, however, their shapes and relative intensity were clearly different. Detailed analyses on the local environment of Zn and in the $ZnAl_2O_4$ and $ZnFe_2O_4$ are in progress by combined use of the XANES and the first principles band structure calculations.

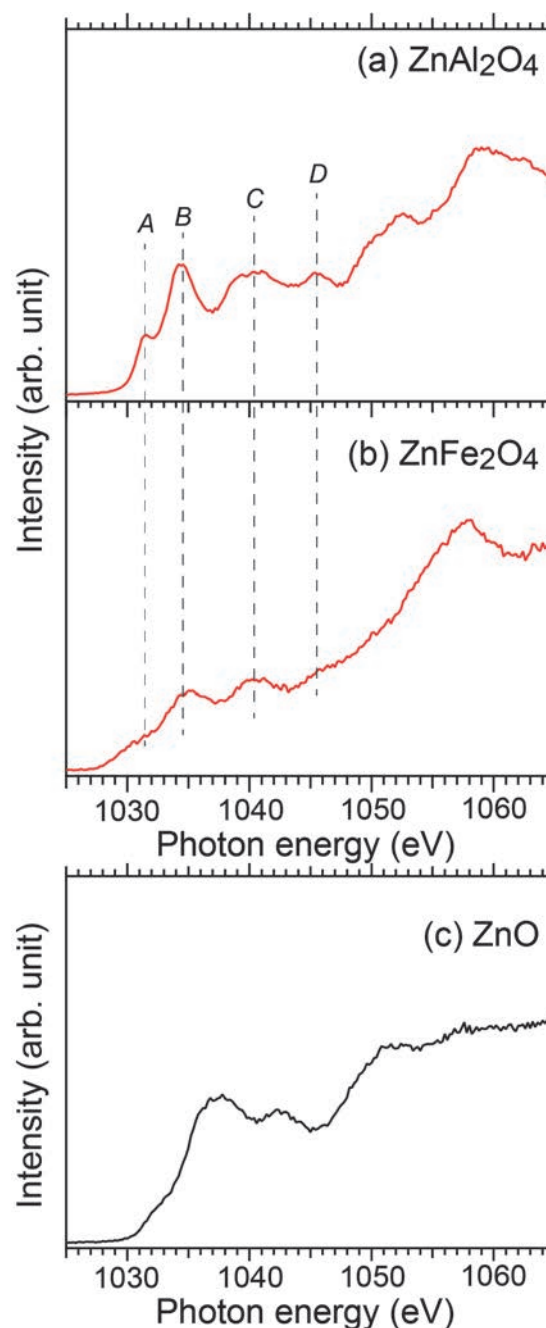


Fig. 1. Zn $L_{2,3}$ -edge XANES spectra of $ZnAl_2O_4$ (a) and $ZnFe_2O_4$ (b). Spectrum of ZnO (c) was shown as a reference.

Direct Observation of 4-Layer Structure in the Chiral SmC Variant Phase Delicate Balance of Ferroelectricity and Antiferroelectricity by Resonant Soft X-ray Scattering (RSoXS) at UVSOR

Y. Takanishi¹, F. Araoka² and H. Iwayama^{3,4}

¹Department of Physics, Kyoto Prefectural University of Medicine,
1-5, Shimogamohangi-cho, Sakyo, Kyoto 606-0823, Japan

²RIKEN Center for Emergent Matter Science, Hirosawa 2-1, Wako, Saitama 351-0198, Japan

³UVSOR Synchrotron Facility, Institute for Molecular Science, Okazaki 444-8585, Japan

⁴School of Physical Sciences, The Graduate University for Advanced Studies (SOKENDAI),
Okazaki 444-8585, Japan

The ferroelectricity and antiferroelectricity have been found in the tilted chiral smectic phases, called SmC* and SmC_A*, respectively. By competition of SmC* and SmC_A*, several phases with narrow temperature range were found, called subphases. Subphases have been defined as the relative ratio of anticlinic and synclinic ordering, q_T . Some subphases have been experimentally observed, and the existence of further subphases has been theoretically predicted based on the long-range interlayer interaction and the frustration of clinicity. The structures of subphases becomes decisive using resonant X-ray scattering (RXS). In RXS, using X-ray whose energy is coincident with a certain atom absorption edge, the structure factor becomes a tensor instead of the scalar in conventional X-ray diffraction. Using this technique, one of authors (YT) discovered at least four new subphases with 6-, 7-, 8- and 10-layer periodicities[2].

Unexpectedly, it was found that the temperature change between SmC* and SmC_A* is continuous in some chiral binary system. In this system, clear phase transition between subphases seems not to be seen[2], but the system does not have a specific atom whose absorption edge energy is corresponding to that of hard x-ray. Hence, resonant soft x-ray scattering (RSoXS) has been applied to this study, and we directly observed the structure of continuous change between SmC* and SmC_A* using wide angle RSoXS.

The experiment was performed at BL3U of UVSOR. Used sample is a mixture of MC881 and MC452, as shown in Fig. 1. Figure 1(c) shows the phase diagram around the critical mixing ratios. In this study, samples used were filled in the grid mesh for electron transmission microscopy. The scattering was detected by CCD (ANDOR DO940P-BN). Incident X-ray beam was tuned between 270~300 eV, and carbon K-edge energy was 284.5 eV in the mixture.

Figure 2(a) shows a typical RSoXS intensity profile of the mixture of 55.7wt% MC452 at 24°C. Splitted strong peak at $Q \sim 0.5 \text{ nm}^{-1}$ corresponds to the 4-layer periodicity. Peak splitting is caused by the macroscopic helical structure, whose pitch is corresponding to ca. 1.1 μm . 4-layer periodicity is kept until 80 °C, which is almost consistent with region assigned as $q_T = 1/2$ of ref.

[3] as shown in Fig.1 (c). This result made the structure of the secondary phase with a wide temperature range conclusive. Above 80 °C, resonant peak is gradually shifted corresponding to the longer periodicity, which indicated incommensurate structure from 4layer periodic one. The concentration dependence of the long-range structure will be next subject.

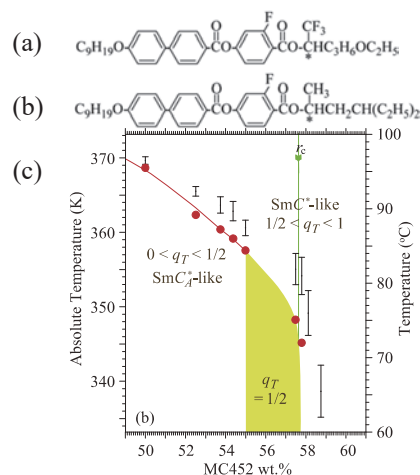


Fig. 1. Chemical structures of (a)MC452 and (b) MC881, and the phase diagram(c). (c) is referred from [3]

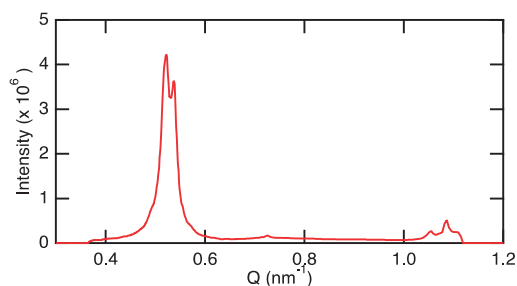


Fig. 2. A RSoXS intensity profile of the mixture of 55.7wt% MC452 at 24°C.

[1] Y. Takanishi *et al.*, Phys. Rev. E **87** (2013) 050503(R).

[2] Z. Feng *et al.*, Phys. Rev. E **96** (2017) 012701.

[3] Z. Feng *et al.*, Phys. Rev. E **102** (2020) 012703.

BL3B, 7B

Evaluation of Measurements of Fluorescence Lifetimes in Multi Bunch Mode

Y. Tajima, Y. Hayashi, K. Shintate, R. Abe, T. Naito, S. Sakano and H. Y. Yoshida
Department of Physics, Yamagata University, Yamagata 990-8560, Japan

Measurement of fluorescence lifetimes requires an adequate time interval before the next excitation, so we use beam time in single bunch mode with a bunch interval of 177 ns. Since most plastic scintillators and wavelength shifters used in high energy physics have short lifetimes (< 3 ns), a measurement in multi bunch mode with a bunch interval of 11 ns seems to be possible.

The purpose of this experiment was to measure fluorescence lifetimes in multi bunch mode using samples that have already been measured, and to evaluate how well multi bunch mode measurements work for samples with short fluorescence lifetimes.

Without changing the optical system, two different methods of data acquisition were attempted: one measurement using the same circuit and MCA as before and the other measurement of direct analog signal collection using a digitizer. The digitizer was BBTX-112 (Bee Beans Technology) with sampling rate was 5 Gsps (200 ps interval). The specification is shown in Fig.1 and Table 1.

Figure 2 displays the typical recorded data using the digitizer. The red line is the signal from photo-multiplier tube and the green line is the RF signal (90.1MHz / 16 = 5.63MHz) from the accelerator.

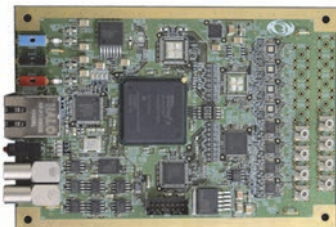


Fig. 1. Bee Beans Technology BBTX-112.

Table 1. Specification of BBTX-112.

Analog Input	8ch (SMB connector)
Sampling Rate (Gsps)	1 / 2 / 3.3 / 5
Time Range (ns)	1000 / 500 / 333 / 200
Output	Ethernet (RJ-45) 1Gbps
Power	$\pm 3.3V$ 1.6/0.5A

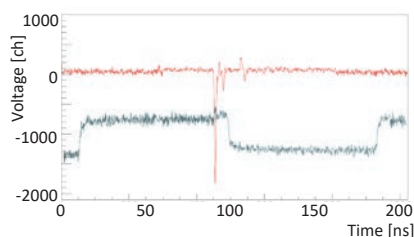


Fig. 2. The recorded data using the digitizer. PMT signal (Red) and RF Signal (Green).

The measured samples were Y-11 and YS6 (made by Kuraray [1]), used as the read-out for gamma-ray sampling calorimeters in high energy physics. Both samples have only one component of fluorescence lifetime, 6.6 ns (Y-11) and 1.3 ns (YS6) [2].

Figure 3 shows the time distribution between the PMT signal and the RF signal, with blue lines representing multi bunch mode, and green areas representing single bunch mode.

In multi bunch mode, the incoming beam bunches were 10 bunches. But the bunches appear to be 14 in Fig.3. These are likely to be leaked from the 10 bunches to the adjacent bunches.

The results of the fluorescence lifetimes are shown in Table 2. The measurements of fluorescence lifetimes in multi bunch mode are found to be as feasible as in single bunch when the fluorescence lifetime of a sample has one component. In the case of samples with multiple components, it is only possible to determine whether there are short-lived components.

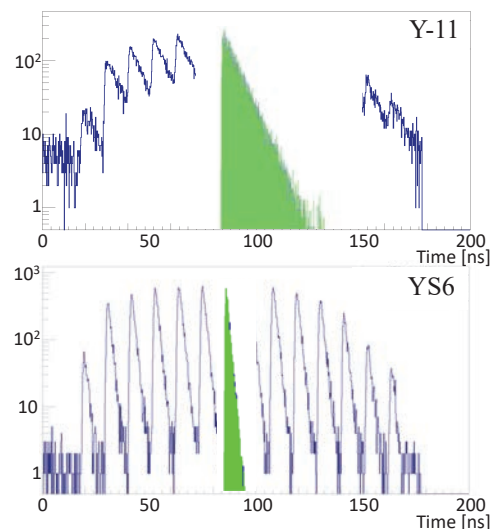


Fig. 3. The time distribution of the single photon and RF signal of Y-11 and YS6 (Blue: multi bunch mode, Green: single bunch mode).

Table 2. The results of fluorescence lifetimes.

	Single bunch	Multi bunch
Y-11	6.65 ns	6.65 ns
YS6	1.40 ns	1.34 ns

[1] Kuraray, "Plastic Scintillating Fibers, Plastic Imaging Fibers", <http://kuraraypsf.jp/>.

[2] K. Shintate *et al.*, UVSOR Activity Report **49** (2022) 66.

Effect of Ce Co-Doping to Cr:GGG as a Scintillator for Dose-Rate Monitoring System

D. Matsukura^{1,2}, S. Kurosawa^{2,3,4}, C. Fujiwara^{1,2} and A. Yamaji^{2,3}

¹School of Engineering, Tohoku University, Sendai 980-8579, Japan

²Institute for Materials Research, Tohoku University, Sendai 980-8577, Japan

³New Industry Creation Hatchery Center, Tohoku University, Sendai 980-8579, Japan

⁴Institute of Laser Engineering, Osaka University, Suita 565-0871, Japan

For the decommissioning of the Fukushima Daiichi nuclear power plant, real-time radiation dose rate monitoring system is required [1], and such system is plan to consist of scintillator, 100-m long optical fiber and CCD spectrometer. Due to high dose rate condition, noise such as Cherenkov light or scintillation light are expected to be observed for the optical fiber [2, 3]. These noises are dominant in the wavelength range below 650 nm. Therefore, the emission wavelength of the scintillator should be 650-1000 nm. Also, high light output is required for the scintillator.

In this study, we focused on Ce/Cr co-doped $Gd_3Ga_5O_{12}$ (Ce/Cr:GGG) as a scintillator. Cr-doped $Gd_3Ga_5O_{12}$ (Cr:GGG) is known to have emission wavelength of 730 nm originating from d-d transition of Cr^{3+} . In addition, by co-doping Ce, the increase of light output of Cr:GGG is expected. Ce-doped $Gd_3Ga_5O_{12}$ (Ce:GGG) has Ce^{3+} absorption bands (approximately 350, 450 nm), while no emission light is observed originating from Ce^{3+} [4]. We expected increase of the light output by Ce^{3+} absorption bands and energy transfer from Ce^{3+} to Cr^{3+} . Since similar energy transfer for the garnet host were reported [5-7], similar energy transfer in Ce/Cr:GGG was expected and we investigated such transfer.

Ce/Cr:GGG crystals were grown by the micro-pulling down method in following compositions: $(Gd_{1-x}Ce_x)_3(Ga_{0.995}Cr_{0.005})_5O_{12}$, where $x=0, 0.01, 0.1$ and 1%, and hereafter we describe as xCe0.5%Cr:GGG. Grown crystal were sliced into 1-mm thickness and evaluated their photoluminescence (PL) at 10 K (excitation wavelength: 100-700 nm) using BL3B.

Figure 1(s) show Ce/Cr:GGG grown crystals, and photoluminescence excitation and photoluminescence (PLE-PL) spectra for these samples were displayed in Fig. 2. In the PLE spectra, the emission intensity around the excitation wavelength of approximately 350 nm slightly increased with increasing Ce concentration. However, the emission intensity of 1%Ce0.5%Cr:GGG decreased at excitation wavelengths around 400-450 nm.

This result indicated some excited energy originating from Ce^{3+} absorption become nonradiative transitions.

Thus, in the GGG system, Ce-co-doping does not support increasing light output in this composition.

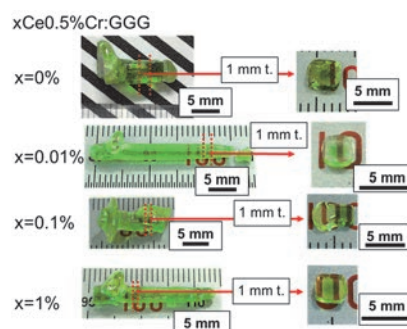


Fig. 1. Ce/Cr:GGG crystals.

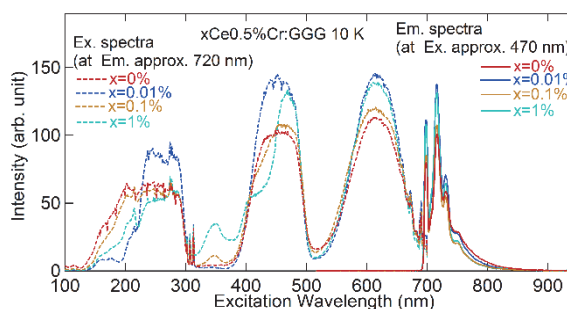


Fig. 2. PLE-PL spectra, dashed line: excitation spectra, solid line: emission spectra.

- [1] Fukushima Administrative Department Sector of Fukushima Research and Development, JAEA, TOPICS Fukushima No.70 (2015).
- [2] Fosco Connect, Optical Fiber Loss and Attenuation. (2010).
- [3] H. Liu *et al.*, Rev. Sci. Instrum, **89** (2018) 083302.
- [4] V. Baranov *et al.*, Phys. Part. Nucl. Lett. **17** (2020) 878.
- [5] X. Yi *et al.*, Ceram. Int. **40** (2014) 7043.
- [6] Y. Tang *et al.*, J. Am. Ceram. Soc. **100** (2017) 2590.
- [7] G. Merkininkaite *et al.*, Ceram. Int. **49** (2023) 16796.

BL3B

Optical Properties of Li-Containing $\text{Cs}_3\text{Cu}_2\text{I}_5$ for Neutron Monitor

Y. Urano^{1,2}, S. Kurosawa^{2,3,4} and A. Yamaji^{2,3}

¹Graduate School of Engineering, Tohoku University, Sendai 980-0845, Japan

²Institute for Materials Research (IMR), Tohoku University, Sendai 984-8577, Japan

³New Industry Creation Hatchery Center (NICHe), Tohoku University, Sendai 980-8579, Japan

⁴Institute of Laser Engineering, Osaka University, Suita, Osaka 565-0871, Japan

In order to decommission the Fukushima Daiichi Nuclear Power Plant quickly and safely and reliably, radiation monitoring is required to accurately evaluate the debris with radio-isotopes inside the reactor. We have proposed a dose monitor consisting of a scintillator, optical fiber with a length of 50-100m and CCD spectrometer, and scintillation photons are read under lower dose conditions with the CCD [1-2]. The presence of neutrons as well as gamma rays in the reactor has been suggested [3], and detailed mapping of neutrons is also required. In addition, when the scintillator emission wavelength is less than 500 nm, such emission bands are overlapped with noise bands under such a high dose rate due to scintillation or Cherenkov photons generated in the optical fiber itself. Therefore, scintillator materials with high neutron sensitivity and long emission wavelength are required.

$\text{Cs}_3\text{Cu}_2\text{I}_5$ (CCI) has a high light output of 41,500 photons/MeV and an emission wavelength of approximately 440 nm [4, 5]. However, CCI has low neutron sensitivity and the emission wavelength is also shorter than the target value.

We have developed Li-containing $\text{Cs}_3\text{Cu}_2\text{I}_5$ (CCIL) crystals for the neutron detector, because ^6Li has a large neutron capture cross-section. In this study, we grew the CCIL crystal, and its luminescence properties were investigated.

The CCIL crystal specimen was synthesized by the vertical Bridgman growth method in our laboratory using CuI, CsI and LiI raw materials. The neutron detection capability of CCIL has been evaluated in our laboratory. In order to reveal the emission mechanism and compare to such mechanism with CCI, we measured the temperature dependence of photoluminescence excitation and emission spectra from 10 K to 300 K at UVSOR BL3B beam line.

Figure 1 shows the photoluminescence excitation and emission spectra of Li-containing $\text{Cs}_3\text{Cu}_2\text{I}_5$. CCIL showed broad luminescence with a peak at approximately 450 nm at an excitation wavelength of 331 nm at 300 K, which was slightly longer than that of CCI (440 nm).

Figure 2 shows the temperature dependence of emission intensity for CCIL excited with 298 to 331-

nm photons. As the temperature increased, the emission intensities decreased. In the future, we compare the temperature dependence between CCI and CCIL.

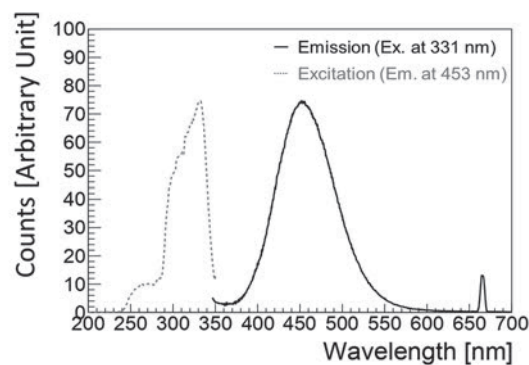


Fig. 1. Photoluminescence excitation and emission spectrum of Li-containing $\text{Cs}_3\text{Cu}_2\text{I}_5$ scintillator at 300 K.

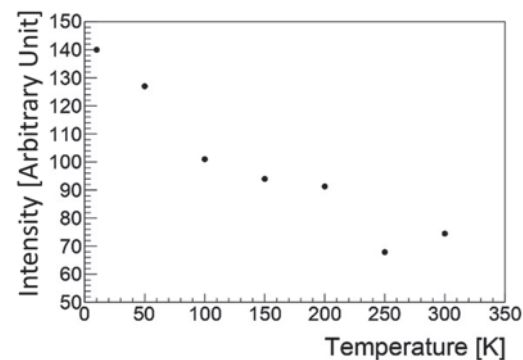


Fig. 2. Temperature dependence of emission intensity of Li-containing $\text{Cs}_3\text{Cu}_2\text{I}_5$ scintillator.

[1] <https://fukushima.jaea.go.jp/en/pamphlet/topics/pdf/topics-fukushima070e.pdf>.

[2] C. Fujiwara, S. Kurosawa and A. Yamaji, UVSOR Activity Report **50** (2023) 78.

[3] https://www.tepco.co.jp/decommission/information/committee/roadmap_progress/pdf/2022/d221222_08-j.pdf.

[4] L. Stand *et al.*, J. Phys. Chem. C **126** (2022) 12882.

[5] T. Jun *et al.*, Adv. Mater. **30** (2018) 1804547.

Luminescence Characteristics of Synthetic Diamonds

A. Umemoto^{1,2}

¹International Center for Quantum-field Measurement Systems for Studies of the Universe and Particles (QUP), High Energy Accelerator Research Organization (KEK), Tsukuba 305-0801, Japan

²Division of Physics, University of Tsukuba, Tsukuba 305-8571, Japan

Diamond is expected to be used as a scintillator for radiation detectors because color-centers are easily formed through impurity doping. Applications of diamond scintillators extend to fields such as radiation monitor, medical imaging, and astro-particle physics such as a dark matter search. “C center”, which is a nitrogen-replacing carbon in diamond, generates a luminescence band in visible wavelength. We showed basic characteristics of diamond scintillator by using a commercially available synthetic crystal [1]. At present, with the cooperations of Prof. Taniguchi and Miyakawa in the Research Center for Materials Nano-Architectonics, National Institute for Materials Science, synthetic diamonds via high-pressure high-temperature (HPHT) method with containing nitrogen impurities can be used for studying the luminescence properties.

In the beam time of FY2023, photoluminescence measurements were conducted on HPHT diamonds containing nitrogen impurities ranging from 1 to 200 ppm. Figure 1 shows the comparison of photoluminescence spectra of HPHT diamonds with various nitrogen concentrations at room temperature. The excitation wavelength was set to $\lambda=220$ nm, which corresponds to a similar energy as the bandgap of diamond. The spectrum shape of each sample varied depending on the nitrogen concentration, and the emission on the short wavelength would be increased in lower nitrogen concentration. Although it was not easy to quantify the light-yield of scintillator using the BL3B measurement setup, we can estimate high light-yield at low nitrogen concentration. Since the nitrogen impurities in diamond absorb light from the ultraviolet to visible region, it is anticipated that the detected light would decrease especially at wavelengths below 500 nm, particularly for diamonds with high nitrogen content.

Next, we evaluated the temperature dependence of luminescence characteristics about diamond with a nitrogen concentration of 28 ppm. Luminescence at temperatures around 7 K was measured by using liquid helium, and thermoluminescence (TL) during heating after irradiation was measured by using a thermo-controller. The results revealed a shift in the spectrum towards longer wavelength at the low temperature, and the luminescence spectrum of TL with the sample temperature of around 200 K closely resembled the photoluminescence spectrum observed at room temperature. Furthermore, the trap depth of diamond

estimated from the thermoluminescence measurement was approximately ~ 0.3 eV.

The difference of photo luminescence process of diamond between at low temperature and room temperature has not been clear yet. Scintillators are sometime used at low temperature to improve their light-yields. Hence, further investigations are needed to understand the luminescence characteristics at low temperatures and to determine the optimal nitrogen concentration for enhancing the quality of diamond scintillator.

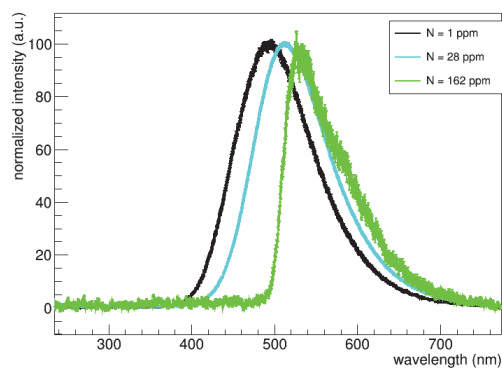


Fig.1. Photoluminescence spectra of HPHT diamonds with various nitrogen concentrations.

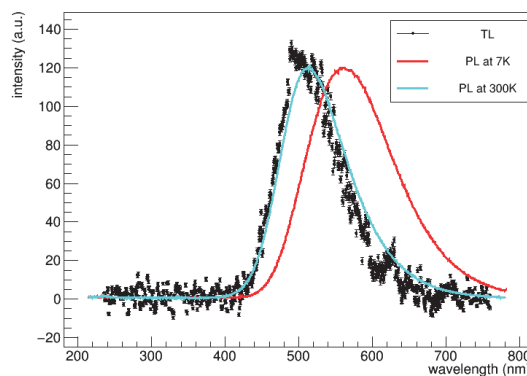


Fig.2. Temperature dependence of luminescence characteristics and thermoluminescence for diamond with a nitrogen concentration of 28 ppm.

[1] A. Umemoto *et al.*, Nucl. Instrum. Methods Phys. Res., Sect. A **1057** (2023) 168789.

BL3B

Photoluminescence Properties of CsI Crystals Obtained Via the Melt Aging Procedure Using I₂ Gas

S. Omiya, S. Kodama, N. Shimoyama, T. Saito, I. Yanase and H. Takeda
*Graduate school of Science and Engineering, Saitama University,
 255 Shimo-Okubo, Sakura-ku, Saitama 339-8570, Japan*

The presence of water (H₂O) and H- or O-containing impurities degrades the optical properties of halide crystals. A method for removing water from the starting material by treatment with reactive gas before crystal growth (Reactive Gas Process, RAP) has been proposed to improve the quality of halide crystals [1]. In addition, to remove excess halogen ions from the raw material, we combined the RAP technique with the melt aging (MA) technique. In the MA process, the raw material is melted under a vacuum atmosphere for a few hours to days [2]. In this study, as the first test of the RAP+MA technique, CsI was treated under several temperature conditions.

The melting point of CsI is 621 °C. CsI was subjected to RAP treatment at 500 °C, which is lower than its melting point, and MA treatment for 24 hours (RAP500-MA24). For comparison, CsI was subjected to RAP treatment at 650 °C, which is higher than its melting point, and MA treatment for 24h (RAP650-MA24). Sublimated I₂ gas was used as reactive gas. CsI was gradually cooled and crystallized.

Before evaluating the optical properties, the crystal phases of the obtained CsI crystals (RAP500-MA24 and RAP650-MA24 specimens) were identified by powder X-ray diffraction. Only the CsI phase and no shifts in the diffraction peaks were observed. The optical properties and photoluminescence emission spectra of the RAP500-MA24 and RAP650-MA24 specimens were measured at the BL3B. The experiments were performed at 10 K and 300 K.

The photoluminescence emission spectra of the RAP500-MA24 and RAP650-MA24 specimens are shown in Figure 1. A strong emission peak at approximately 440 nm is observed at 10 K for the RAP500-MA24 specimen. Weak emission peaks were observed at 310 nm and 340 nm. In contrast, the RAP650-MA24 specimen exhibited strong peaks at 310 and 340 nm. The intensity of the 440-nm-emission was suppressed compared to that of the RAP500-MA24 specimen.

The luminescence at 310 nm and 340 nm is attributed to self-trapped exciton (STE) emission, and the luminescence around 440 nm is attributed to impurity

emission from O-containing impurities [3,4]. The above results suggest that O-containing impurities, such as H₂O, were effectively removed by the RAP technique from the melted CsI raw material. However, the RAP technique against the non-melted CsI raw material had a negligible effect on removing such impurities. In future work, the RAP-MA conditions should be optimized to grow large halide crystals with high optical quality.

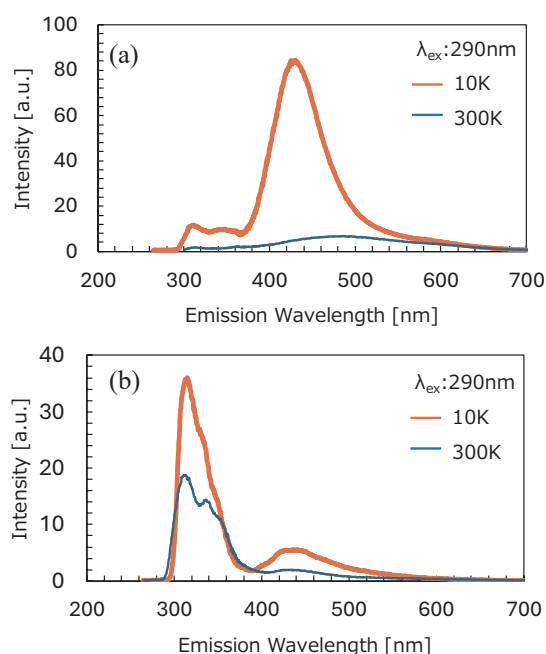


Fig. 1. Photoluminescence emission spectra of CsI crystals at 10 K and 300 K for the (a) RAP500-MA24 and (b) RAP650-MA24 specimens.

- [1] S. Sakuragi, *Am. J. Chem. Eng.* **9** (2021) 25.
- [2] Y. Wu *et al.*, *Cryst. Growth Des.* **8** (2015) 3929.
- [3] S. Kubota *et al.*, *Nucl. Instrum. Methods Phys. Res., Sect. A* **268** (1988) 275.
- [4] L.N. Shpilinskaya *et al.*, *Semicond. Phys. Quantum Electron. Optoelectron.* **3** (2000) 2.

Bandgap Determination of CaCO_3 by Excitation Spectrum in the VUV Range

H. Miyata and J. Ueda

Japan Advanced Institute of Science and Technology, Nomi 923-1292, Japan

Persistent phosphors are luminescent materials that emit light for a long duration after the excitation source is turned off. They are widely used in many applications such as luminous paints in the dark for hazard signboards and road markers and luminescent markers for in vivo imaging. Persistent luminescence originates from the temporary trapping of the electrons or holes generated with light absorption by crystalline defects. The trapped electrons or holes are thermally released and transferred back to the luminescent center.

The carrier trapping depth of lanthanoid ions-activated persistent phosphors can be designed semi-empirically by elucidating the solid-state electronic structure. The depth of electron traps by trivalent lanthanoid ions in solids can be predicted from the vacuum level reference binding energy (VRBE) diagram [1]. The VRBE diagram is constructed from the valence and conduction bands of the host crystal and the ground levels of divalent and trivalent lanthanoids. To create a VRBE diagram, the charge transfer energy E^{CT} of Eu^{3+} , $U(6, A)$, and band gap E_g are required. To obtain these spectroscopic parameters, the photoluminescence excitation spectrum or the absorption spectrum in the range from VUV to UV is required.

So far, aluminates and silicate compounds such as $\text{SrAl}_2\text{O}_4\text{:Eu}^{2+}\text{-Dy}^{3+}$ [2] and $\text{Sr}_2\text{MgSi}_2\text{O}_7\text{:Eu}^{2+}\text{-Dy}^{3+}$ have been widely used as practical persistent phosphors. In contrast, oxides including other oxoanion (CO_3^{2-} , NO_3^- and etc.) and non-oxides are still an unexplored material group for persistent phosphors and have the potential to show excellent persistent luminescent properties. We propose carbonate compounds as a new host material and focus on CaCO_3 with the calcite crystal structure. In this report, the photoluminescence excitation spectra of a natural single crystal of calcite and the synthesized CaCO_3 powder were analyzed to elucidate the solid-state electronic structure of calcite.

Photoluminescence (PL) and PL excitation (PLE) spectra of the natural crystal of calcite and the CaCO_3 powder at 10 K are shown in Fig. 1 and 2. Both samples show a broad PL band around 430 nm at 10 K, while this PL band was not observed at room temperature. The PL band can be attributed to defect luminescence. In the PLE spectra of this defect luminescence, a broad PLE band is observed around 210 nm in both samples. Also, the synthesized CaCO_3 sample shows a relatively strong PLE band at 175 nm, while in the natural calcite sample this PLE band is very weak. In the measured transmittance spectrum of the natural CaCO_3 sample (not shown here), an absorption band rises from 205

nm and the absorption intensity is saturated around 195 nm. Therefore, the PLE band at 210 nm can be related to the defect absorption and that at 175 nm can be related to the host exciton. The E_g is calculated to be 7.65 eV using E^{ex} (175 nm). However, the bandgap of CaCO_3 (calcite) was reported to be around 6.0 eV [3]. The obtained E_g in this study is 20% larger than the previously reported value. In order to discriminate the attribution of the host exciton band and the defect absorption, the further study is necessary.

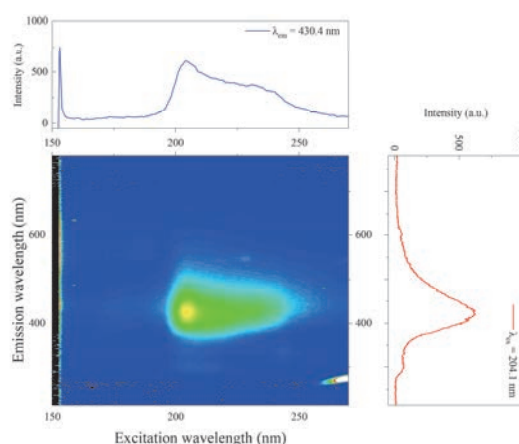


Fig. 1. PL/PLE 2D mapping of natural calcite at 10 K.

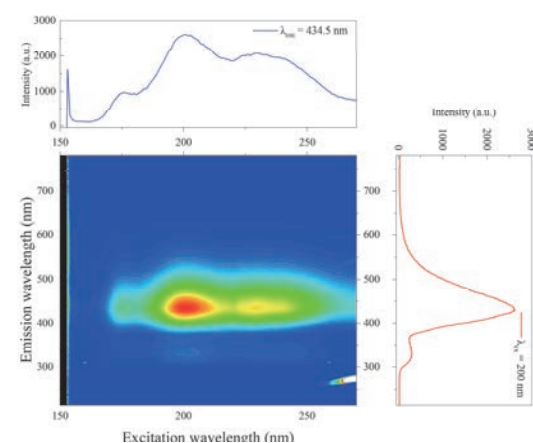


Fig. 2. PL/PLE 2D mapping of the synthesized CaCO_3 powder at 10 K.

[1] P. Dorenbos, *Phys. Rev. B: Condens. Matter* **85** (2012) 165107.

[2] T. Matsuzawa *et al.*, *J. Electrochem. Soc.* **143** (1996) 2670.

[3] D.R. Baer and D.L. Blanchard, *Appl. Surf. Sci.* **72** (1993) 295.

BL3B

Luminescence Properties of CsAg₂I₃ and Cs₂AgI₃ Crystals

T. Kawai and S. Ibuki

Graduate School of science, Osaka Metropolitan University, Sakai 599-8531, Japan

In the past decade, hybrid perovskite Pb halides and various ternary Pb halides have been extensively investigated for application to solar cells, scintillator materials, photodetectors, and light-emitting diodes [1,2]. However, the environmental toxicity of Pb remains a significant concern. Therefore, considerable efforts have been made to develop alternative environmentally friendly Pb-free ternary metal halides [3,4]. In this study, we focused on Pb-free CsAg₂I₃ and Cs₂AgI₃ crystals. The CsAg₂I₃ and Cs₂AgI₃ crystals were prepared by the Bridgman method from high-purity CsI and AgI powders, which were mixed in a stoichiometric ratio.

Figure 1 (a) and (b) show the luminescence and excitation spectra of the CsAg₂I₃ and Cs₂AgI₃ crystals at 10 K, respectively. In CsAg₂I₃, the luminescence band is observed at 3.37 eV. The excitation spectrum for the 3.37 eV luminescence band has a sharp rise from 3.75 eV and an excitation band peaking at 3.82 eV, which correspond to the absorption edge and the transition region of the band-edge excitons in CsAg₂I₃, respectively [5]. In Cs₂AgI₃, the broad luminescence band is observed at 2.22 eV. The 2.22 eV luminescence exhibits a sharp rise from 4.05 eV and an excitation band peaking at 4.41 eV in the excitation spectrum. The energy positions also correspond to those of the absorption spectrum of the Cs₂AgI₃ thin film reported in a previous paper [6]. The luminescence bands at 3.37 and 2.22 eV in CsAg₂I₃ and Cs₂AgI₃, respectively, have a Gaussian-like shape with half-width of about 0.14 and 0.34 eV, respectively, and could be attributed to a self-trapped exciton (STE) of the respective crystals.

Assuming that the lowest peaks in the excitation spectra are the lowest exciton transition energies, the STE luminescence in CsAg₂I₃ and Cs₂AgI₃ has a Stokes shift energy of about 0.41 and 2.2 eV, respectively. The Stokes shift energy of the STE in CsAg₂I₃ is much smaller than that of the STE in Cs₂AgI₃. Therefore, the exciton-phonon interaction in CsAg₂I₃ is weaker than that in Cs₂AgI₃.

What is noteworthy is that a weak emission line is observed at 3.77 eV in CsAg₂I₃. An enlarged spectrum is shown in the inset of Fig.1 (a). Since the value of 3.77 eV is roughly equal to the exciton resonance energy [5], the luminescence line at 3.77 eV is considered to be free exciton (FE) luminescence. This implies that FE and STE coexist in the CsAg₂I₃ crystals. In Cs₂AgI₃, on the other hand, the luminescence line is

not observed in the vicinity of the exciton-resonance energy region reflecting the strong exciton-phonon interaction.

In AgI crystals, no STE luminescence band is observed, and exciton luminescence bound to defects was observed with small Stokes shifts [7]. On the other hand, the STE luminescence with a large Stokes shift is observed in CsI crystals [8]. The ratio of AgI and CsI present in the crystals may be related to the strength of the exciton-lattice interaction.

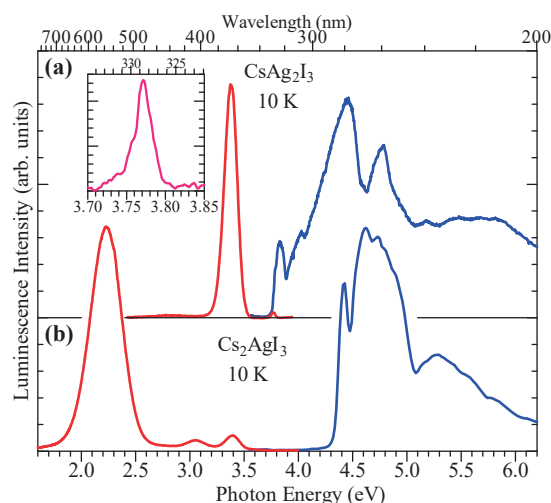


Fig. 1. Luminescence and excitation spectra of (a) CsAg₂I₃ and (b) Cs₂AgI₃ at 10 K. Inset shows the enlarged luminescence spectrum in the vicinity of the exciton-resonance energy region in CsAg₂I₃.

- [1] A. K. Jena, A. Kulkarni and T. Miyasaka, *Chem. Rev.* **119** (2019) 3036.
- [2] J. Yan *et al.*, *Chem. Mater.* **35** (2023) 2683.
- [3] A. Kumer *et al.*, *Appl. Surf. Sci. Adv.* **18** (2023) 100495.
- [4] Q. Yang, *et al.*, *Mater. Today Phys.* **36** (2023) 101143.
- [5] S. Ibuki and T. Kawai, *UVSOR Activity Report* **50** (2023) 81.
- [6] V. K. Miloslavskii, S. T. Lin and O. N. Yunakova, *Opt. Spectrosc.* **80** (1996) 643.
- [7] S. Mochizuki and F. Fujishiro, *Phys. Status Solidi C* **3** (2006) 3586.
- [8] H. Nishimura *et al.*, *Phys. Rev. B: Condens. Matter* **51** (1995) 2167.

Luminescence Properties of Co-Doped NaCl:I, Ce³⁺ Crystals

R. Oda and T. Kawai

Graduate School of Science, Osaka Metropolitan University, Sakai 599-8531, Japan

In our previous paper, we reported an energy transfer from I⁻ centers to TI⁺ centers via V_K centers in NaCl:I, TI⁺ crystals [1]. By considering the hopping motion of V_K center, we could explain the changes in the temporal response of I luminescence. However, the emission lifetime of TI⁺ centers were so long compared to the repetition interval of the excitation pulse, and we were unable to discuss the decay profile of TI⁺ luminescence. In this study, we selected Ce³⁺ ions as acceptor ions, which have a short emission lifetime, instead of TI⁺ ions. Here, we reported on the luminescence properties of co-doped NaCl:I, Ce³⁺ crystals.

NaCl:I, Ce³⁺ crystals were grown by the vertical Bridgman method from NaCl, CeCl₃ and NaI powders. The Ce³⁺ and I concentrations in the starting materials were 0.179 and 0.021 mol%, respectively.

As shown in Fig. 1, two luminescence peaks due to the Ce³⁺ centers were observed at 3.37 eV and 3.64 eV. In the excitation spectra, five peaks were observed at 4.32, 4.52, 4.74, 4.98, and 5.18 eV. The Ce³⁺ center has the 4f¹ and 5d¹ electron configuration in the ground and excited state, respectively. The ground 4f level splits into two levels because of the spin-orbit interaction. The excited 5d level splits into five levels by the crystal field. The luminescence peaks are attributed to the radiative transition from the lowest 5d excited level to the split 4f ground levels. The five excitation peaks are assigned to the optical transition from the lower 4f ground level to the split 5d excited levels.

In Fig. 2, the luminescence and excitation bands due to I⁻ centers were observed at 5.7 and 7.0 eV, respectively. Although the luminescence of the Ce³⁺ centers was also observed, the intensity was very weak compared to the luminescence of the I⁻ centers.

There is a dip in the excitation spectrum of the Ce³⁺ luminescence in the co-doped NaCl:I, Ce³⁺ at 7.0 eV where the excitation band of the I⁻ luminescence is located. As shown by the green curve in Fig.1, on the other hand, no dip was observed at 7.0 eV in the excitation spectrum of the Ce³⁺ luminescence in single-doped NaCl:Ce³⁺. Thus, the dip indicates that the I⁻ centers are efficiently excited at 7.0 eV, while only a few Ce³⁺ centers are directly excited.

Noteworthy, there is little overlap between the luminescence of the I⁻ centers and the excitation peaks of the Ce³⁺ centers. The fact implies that the energy transfer from I⁻ centers to Ce³⁺ centers is hard to occur by resonance and/or emission-reabsorption mechanism in co-doped NaCl:I, Ce³⁺. The energy transfer by the

hopping motion of the V_K centers is expected, in the similar to NaCl:I, TI⁺ crystals.

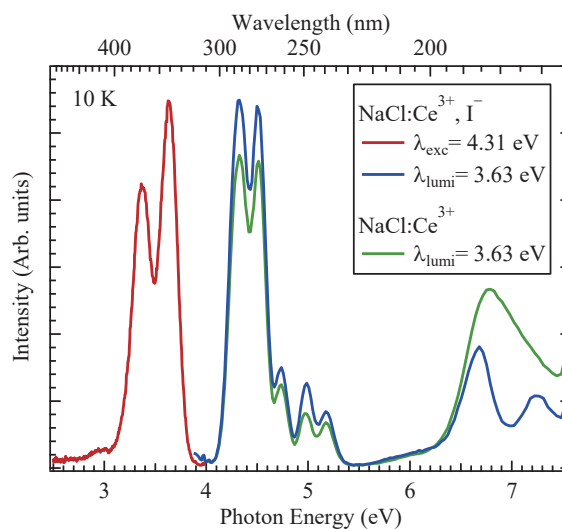


Fig. 1. Luminescence spectrum under excitation 4.31 eV for co-doped NaCl:Ce³⁺, I⁻ (red) and excitation spectra detected at 3.63 eV for co-doped NaCl:Ce³⁺, I⁻ (blue) and single-doped NaCl:Ce³⁺ (green) at 10 K.

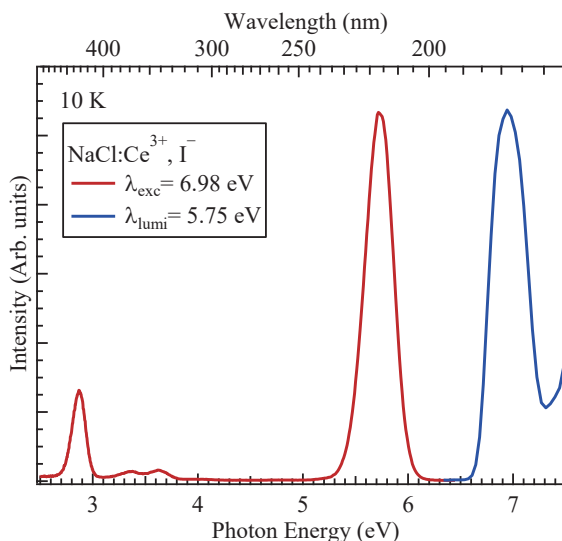


Fig. 2. Luminescence spectrum under excitation 6.98 eV (red) and excitation spectrum detected at 5.75 eV (blue) for co-doped NaCl:Ce³⁺, I⁻ at 10 K.

[1] O. Yagi, T. Kawai and K. Mizoguchi, *J. Lumin.* **226** (2020) 117359.

BL4U

Electronic Structure Identification of the Free-Standing Hexagonal Boron Nitride Membranes

C. O. M. Mariano¹, J. S. D. Rodriguez^{1,2}, T. Araki³ and C.-H. Chuang¹

¹Department of Physics, Tamkang University, Tamsui, New Taipei City 251301, Taiwan

²Institute of Chemistry, Leiden University, Leiden, 2300 RA, The Netherlands

³Institute for Molecular Science, Okazaki 444-8585, Japan

A honey-like structure with sp^2 hybridized orbitals is noted for a typical lattice in graphene (G) or hexagonal boron nitride (hBN), which of difference likes boron (B) and nitrogen (N) atoms alternatively bonded in the basal plane. Unlike a zero bandgap in G, hBN behaves as a wide band gap (~ 6 eV) due to the partly ionic B-N bond and its electron-delocalization on the basal plane. The unique coordination of hBN down to the nanosheets has excellent properties in high chemical/thermal stability, enhanced thermal/electrical conductivity, and flexible doping capability, leading to various applications in dielectric substrates, UV light emitters, and functional coatings. Thus, a valuable synthesis of a few hundred nm in thickness and a few centimeters in an area with the free-standing type of hBN membranes is our objective in the BL 4U for scanning transmission X-ray microscopy (STXM). An in-depth understanding of the morphology, chemical composition, and electronic structure of hBN membranes is significant in developing materials engineering.

The hBN grounding formed the ball-rolled solvent and later cleaned a couple of times in water, particularly for extensive practical application. The cyclic voltammetry method, called CV hBN, was used to grow the free-standing and thin-thickness membrane on a gold mesh, compared to the control sample by the drop-cast (DC) and dried in air. The previous characterization, such as transmission electron microscopy, Raman microscopy, and Photoluminescence microscopy, displays that DC and CV hBN are highly similar to the bulk case in the ordered lattice structure and the typical photo-electron process. One wide-range emission that emerged in the background was found in PL, hinting only at the solution-induced difference.

The area-selected absorption spectra and element-dependent images are powerful capabilities in STXM for information of interest in surface morphology. The three areas (indicated as “1”–“3”) in DC hBN and the other areas (indicated as “4”–“6”) in CV hBN are shown in different element-resolved results in Fig. 1(a)–(f), as indicative of the same region of SEM images in the inset. In Fig. 1(a)(d), an intensive peak at 192.0 eV and double-split peak at 198.0 and 199.5 eV are assigned to the $1s \rightarrow \pi^*$ and σ^* resonance for the angular orientation of B- p_z /N- p_z direction and B- p_{xy} /N- p_{xy} plane. There is no difference between DC and CV hBN, except for the relative intensity ratio of π^* and σ^* resonance for the polarization dependence of the plane structure and X-ray incidence. Fig. 1(b) and (e) are the N K-edge spectra of DC and CV hBN, which are identical of $1s \rightarrow \pi^*$ resonance at 401.6 eV and σ^* resonance between the range of 408.0 and 420.0 eV.

The N- p_z (π^*) peak with the low and broad signal in the area of “3” in DC hBN and “6” in CV hBN reflects the polycrystalline feature by the stacking formation. The narrow peaks within the 404.0 and 407 eV range in the inset are considered the specific lattice defect or H-passivated vacancies at the B site, which is identical in the area (“1”–“3”) of DC hBN. Because as-obtained hBN was separated from the centrifugation and redispersed in the water solution, the oxygen-modified possibility during the exfoliation process is necessary for the discussion in Fig. 1(c) and (f). Due to the weak optical density signal, a negligible amount of surface O is found in both DC and CV hBN. Two peaks at 531.7 and 539.0 eV are assigned to the electron transition from $1s$ to π^* and σ^* state of adsorbed molecule oxygen, respectively. Besides, the O bonding to B and N sites can be found at 530.6 eV for the N=O state and 531.7 eV for the B-O bond. The synchronization effect of oxygen molecules during the flake stacking and electrochemical reconstruction in the water solution is highly reasonable in the substitutional O or OH species in the vacancy at B and N sites.

Our work indicates a vital identification to track the morphology and electronic structure of freestanding hBN membranes by contrasting electrochemical reactions between DC and CV methods. Various spectral features selected from the area “1” to “6” demonstrate the lattice structure and chemical functionalization between B, N, and O sites, which is addressed by the spatially resolved absorption in STXM.

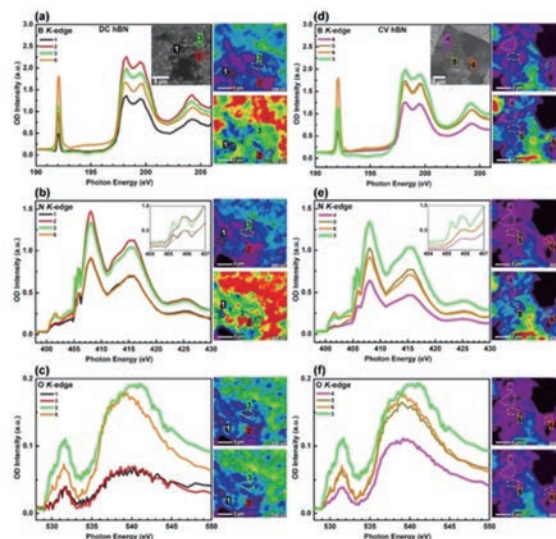


Fig. 1. (a) and (d) B K-edge, (b) and (e) N K-edge, and (c) and (f) O K-edge of DC and CV hBN, respectively.

Transition Metal Dopants on Graphitic Carbon Nitride (g-C₃N₄) for Electrocatalytic Carbon Dioxide Reduction Reaction

W.-T. Chen¹, H. W. Shiu¹, Y.-L. Lai¹, T. Araki² and Y.-J. Hsu^{1,3}

¹Nano Science Group, National Synchrotron Radiation Research Center, Hsinchu 300092, Taiwan

²UVSOR Synchrotron Facility, Institute for Molecular Science, Okazaki 444-8585, Japan

³Department of Photonics, National Cheng Kung University, Tainan 70101, Taiwan

The synthesis of high-order chemicals and fuels from electrochemical carbon dioxide reduction reaction (CO₂RR) has been considered a promising strategy to tackle CO₂ emissions in the near future [1]. Substantial efforts have been made in designing heterogeneous electrocatalysts with improved CO₂RR performance. Among all electrocatalysts, metal atoms embedded with functional nitrogen species (M-N_x) porphyrin-like sites on carbon-based materials, so-called single-atom catalysts (SACs) and dual-atom catalysts (DACs) received numerous attention due to their favorable in exposing abundant unsaturated surface atoms and providing larger active sites for many catalytic reactions [2, 3]. However, these metal-nitrogen-doped carbon materials often contain complicated nitrogen species with low concentrations, which leads to technical difficulty in investigating the structure-activity relationships of SACs and DACs for CO₂RR. In this project, we chose porous graphitic carbon nitride (g-C₃N₄) as the support, because it can provide uniform and stable nitrogen vacancy that can stabilize metal atoms and provide simpler M-N_x reaction sites. We fabricated a series of Cu/g-C₃N₄ (where M = Cu with different loading) samples to study the effect of metal dopants using synchrotron-related techniques, such as scanning transmission X-ray microscopy (STXM) and Near-edge X-ray absorption fine structure (NEXAFS) analysis.

In Fig. 1(a), the optical density (OD) of carbon maps suggested that the C signals came from the carbon paper (light green area) and g-C₃N₄ (orange area). Different Cu loading of pristine 0.7 wt.% Cu/g-C₃N₄ (Cu-SACs) and 12 wt.% Cu/g-C₃N₄ (Cu-DACs) were chosen to study the effect of Cu dopant and loading on the g-C₃N₄ support as shown in Fig. 1(b). All samples showed characteristic π^*_{C-N-C} peak of the g-C₃N₄ samples at 288.0 eV [4]. A weak peak at 285.4 eV was observed due to the use of carbon paper as a free-standing electrochemical electrode during CO₂RR.

Additional shoulder at 287.3 eV was observed in 0.7 wt.% Cu/g-C₃N₄ sample, which can be assigned to a C-H bond from catalyst ink that contains isopropanol, milli-Q water, and 5 wt.% Nafion solution [5].

Furthermore, to explain the fundamental mechanism of the Cu/g-C₃N₄ for CO₂RR, we aim to perform ex-situ experiments on Cu/g-C₃N₄ to study the changes in reaction sites before and after CO₂RR. The correlation between reaction sites and the reaction products (such

as CO, CO₂, and hydrocarbons) is also of interest. The 12 wt.% Cu/g-C₃N₄ sample (pristine and after reaction) was conducted to correlate the catalytic reaction sites with associated CO₂RR products (Fig. 2(a)). After the CO₂ reduction reaction at -0.8 V vs RHE, an additional peak was observed at 290.4 eV, suggesting this peak is associated with CO₂RR-related products. The OD images shown in Fig. 2(b)-(c) suggested the location of 290.4 eV peak (light green) on the g-C₃N₄ sample (red). A mixture of g-C₃N₄ (red) and 290.4 eV (light green) led to the orange particles. Further data analysis is underway to provide ex-situ insight into reaction sites under CO₂RR.

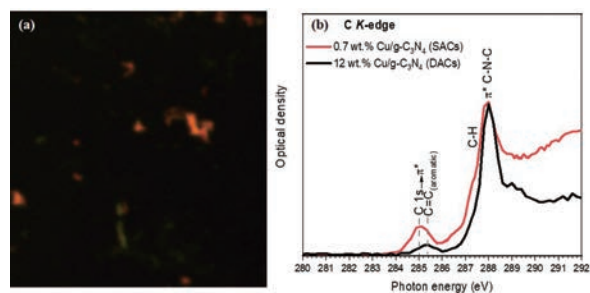


Fig. 1. (a) The OD images of the carbon paper (light green) and Cu/g-C₃N₄ (orange) component maps, and (b) C K-edge NEXAFS spectra of pristine Cu-SACs and Cu-DACs.

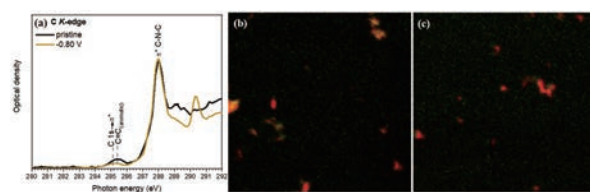


Fig. 2. (a) Ex-situ C K-edge NEXAFS spectra of 12 wt.% Cu/g-C₃N₄ sample before and after CO₂RR, (b) and (c) the OD images of g-C₃N₄ (red) and 290.4 eV (light green) component maps of region 1 and 2 for 12 wt.% Cu/g-C₃N₄ sample after CO₂RR at -0.8 V vs RHE.

- [1] W. Zhang *et al.*, *Adv. Sci.* **5** (2018) 1700275.
- [2] A. S. Varela *et al.*, *ACS Catal.* **9** (2019) 7270.
- [3] R. Li and D. Wang, *Adv. Energy Mater.* **12** (2022) 2103564.
- [4] Y. Zheng *et al.*, *Nat. Commun.* **5** (2014) 3783.
- [5] K. G. Latham *et al.*, *Carbon* **114** (2017) 566.

BL4U

Nm-scale NEXAFS Spectra of Styrene-Butadiene Rubber (SBR) Compounds Mixed with Silica Fillers

T. Ejima^{1,2*} and Y. Tamura³¹SRIS & ²IMRAM, Tohoku University, Sendai 980-8577, Japan³ENEOS Materials Corp., Yokkaichi 510-0871, Japan

In tire tread compounds, elastomers are blended and fillers are added to obtain the properties necessary to achieve optimal tire performance. Elastomers exhibit specific compatibility depending on the level of elastomer incorporation. The aggregation behavior of the filler is also suppressed by the higher compatibility of the filler surface with the elastomer [1, 2]. When silica is added to elastomers blended with SBR and BR, the silica population is higher in the SBR [3]. Our previous electron microscopy observation showed that silica dispersed in SBR causes aggregation with a size of roughly tens to hundreds of nm. The aggregation size depends on the blended species and coupling agents. In this study, to investigate the chemical properties of the elastomer and filler surfaces, which are considered to be important for filler dispersion and network formation, we performed NEXAFS measurements using STXM. And then, by image analysis using typical NEXAFS spectra of each material, we investigate the spectral changes between aggregates of fillers.

Elastomer materials used for samples were normal SBR and chemically modified SBR (m-SBR). The difference between the elastomer materials is crosslink density: the m-SBR has a higher crosslink density than the normal SBR. A silica filler was added to the elastomer materials. A total of four blocks were made combining the elastomer with silica filler ($\Phi 100$ nm or $\Phi 16$ nm in diameter). The resulting blocks were cut into sheets, and then sliced with an ultramicrotome in 100 nm thick to observe.

Distribution of the SBR and aggregation area of the silica fillers were obtained based on the STXM sequential images around C-K edge and is shown in the inset of Figure 1(a). The related NEXAFS spectra of the distribution are also shown in the figure. The red region and the curve show the SBR area and its spectrum, respectively, and the green region and the curve, the silica aggregation area and its spectrum, respectively. The blue area is zinc oxide used as an additive. Comparing the spectrum of the silica aggregation region with that of the SBR region, the shapes of the spectra are almost same except for a different peak-intensity around 285 eV, which is attributed to the π^* anti-bonding states of C=C bond. The spectral shapes of the other samples have same tendency. To compare the peak intensities of the π^* antibonding states between the areas, the integration intensities of the peaks were obtained (Figure 1(b)). The intensity ratios of $\Phi 100$ nm silica samples are same to each other, on the other hand the intensity ratios of

the $\Phi 16$ nm silica samples differed greatly between the SBR and the m-SBR. This difference will be attributed to the difference in surface area of silica.

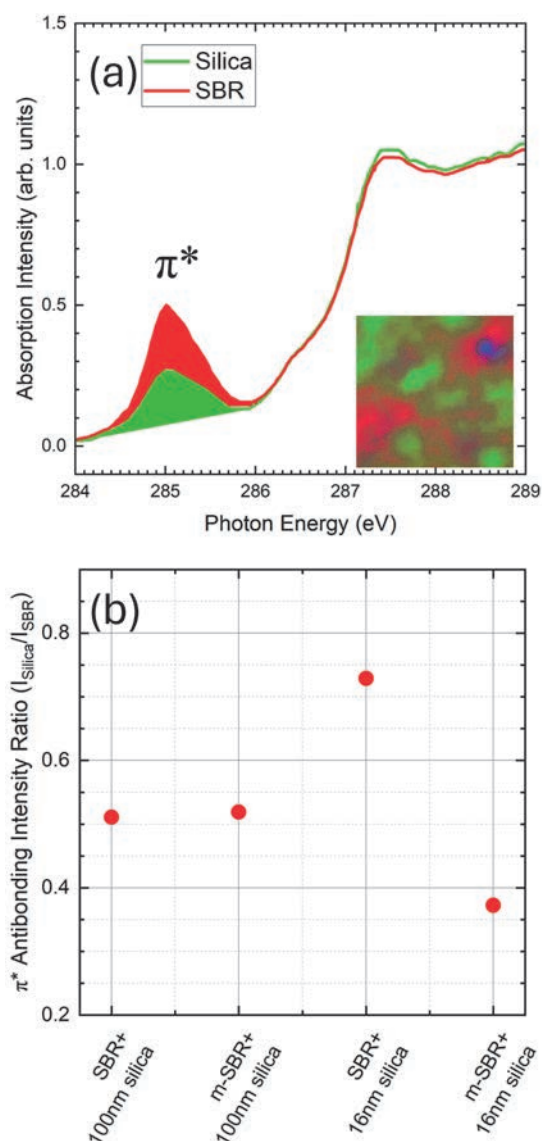


Fig. 1. (a) Analyzed STXM image and related spectra around the C-K absorption edge. The size of the inset is $2 \times 2 \mu\text{m}$. (b) Comparison of integrated peak intensity ratios of the π^* anti-bonding structure.

[1] A. J. Marzocca *et al.*, Polym. Int. **49** (2000) 216.

[2] J.M. Massie *et al.*, Rubber Chem. Technol. **66** (1993) 276.

[3] J. Jin *et al.*, Polym. Test. **99** (2021) 107212.

Investigation of Micro Voids in Rubber by STXM with a Tensile-Stress Sample Cell

T. Ohigashi^{1,2}, F. Kaneko³, H. Yuzawa⁴, T. Yano⁴, T. Araki⁴ and H. Kishimoto³

¹*Institute of Material Structure Science, High Energy Accelerator Research Organization, Tsukuba 305-0801, Japan*

²*Materials Structure Sciences, The Graduate University for Advanced Studies (SOKENDAI), Tsukuba 305-0801, Japan*

³*Sumitomo Rubber Industries Ltd., Kobe 651-0072, Japan*

⁴*UVSOR Synchrotron Facility, Institute for Molecular Science, Okazaki 444-8585, Japan*

In recent years, SDGs (Sustainable Development Goals) is a keyword in our daily life. Especially, reduction of mass consumption is a critical issue. Rubber is one of the important resources and its demand is assumed to increase especially according to growth of automobile industries. To reduce its consumption, establish of LCA (Life Cycle Assessment) of rubber industrialization and further improvement of functionality of rubbers, such as wear- and destruction-resistant, are essential.

To improve characteristics of the tire rubbers, understanding of process of the deterioration is necessary. Generally, an origin of the damage of tire rubber is chemical and mechanical issues. In recent years, Mashita et al. investigated the mechanical damage by time-resolved X-ray tomography and elucidated generation process of micro voids in a rubber pillar during its deformation [1]. On the other hand, we are using scanning transmission X-ray microscopy (STXM) to understand chemical change by mechanical damage. STXM is a powerful tool to analyze localized chemical state of a sample with high spatial resolution around 30 nm. Moreover, an advantage of STXM is relatively long working distance around 300 μm and that enables measurements in various sample environments by designing special sample cells. In this study, we designed a tensile-stress sample cell for STXM and measured a rubber sample under applied tensile stress.

The tensile-stress sample cell with a sample cartridge is shown in Fig. 1. The sample cartridge (stainless steel, 100 μm thick) was originally designed by Sato et al. [2]. Width of the gap of the sample cartridge can be adjusted manually from 300 to 850 μm in horizontal direction by a micrometer and the sample placed on the gap is stretched or relaxed. In this study, an ultra-thin slice (200 nm thick) of mixture of isoprene and butadiene rubbers was used as a sample. Figure 2 shows X-ray absorption spectra around C K-edge of the rubber with or without tensile stress. The spectra are normalized at 280 eV and $\pi^*_{\text{C-C}}$ peak at 285.2 eV. In “with tensile stress” condition, the width of the gap was 2.2 times wider than “without tensile stress” condition. In comparison of the spectra, spectral features at 285.2 eV

and 288.1 eV do not show remarkable change but σ^* peak around 292.2 eV increases with stress. An inset of Fig. 2 shows zooming up of σ^* peaks and that becomes slightly sharper with the stress. These changes may imply that stretching of the rubber makes arranging C-C bonding along stretching direction (i.e. horizontal direction). As a future plan, further investigation chemical state of the micro void which is caused by stretching is analyzed.

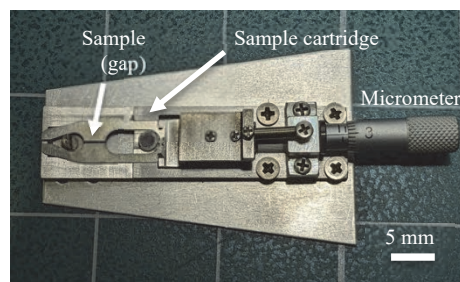


Fig. 1. Photo of the tensile-stress sample cell with the sample cartridge.

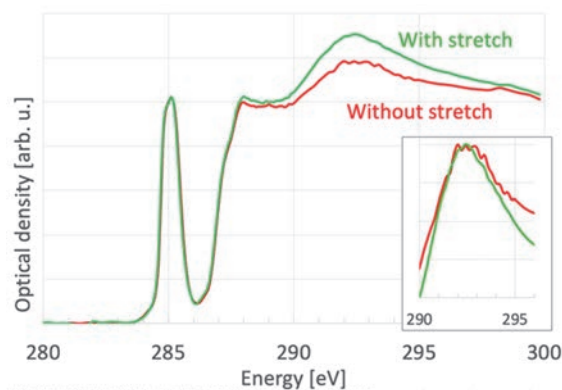


Fig. 2. X-ray absorption spectra around C K-edge of the rubber with/without stretching (normalized at 280 eV and 285.2 eV). An inset shows zooming up around σ^* peak (normalized at σ^* peak).

[1] R. Mashita *et al.*, *Sci. Rep.* **13** (2023) 5805.

[2] T. Higuchi *et al.*, *Microscopy* **67** (2018) 296.

BL4U

Electronic Structure Analysis of Electrolyte for Redox Flow Battery

E. Hosono^{1,2,3}, D. Asakura^{1,2,3}, H. Yuzawa⁴, T. Ohigashi⁵ and A. Ohira^{1,2}

¹Global Zero Emission Research Center, National Institute of Advanced Industrial Science (AIST), Tsukuba, Ibaraki 305-8569, Japan

²Research Institute for Energy Conservation, AIST, Tsukuba, Ibaraki 305-8565, Japan

³AIST-UTokyo Advanced Operando Measurement Technology Open Innovation Laboratory (Operando-OIL), Kashiwa, Chiba 277-8565, Japan

⁴UVSOR Synchrotron Facility, Institute for Molecular Science, Okazaki, Aichi 444-8585, Japan

⁵Photon Factory, Institute of Materials Structure Science, High Energy Accelerator Research Organization, Tsukuba, Ibaraki 305-0801, Japan

Effective use of renewable energy is attracting attention to realize a low-carbon society. For promoting the society of renewable energy, it is necessary to store the power generated by solar and wind etc. Thus, larger storage batteries are suitable for renewable energy power plants. These batteries are naturally required high safety, but the following characteristics are also expected: easy enlargement, long-term availability, and low cost.

We have been conducting research and development focusing on redox flow batteries as a large-scale storage battery. Redox flow batteries are nonflammable and safe because the electrolyte is an aqueous solution. In addition, they can be easily scaled up to larger capacities by increasing the size of the tank. Currently, redox flow batteries using vanadium as the electrolyte are in practical use [1-4], but further cost reduction and higher energy density are desired. Since vanadium is unevenly distributed, we have been studying redox flow batteries using Ti and Mn from the viewpoints of lower cost metal. Furthermore, higher energy density is also expected.

An important research and development element for redox flow batteries using Ti-Mn is the stability of electrolytes. Redox reaction of this system on the charging process is considered as follows.

- Negative Electrode
 $(\text{TiO})^{2+} + 2\text{H}^+ + \text{e}^- \rightarrow \text{Ti}^{3+} + \text{H}_2\text{O}$
- Positive Electrode
 $\text{Mn}^{2+} \rightarrow \text{Mn}^{3+} + \text{e}^-$
- Total Reaction
 $(\text{TiO})^{2+} + \text{Mn}^{2+} + 2\text{H}^+ \rightarrow \text{Ti}^{3+} + \text{Mn}^{3+} + \text{H}_2\text{O}$

As the electrolyte degrades during oxidation reaction, precipitates forms in the electrolyte. We conducted STXM measurement, which is effective to understand the distribution of electronic state of the electrolyte with precipitates in detail. Through this study, we hope

that it will lead to the formulation of development strategies that are important for improving the performance of redox flow batteries using Ti-Mn.

For measurement of STXM of Ti-Mn electrolyte samples, Si_3N_4 thin-film windows (100 nm) were used for separating sample from the vacuum. Charged electrolyte was investigated by STXM at BL4U of UVSOR.

Figure 1 shows spectrum at the Ti L-edge in a solution part. This spectrum is attributed to similar Ti^{4+} state. By using this measurement system, the electronic state of the transition metals in solution of the electrolyte was revealed. In addition, we conducted measurement of various electrolytes and discussed based on the obtained results.

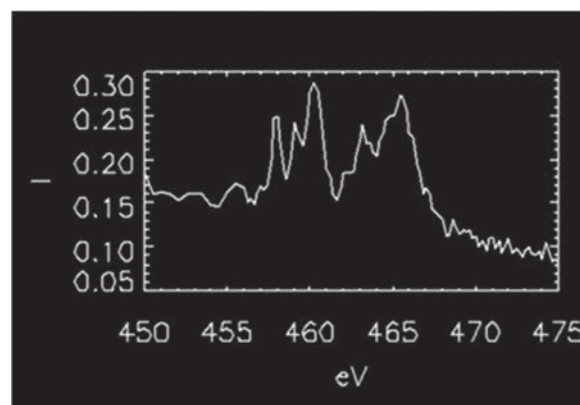


Fig. 1. Ti L-edge spectrum at a solution part in charged electrolyte.

[1] A. Z. Weber *et al.*, *J. Appl. Electrochem.* **41** (2011) 1137.

[2] M. Rychcik and M. Skyllas-Kazacos, *J. Power Sources* **22** (1988) 59.

[3] T. Shigematsu, *SEI Technical Review* **73** (2011) 4.

[4] M. Skyllas-Kazacos *et al.*, *Int. J. Energy Res.* **34** (2010) 182.

A Scanning Transmission X-ray Microscopy Study of $\text{LiFe}_{0.6}\text{Mn}_{0.4}\text{PO}_4$ Nanowires to Observe Partial Degradation by Natural Oxidation

D. Asakura^{1,2,3}, E. Hosono^{1,2,3}, H. Yuzawa⁴, T. Ohgashi⁵, W. Zhang⁶, M. Kobayashi^{7,8}, H. Kiuchi⁶ and Y. Harada^{3,6,9}

¹Global Zero Emission Research Center, National Institute of Advanced Industrial Science (AIST), Tsukuba, Ibaraki 305-8569, Japan

²Research Institute for Energy Conservation, AIST, Tsukuba, Ibaraki 305-8565, Japan

³AIST-UTokyo Advanced Operando Measurement Technology Open Innovation Laboratory (Operando-OIL), Kashiwa, Chiba 277-8565, Japan

⁴UVSOR Synchrotron Facility, Institute for Molecular Science, Okazaki, Aichi 444-8585, Japan

⁵Photon Factory, Institute of Materials Structure Science, High Energy Accelerator Research Organization, Tsukuba, Ibaraki 305-0801, Japan

⁶Institute for Solid State Physics (ISSP), The University of Tokyo, 5-1-5 Kashiwanoha, Kashiwa, Chiba 277-8581, Japan

⁷Department of Electrical Engineering and Information Systems, The University of Tokyo, 7-3-1 Hongo, Bunkyo-ku, Tokyo 113-8656, Japan

⁸Center for Spintronic Research Network, The University of Tokyo, 7-3-1 Hongo, Bunkyo-ku, Tokyo 113-8656, Japan

⁹Synchrotron Radiation Research Organization, The University of Tokyo, 7-3-1 Hongo, Bunkyo-ku, Tokyo 113-8656, Japan

$\text{LiFe}_{1-x}\text{Mn}_x\text{PO}_4$ is a cathode material for Li-ion batteries, which exhibits two potential plateaus at ~ 3.5 V vs. Li/Li^+ and ~ 4.1 V vs. Li/Li^+ on the charge-discharge curves [1]. The lower one has been attributed to the redox reaction of $\text{Fe}^{2+} \rightleftharpoons \text{Fe}^{3+}$ as with LiFePO_4 [1]. The Fe^{2+} state before charge is not so stable in air: it is easily oxidized. Then, it is well-known that the low electron conductivity of $\text{LiFe}_{1-x}\text{Mn}_x\text{PO}_4$ and LiFePO_4 is problematic for the high-rate charge-discharge performance. To overcome these problems, carbon-coated $\text{LiFe}_{0.6}\text{Mn}_{0.4}\text{PO}_4$ (LFMP) nanowires have been developed [2]. The LFMP nanowires indeed showed improvement on the high-rate performance.

To confirm the suppression of the surface oxidation by the carbon coating, we investigated the chemical state distribution of the LFMP nanowires by using scanning transmission X-ray microscopy (STXM) at BL4U [3]. The carbon-coated LFMP nanowire sample was fabricated by an electrospinning method. The nanowire sample was fixed on a Si_3N_4 membrane window with a thickness of 150 nm. The spatial resolution was around 130 nm.

Figure 1 shows an STXM optical density (OD) image at 703 eV just before the Fe L_3 -edge. It is confirmed that the diameter of the nanowires is less than 1 μm . Figure 2(a) shows the pinpoint absorption spectra of areas A(i) and A(ii) in Fig. 1(a). The areas A(i) and A(ii) are well reproduced by the charge-transfer multiplet calculations for Fe^{2+} and Fe^{3+} states, respectively. Then, we analyzed the STXM data at the Fe $L_{2,3}$ -edge by using the two calculated spectra. Figure 2(b) shows the color mapping. Most of the nanowires are colored by red that is the Fe^{2+} state. Some of the edges and most of the nanowire on the upper side are colored by green corresponding to the Fe^{3+} state. Therefore, it is

confirmed that the carbon coating effectively preserves the Fe^{2+} state, while some of the edges and some nanowires are oxidized to the Fe^{3+} state [3].

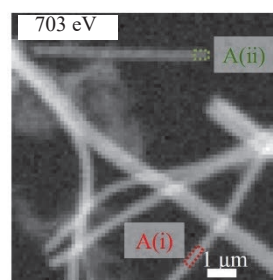


Fig. 1. A STXM OD image of the LFMP nanowire sample at 703 eV [3].

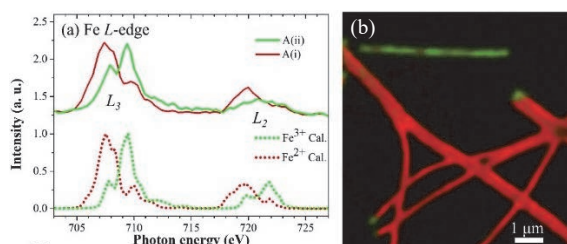


Fig. 2. (a) Pinpoint absorption spectra corresponding to areas A(i) and A(ii) in Fig. 1 and calculations for Fe^{2+} and Fe^{3+} states. (b) Color mapping of the Fe $L_{2,3}$ -edge STXM data by using the calculated spectra in (a) [3].

[1] A. Yamada *et al.*, J. Electrochem. Soc. **148** (2001) A747.

[2] K. Kagesawa, E. Hosono *et al.*, J. Power Sources **248** (2014) 615 and CrystEngComm **15** (2013) 6638.

[3] W. Zhang *et al.*, J. Electron Spectrosc. Relat. Phenom. **266** (2023) 147338.

BL4U

Hierarchically Structured $\text{ZnCo}_2\text{O}_4@\text{CoS}/\text{NF}$ Binder-Free Electrode for Multifunctional Applications

P. Mannu¹, T. T. T. Nga^{1,2}, Y.-C. Huang¹, C.-L. Dong¹, W. F. Pong¹, W.-C. Chou²,
T. Araki³ and T. Ohgashi^{3,4}

¹Department of Physics, Tamkang University, New Taipei City 25137, Taiwan

²Department of Electrophysics, National Yang Ming Chiao Tung University, Hsinchu 30010, Taiwan

³UVSOR Facility, Institute for Molecular Science, Okazaki 444-8585, Japan

⁴Photon Factory, High Energy Accelerator Research Organization, Japan

Water electrolysis is a promising technology that provides clean and sustainable energy to solve global energy crisis issues and eco-friendly degradation as the energy crisis and environmental issues produced by the over-exploitation of fossil fuels lead to unbearable problems for the growth of human society. Hence, developing a facile, environmentally friendly, and low-cost approach that can precisely regulate electrocatalysts' electronic structure and surface/ interface properties is essential. Herein, we report a high-efficiency and low-cost hydrothermal method to synthesize $\text{ZnCo}_2\text{O}_4/\text{CoS}/\text{NF}$ heterostructure electrocatalysts. The satisfactory performance was deduced that the formation of heterostructure can increase the specific surface area, form abundant oxygen vacancies, and achieve a higher proportion of $\text{Co}^{3+}/\text{Co}^{2+}$, thus providing more active sites and greatly improving its intrinsic catalytic activity (OER/HER).

STXM microscopy provides chemically and spatially resolved information and is ideal for investigating the element and region of interest in the sample. The optical density (OD) images and STXM stack maps of ZnCo_2O_4 and (b) $\text{ZnCo}_2\text{O}_4@\text{CoS}$ are presented in Figure 1a-b. The OD images (inset image) of ZnCo_2O_4 and $\text{ZnCo}_2\text{O}_4@\text{CoS}$ show three regions (R1, R2, and R3). Through the decomposition of the stack STXM maps, distinct maps are generated to depict various spectroscopic properties across the samples, including a background, as well as maps for regions colored, yellow (R1), red (R2), and green (R3) that are related with the surface area to the core region of the samples with different XAS extracted from the corresponding regions. The pre-peak of the O K-edge exhibits two features that could be associated with the hybridization of Co 3d(t_{2g})-O 2p (lower energy) and Co 3d(e_g)-O 2p orbitals (higher energy), reflecting the amount of unoccupied Co 3d states. Overall spectral evolution shows that the ratios of 3d(t_{2g})-O 2p to Co 3d(e_g)-O 2p states gradually decline from the core region to the surface area for both samples, suggesting that the hybridized 3d(t_{2g})-O 2p orbital gains some charges in the surface area, which is consistent with the charge transfer processes revealed from the combined XAS results of Co L-edge (not shown here). Especially, the intensity of the main absorption peak around 540 eV in the surface region (R-1) of $\text{ZnCo}_2\text{O}_4@\text{CoS}$ is

significantly lower than that of ZnCo_2O_4 , suggesting that the surface region of $\text{ZnCo}_2\text{O}_4@\text{CoS}$ gains even more charges than ZnCo_2O_4 does. This also suggests that the charge transfer at the surface oxygen site is not only from Zn but also from core Co, which could be further confirmed by the Co L-edge STXM-XAS.

It is believed that the intensity of O K-edge in the core region (R-3) declines more significantly in $\text{ZnCo}_2\text{O}_4@\text{CoS}$ than in ZnCo_2O_4 , suggesting the enriched electron density in the core region of $\text{ZnCo}_2\text{O}_4@\text{CoS}$, which would hinder the photoexcitation of electrons from valence band to conduction band. The overall spectral profiles of STXM-XANES of all regions of the $\text{ZnCo}_2\text{O}_4@\text{CoS}$ sample are dissimilar compared to that of ZnCo_2O_4 and consistent with the results obtained by XAS (not shown here). Notably, the pre-edge and absorption peaks of $\text{ZnCo}_2\text{O}_4@\text{CoS}$ are similar to the normal O K-edge XAS spectra. Moreover, the distinctive feature at 531.8 eV in the O K edge XANES spectra of $\text{ZnCo}_2\text{O}_4@\text{CoS}$, shown in Figure 1b, is mostly related to the hybridization of the Co 3d and O 2p state. It seems the Co sites are expected to be more active than Zn in overall better OER/HER/UOR performance of $\text{ZnCo}_2\text{O}_4@\text{CoS}$ compared to ZnCo_2O_4 .

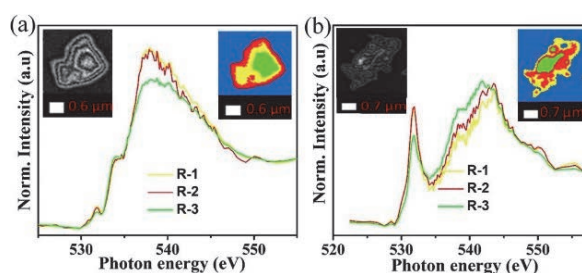


Fig. 1. STXM-XAS recorded at O K-edge of (a) ZnCo_2O_4 and (b) $\text{ZnCo}_2\text{O}_4@\text{CoS}$, STXM images show three different regions (R-1 [yellow], R-2 [red], and R-3 [green]) that are associated with surface area to the core region, the grey images of nanosheets were captured using STXM without chemical mapping.

- [1] Z. Chen *et al.*, *Nano Energy* **78** (2020) 105270.
- [2] Z. Chen, *et al.*, *Nano Res.* **13** (2020) 293.
- [3] K. Zhang and R. Zou, *Small* **17** (2021) 2100129.
- [4] W. Liu, *et al.*, *J. Catal.* **394** (2021) 50.

Unveiling the Interfacial Electronic Structure of MnO₂/CuO_x Heterostructure by Spectro-Microscopy

K. T. Arul¹, C.-L. Pan¹, H.-W. Chang², C.-L. Dong¹,
W.-F. Pong¹, T. Araki³ and T. Ohgashi^{3,4}

¹Department of Physics, Tamkang University, Tamsui 25137, Taiwan

²Department of Chemical Engineering, National United University, Miaoli 360302, Taiwan

³UVSOR Synchrotron Facility, Institute for Molecular Science, Okazaki 444-8585, Japan

⁴Photon Factory, High Energy Accelerator Research Organization, Japan

The development of renewable electricity generation technologies and novel energy storage devices are significant nowadays to tackle upcoming energy scarcity. Currently, electrochemical energy storage has fascinated because of its high cyclic stability, swift charge/discharge rate, and superior power density [1]. Recently, bimetallic oxides depicted the enhancement of pseudocapacitive performance with abundant active sites, higher cyclic stability, and augmented electrical conductivity than that of single metal oxides owing to the synergetic effects between the elements [2].

Mn and Cu-based oxides are one of the potential candidates for the electrochemical energy storage application due to their multi-valence state, high electrical conductivity, redox, and ionic conductivity. Developing the heterostructure of bimetallic oxide is important for the improvement of electrical conductivity, stability, energy, and power densities. Moreover, how the charge storage occurs in the heterostructure can pave a path for the development of next-generation materials which can be achieved by an advanced synchrotron technique. Spectro-microscopy is one of the complimentary routes to understanding site and elemental-selective spatiodynamics mapping [3]. In this study, the heterostructure of MnO₂/CuO_x was developed as a potential candidate for insight into the interfacial electronic structure and spatial mapping of the heterostructure by scanning transmission X-ray microscopy (STXM). For different reaction times, the heterostructure of MnCuO-10 (10 min) and MnCuO-40 (40 min) were developed. The electrochemical measurement showed a superior specific capacitance achieved in the heterostructure of MnCuO-40 than the other sample. To insight into the mechanism of charge storage, the STXM was performed on the heterostructure.

The optical density images and associated stack mapping STXM images for the O K-edge of (a) MnCuO-10 and (b) MnCuO-40 are shown in Fig.1. O K-edge of MnCuO-10 (red) is due to the hybridization of O 2p and Mn 3d-t_{2g} (a₁) and 3d-e_g (a₂) orbitals. The peak intensity (a₁) (green) is reduced owing to the gaining of charges by O from Mn at the interfacial

region. A feeble peak (a₃) is associated with the Cu₂O species. A broad peak (a₄) (red) was noticed because of the O 2p with the Mn 4sp character. The yellow region evidently shows CuO with minor Cu₂O species and the peak (a₂) (yellow) is due to the O 1s to O 2p that hybridized with the Cu 3d states and its intense peak (a₄) is because of the hybridization of O 2p-to-Cu 4sp which is higher than that of the other regions (green and red).

In the case of MnCuO-40, the peak (b₁) (green) is reduced due to the gaining of charges from Mn 3d-t_{2g} to O 2p. In other regions (red and yellow), the peaks b₂ and b₃ are noticed at higher energy which is similar to the spectral profile of CuO and Cu₂O respectively. The broad peak (b₄) is because of the hybridization of O 2p-to-Cu 4sp which is higher in the red region among other regions revealing the superior bulk contribution for electrochemical charge storage. Here, the interfacial and bulk regions favor the enhancement of charge storage in MnCuO-40 than the other sample.

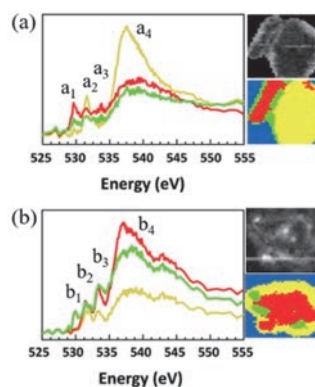


Fig. 1. Optical density images, stack-mapped STXM images, and the corresponding O K-edge XANES of (a) MnCuO-10 and (b) MnCuO-40 from different sites (green, red, and yellow).

[1] D. Sheberla *et al.*, Nat. Mater. **16** (2017) 220.

[2] N. Jabeen *et al.*, Adv. Mater. **29** (2017) 1.

[3] Y.H. Lo *et al.*, Sci. Adv. **5** (2019) 1.

BL4B

Photoresponse of C₆₀ on a Two-Dimensional van der Waals Material

Y. Nakayama^{1,2}, T. Yamada¹ and M.-K. Lin³

¹Department of Pure and Applied Chemistry, Tokyo University of Science, Noda 278-8510, Japan

²Institute for Molecular Science (IMS), Okazaki 444-8585, Japan

³National Central University (NCU), Taoyuan 320317, Taiwan

Heterojunctions between semiconducting molecules are an essential structure for organic optoelectronic devices such as organic photovoltaics, where interactions at these interfaces were generally weak van der Waals couplings. In this work, a novel van der Waals heterojunction was formed by the deposition of a molecular semiconductor C₆₀ on ultra-thin PtTe₂, one of transition metal dichalcogenide materials, to elucidate its electronic structures and photoresponse.

PtTe₂ thin-film substrates were produced in NCU by procedures reported previously [1], and then were vacuum sealed for the shipment to IMS. These were exposed to the ambient conditions for 15-30 minutes prior to introduction into a vacuum load-lock chamber of the measurement system. The sample was annealed up to 200°C for 1 h in an ultra-high vacuum chamber connected to the photoelectron spectroscopy (PES) measurement system, and C₆₀ deposition was conducted in a step-by-step manner in a high vacuum condition. Photoelectron spectroscopy measurements were performed using a system called “acceptance-cone tunable electron spectrometer” [2] at BL4B, UVSOR. The excitation photon energy was set at 40 eV, and the spectra presented here were taken in a normal emission geometry at room temperature. The secondary electron cutoff (SECO) was measured under a negative sample bias of -9 V. In order to check the photoresponse of the sample, simulated Sunlight was introduced in the measurement system from a solar simulator (HAL-320, Asahi Spectra) during the PES measurements (Fig. 1) [3].

Figure 2 shows the evolution of the PES spectra by the growth of C₆₀. The highest occupied molecular orbital (HOMO) of C₆₀ was resolved even for the 1 nm-thick film suggesting physisorption of the molecules on the PtTe₂ surface without any strong electronic couplings. The C₆₀ HOMO peak exhibited an apparent shift to the deeper binding energy side in increasing the thickness. In contrast, the vacuum level position determined by the SECO spectra stayed substantially constant during the growth of C₆₀ except initial vacuum level shift (VLS) of approximately -0.1 eV by the deposition of 1 nm-thick C₆₀, indicating an absence of any band bending in the C₆₀ overlayers. Therefore, the shift in the C₆₀ HOMO peak is plausibly attributed to the image charge screening by the PtTe₂ substrate.

Figure 3 summarizes the photoresponse of the 20 nm-thick C₆₀ on the PtTe₂ substrate. The vacuum level went down upon illumination of the simulated Sunlight by about 15 meV, while the SECO measurements on the PtTe₂ substrate before C₆₀ deposition did not show any change (green plots). The parallel energy

shift of the C₆₀ HOMO peak suggests the occurrence of the photovoltaic effect at the heterojunction.

The authors thank Prof. H. Yoshida (Chiba Univ.) for lending the solar simulator used in this study.

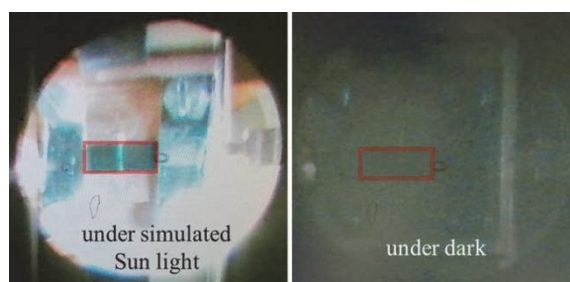


Fig. 1. Photo of the sample (marked in red).

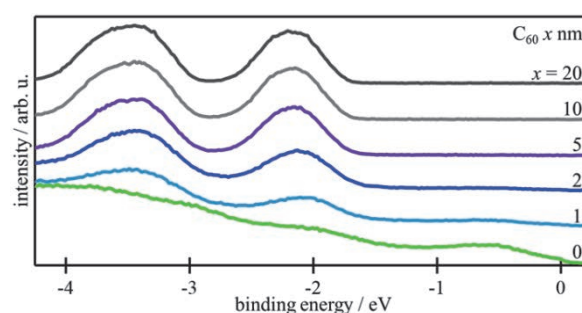


Fig. 2. PES spectra depending on the C₆₀ thickness.

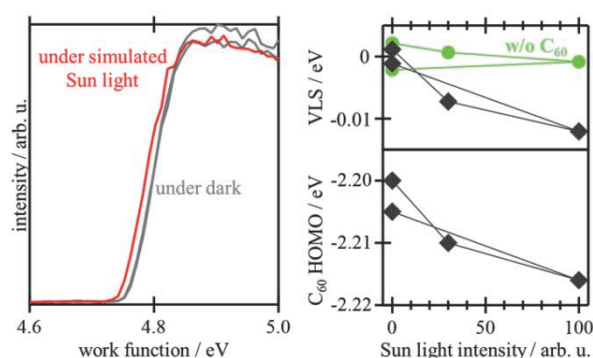


Fig. 3. (Left) SECO spectra of the 20 nm-thick C₆₀ under and without the simulated Sun light. (Right) VLS and the C₆₀ HOMO peak position plotted as a function of the simulated Sunlight intensity.

[1] M.-K. Lin *et al.*, Phys. Rev. Lett. **124** (2020) 036402.

[2] H. Yamane *et al.*, Rev. Sci. Instrum. **90** (2019) 093102.

[3] Y. Nakayama *et al.*, Adv. Energy Mater. **4** (2014) 1301354.

C K-edge XAS Measurement of Carbon-Containing Porous Silica

S. Dohshi

Osaka Research Institute of Industrial Science and Technology 2-7-1, Ayumino, Izumi, Osaka 594-1157, Japan

Compared to incandescent and fluorescent lamps, white LEDs are more environmentally friendly because they consume less power, last longer and contain no toxic substances such as mercury [1]. As a result, white LEDs have become increasingly popular in recent years. Currently, there are various methods used to create white LEDs, including the use of blue LEDs to illuminate yellow phosphors, a combination of LEDs of the three primary colors of light (red, green, and blue), or near-ultraviolet LEDs to illuminate red, green, and blue phosphors. However, these techniques are not capable of producing a continuous emission spectrum in the visible light region, which can make objects appear artificial when viewed under natural lighting conditions. Recently, mesoporous silica/resol composites were prepared by the addition of a resol solution to mesoporous silica, followed by heat treatment to prepare mesoporous silica/carbon composites. Silica/carbon composites could be also synthesized by heat treatment of rice husk. These composites were reported to exhibit continuous emission spectra in the visible light region, resulting in white emissions. These emissions are attributed to the formation of Si-C and/or Si-O-C bonds in silica. Moreover, both graphene and amorphous carbon are known to emit visible light when irradiated with UV light [2].

In addition, carbon-containing porous silica was synthesized by calcination of the denatured collagen/silica composite at 600°C for a predetermined time in air. Upon excitation with ultraviolet light, this carbon-containing porous silica emitted white light with a continuous emission spectrum throughout the visible light region [3, 4].

Several spectroscopic techniques such as UV-vis absorption, FT-IR and XPS measurements have been used to investigate the presence of carbon in porous silica, but none have been able to provide a clear explanation. This is believed to be due to the extremely low carbon content. In the present study, X-ray absorption spectroscopy, which can detect even trace amounts of carbon, was used to investigate the presence of carbon in porous silica.

C K-edge XAS measurement was performed at BL4B. The powder sample was fitted onto indium foil. The measurement was performed by fluorescence mode

(using SDD detector).

Figure 1 shows the C K-edge X-ray absorption spectra (XAF) of graphite and SiC as reference samples, and carbon-containing porous silica with different carbon contents. It is observed that the spectra of the carbon-containing porous silica differ from that of graphite and resemble that of SiC. These findings suggest that the carbon in the carbon-containing porous silica forms Si-C or Si-O-C bonds, and the white emission is a result of the presence of these bonds.

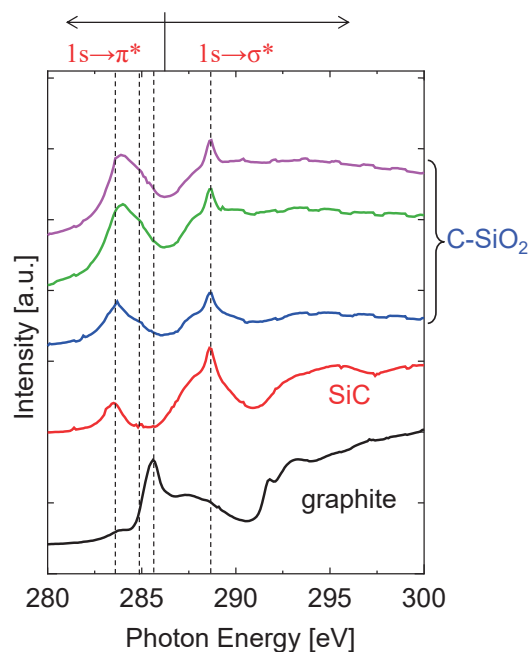


Fig. 1. C K-edge X-ray absorption spectra of graphite and SiC as reference samples, and carbon-containing porous silica with different carbon contents.

[1] T. Justel, H. Nikol and C. Ronda, *Angew. Chem. Int. Ed.* **37** (1998) 3084.

[2] Y. Ishikawa *et al.*, *Jpn. J. Appl. Phys.* **51** (2012) 01AK02.

[3] S. Dohshi, *J. Soc. Leather Technol. Chem.* **95** (2011) 200.

[4] S. Dohshi *et al.*, *J. Soc. Mater. Sci., Jpn.* **68** (2019) 549.

BL4B

Mg L_{2,3}-Edge and Al L_{2,3}-Edge XAS of MgAl₂O₄ Induced on Swift Heavy Ion Irradiations

S. Yoshioka¹, E. Kobayashi² and K. Okudaira³¹*Department of Applied Quantum Physics and Nuclear Engineering, Kyushu University, Fukuoka 819-0395, Japan*²*Kyushu Synchrotron Light Research Center, Saga 841-0005, Japan*³*Graduate school of Advanced Integration Science, Chiba University, Chiba 263-8522, Japan*

Magnesium aluminate oxide (MgAl₂O₄) is one of the common spinel compounds. Since it shows a variety of interesting physical and chemical properties, its microstructure has been extensively investigated. A cationic disordered MgAl₂O₄ spinel is represented by the formula of [Mg_{1-x}Al_x](Mg_xAl_{2-x})O₄, where the square brackets and the parentheses denote the tetrahedral and octahedral sites, respectively. The variable x is called the inversion parameter, which quantifies the cation disorder. Radiation with swift heavy ions (SHIs) interacts with materials and causes the structural change. It is therefore applied to material processing, modifications, etc. SHI irradiation provides high energy deposition through electronic stopping to the materials. SHIs in insulating solid materials are known to leave trails of damage along the ion path with a diameter of several nanometers. Structural change related to the cationic disorder has been also observed in MgAl₂O₄ with SHI irradiation using transmission electron microscopy observation. In this study, we clarify local coordination of each cation element, on which we conducted synchrotron radiation-based X-ray analysis.

Polycrystalline samples of MgAl₂O₄ were used in this study. These specimens were irradiated with 200 MeV Xe ions to fluences of 1×10¹³ cm⁻² at the H1 beamline of the tandem ion accelerator facility in the Japan Atomic Energy Agency (JAEA)-Tokai. At the beginning of each paragraph, two space characters should be inserted as an indent. Mg L_{2,3}-edge and Al L_{2,3}-edge XANES measurements were performed at the BL4B beamline of UVSOR Okazaki, Japan, using the total electron yield method (TEY). A grating monochromator gives Mg L_{2,3}-edge and Al L_{2,3}-edge in energy regions 40 - 60 eV and 60 - 80 eV, respectively. The samples were set with their surface perpendicular to the incident X-ray beam. All measurements of XANES spectra were carried out in vacuum of 1 × 10⁻⁵ Pa at room temperature.

Figure 1 show the Al L_{2,3}-edge XANES spectra of MgAl₂O₄ together with the spectra of Al₂O₃ as reference.

Compared to the spectrum of Al₂O₃, the spectrum of MgAl₂O₄ was broader and the energy positions of main peaks were clearly different. The spectral differences indicated that the local structure of Al in MgAl₂O₄ were relatively scattered. Detailed analyses on the local environment of Al and Mg in the MgAl₂O₄ are in progress by combined use of the XANES and the first principles band structure calculations.

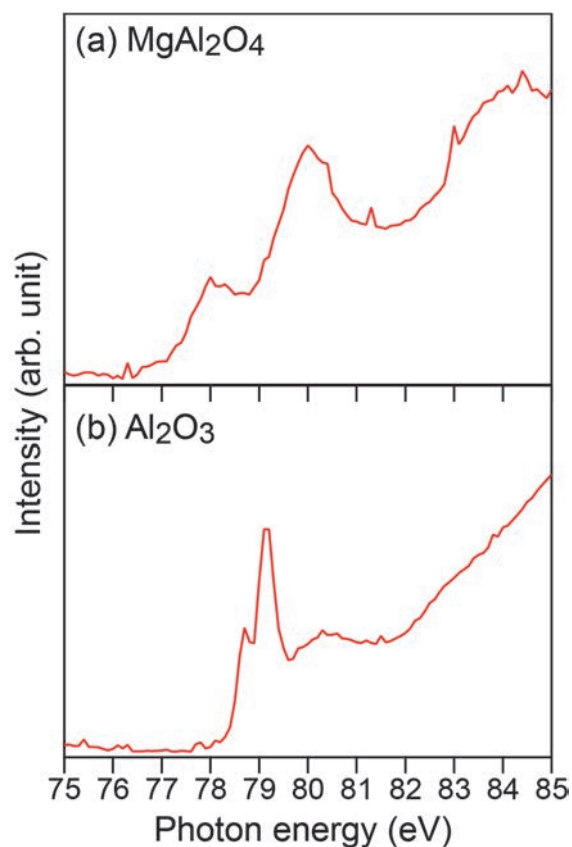


Fig. 1. Al L_{2,3}-edge XANES spectra of MgAl₂O₄ (a) and Al₂O₃ (b).

Observation of Electronic Structure of THPB/Cu(111)

H. Yamazaki¹, R. Moue¹, S. Kera², K. Fukutani², S. Makita² and K. Kanai¹

¹*Department of Physics, Faculty of Science and Technology, Tokyo University of Science, 2641 Yamazaki, Noda, Chiba 278-8510, Japan*

²*UVSOR Synchrotron Facility, Institute for Molecular Science, Okazaki 444-8585, Japan*

Topological flat bands (TFBs) exhibit exotic Bloch states with negligible band dispersion due to destructive interference of the Bloch wave function. It is known that TFBs appear in lattices with specific symmetries, such as Kagome-lattice. The TFB state is strongly localized, so that electron correlation effects have a decisive influence on the electron systems. As a result, many-body quantum phases are theoretically predicted to be realized with TFBs, exhibiting molecular quantum Hall effect, ferromagnetism and superconductivity.

So far, TFB has mostly been observed in materials with layered structures, but in these materials, it is difficult to selectively observe contributions from a single layer. To avoid this problem, this study focuses on materials with a monolayer structure, called MOFs, which consist of coordination bonds between metal atoms and organic molecules. In fact, it has been reported that TFBs were successfully observed in a two-dimensional hydrogen-bonded organic framework with 1,3,5-tris(4-hydroxyphenyl)benzene (THPB) adsorbed on Au(111) (THPB/Au(111)) [1]. Therefore, in this study, THPB/Cu(111) has been similarly investigated.

Copper is known to have high catalytic activity and is easily deposited on the surface as an adatom upon heating, which is known to combine with THPB to produce MOFs. The experiments were carried out at BL4B to fabricate THPB/Cu(111), followed by characterization of structure and electronic structure by LEED, XPS and ARPES. The LEED results showed that THPB/Cu(111) produces a well-ordered structure upon heating to 180°C. Detailed elemental composition obtained by XPS showed that heating leads to dehydrogenation of the hydroxy groups of THPB, breaking the intermolecular hydrogen bonds. However, this experiment did not confirm whether the deposited Cu and THPB actually bonded to form MOFs. As TFBs were not observed by ARPES this time, more detailed characterization of the chemical state and direct observation of the band structure of THPB/Cu(111) are planned in the future.

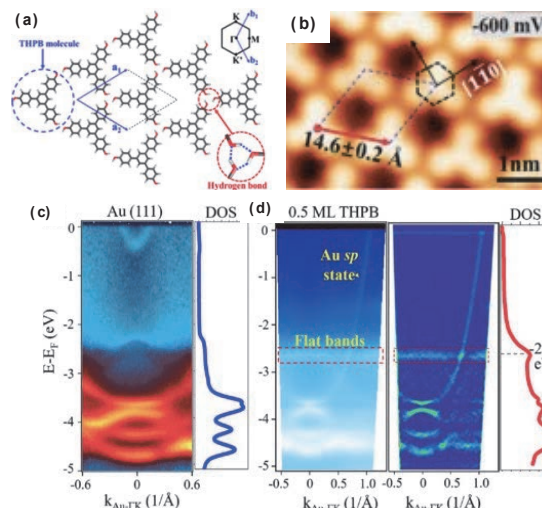


Fig. 1. THPB/Au(111) structure and band structure [1]
(a) Structure of THPB film. (b) STM image of THPB/Au(111). (c), (d) ARPES results of THPB/Au(111).

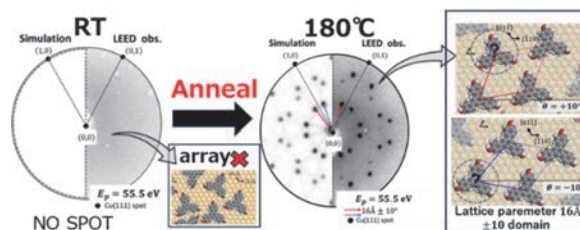


Fig. 2. LEED results for THPB/Cu(111).

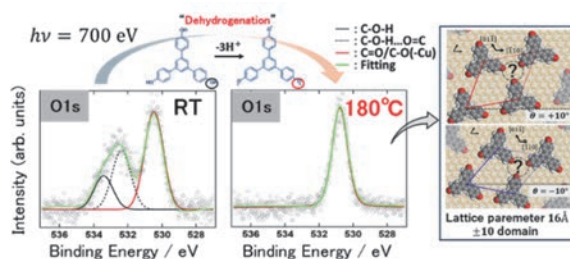


Fig. 3. XPS results for THPB/Cu(111).

[1] M. Pan *et al.*, Phys. Rev. Lett. **130** (2023) 036203.

BL4B

Photoelectron Measurements for Rubrene Derivatives on Rubrene Single Crystals

T. Yamada¹, N. Ohtsuka², N. Momiyama² and Y. Nakayama^{1,2}

¹Department of Pure and Applied Chemistry, Tokyo University of Science, Noda 278-8510, Japan

²Institute for Molecular Science, Okazaki 444-8585, Japan

Charge carrier transport in organic semiconductor materials with high mobility, such as single-crystal 5,6,11,12-tetraphenylnaphthacene (rubrene), is known to be the “band transport” [1,2]. A derivative of rubrene, 5,12-bis(4-methylphenyl)-6,11-bis[4-(trifluoromethyl)phenyl]naphthacene (fm-rubrene), was found to form a highly crystalline interface on rubrene [3], which gave rise to an expectation that the concomitance of both band transport and highly crystalline interfaces could be achieved. Therefore, we set the measurement of the valence band structures of single-crystalline fm-rubrene thin films on the rubrene single-crystal substrates as the research objective. On the other hand, charge carrier transport in molecular solids is generally affected by molecular vibrations and phonons [4], which can be deduced from the change in the electronic structures upon cooling. In this study, we tracked the demonstration of temperature-dependent changes in photoemission spectra of fm-rubrene thin-films on the rubrene single crystals.

The rubrene single crystals used were prepared by a physical vapor transport method, and fm-rubrene was deposited onto the rubrene substrates to a thickness of 20 nm at a deposition rate of 0.40 nm/s in a vacuum load-lock chamber directly connected to the photoelectron spectroscopy (PES) measurement chamber. PES measurements were performed at an excitation energy of 25 eV at BL4B, UVSOR. The photoelectrons emitted to a polar-angle θ range of -15 to 15 degrees from the surface normal were collected by an electron analyzer (A1, MB-Scientific). All photoelectron spectra shown here are photoelectron signals integrated in the θ direction. The secondary electron cutoff (SECO) was measured under a negative sample bias of -9.16 V. All PES measurements were performed with the irradiation of laser light (wavelength of 405 nm) to suppress sample charging due to the photoelectron emission [5]. The sample temperature was cooled from room temperature to 60 K for tracking the change in the PES spectra.

Figures 1 and 2 show the PES spectra in the valence band and the SECO regions, respectively, of a fm-rubrene/rubrene sample taken at different temperatures. The spectra shifted to the lower energy side upon cooling for both the valence band and the SECO regions. As shown in Fig. 2, the slope of the SECO became less steep upon cooling, suggesting a possible occurrence of the sample charging. Although the energy dispersion of the valence bands was hardly observed by the angle-resolved measurements on the present sample plausibly because fm-rubrene formed disordered

overlayers in the present condition, we are planning to prepare single-crystalline fm-rubrene at a lower deposition rate to align the crystal orientation to the single-crystal rubrene [3], and to conduct angle-resolved PES measurements for demonstrating the valence band structure of fm-rubrene in future.

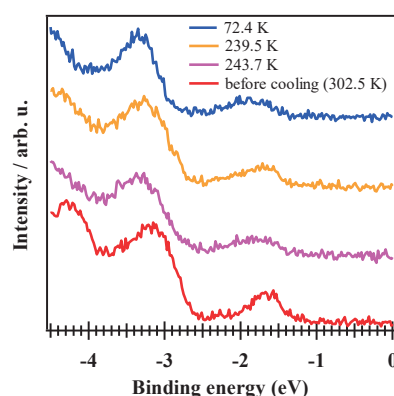


Fig. 1. Temperature-dependence of the PES spectra of the fm-rubrene/rubrene sample in the valence band region.

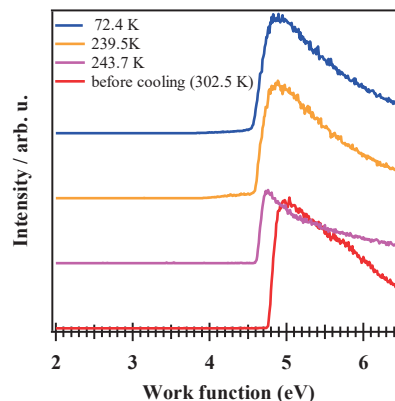


Fig. 2. SECO spectra of the fm-rubrene/rubrene sample taken at different cooling temperatures.

- [1] V. Podzorov *et al.*, Phys. Rev. Lett. **95** (2005) 226601.
- [2] D.A. da S. Filho, E.-G. Kim and J.-L. Bredas, Adv. Mater. **17** (2005) 1072.
- [3] K. Takahashi *et al.*, J. Phys. Chem. Lett. **12**, (2021) 11430.
- [4] G. Schweicher *et al.*, Adv. Mater. **31** (2019) 1902407.
- [5] S. Machida *et al.*, Phys. Rev. Lett. **104** (2010) 156401.

Local Environment of Dopants in (Co, Nb) and (Mn, Nb) Co-Doped TiO₂

H. Murata, Y. Nagatomo and A. Nakahira

Department of Materials Science, Osaka Metropolitan University, Sakai 599-8531, Japan

Titanium dioxide (TiO₂) is one of the typical fine ceramic materials. Its applications are widespread as a pigment, photo-catalyst and transparent conductor. Because the bandgap of TiO₂ is in the ultraviolet region, various kinds of dopants have been investigated to induce visible light absorption. However, the solid solution limit of most of elements in TiO₂ is small. Recently, we reported (Fe, Nb) co-doped TiO₂ has a large solid solution limit above 50 mol% of Ti due to charge compensation of Fe³⁺ and Nb⁵⁺. The shrinkage of bandgap in these materials induced visible-light response and enhanced photo-catalytic activity. The advantages of these materials are attributed to the weak d-d transition of Fe³⁺ at the octahedral site. In order to develop other elements, it is necessary to clarify the local environments and valence states of dopants in co-doped TiO₂. In this study, local environments and valence states of dopants in (Co, Nb) and (Mn, Nb) co-doped TiO₂ were investigated by X-ray absorption near edge structure (XANES).

(Co, Nb) and (Mn, Nb) co-doped TiO₂ samples were prepared by a conventional solid-state reaction method using TiO₂, Co₃O₄, Mn₂O₃ and Nb₂O₅ as starting materials. The starting materials were ground and mixed using an alumina mortar and pestle. They were calcined in an alumina crucible at 1200 °C in air for 6 h. The samples were again ground and mixed by the mortar and pestle. Then, they were calcined in an alumina crucible at 1200 °C in air for 6 h.

Obtained samples were characterized using X-ray diffraction (XRD), Ultraviolet-Visible light spectroscopy (UV-Vis) and X-ray absorption near edge structure (XANES). Co-L₃ and Mn-L₃ XANES spectra were collected using the total electron yield method with a sample current at BL4B in UVSOR (Okazaki, Japan). The X-ray beam was monochromated using gratings with groove densities of 800 l/mm. The samples were mounted on carbon tapes. Photo-catalytic activity of the samples was evaluated by degradation of methylene blue (MB).

The (Co, Nb) co-doped TiO₂ samples show reddish color. The XRD patterns of (Co, Nb) co-doped TiO₂ samples were confirmed to be rutile-type TiO₂. The maximum solid solution limit of Co in TiO₂ was attained as Ti_{1-x}(Co_xNb_{2x})O₂, which was more than 50 mol% with respect to Ti. Co-L₃ XANES of the samples showed that Co in (Co, Nb) co-doped TiO₂ is Co²⁺ at octahedral sites.

(Mn, Nb) co-doped TiO₂ samples exhibit deep brown color, which can be attributed to the spin-allowed d-d transition of Mn³⁺ at octahedral site. The XRD patterns

of the samples were assigned to rutile-type TiO₂ with peak shifts. The solid-solution of Mn in TiO₂ depends on the amounts of Nb but the Mn:Nb ratio at which the solid solution limit of Mn in TiO₂ is maximum is between 1:1 and 1:2, which implies a mixed valence state of Mn.

Figure 1 shows a Mn-L₃ XANES spectrum of Ti_{0.85}Mn_{0.06}Nb_{0.09}O₂. The spectrum of the sample has similarity to that of Mn²⁺ at octahedral site, but it also contains other components corresponding to Mn³⁺ at octahedral site. This result confirmed that both Mn²⁺ and Mn³⁺ are present in the samples, which differs from the case of (Fe, Nb) and (Ni, Nb) co-doped TiO₂ reported elsewhere. [1, 2]

MB degradation tests shows that the (Mn, Nb) co-doped TiO₂ samples have weaker photo-catalytic activity than pristine rutile-type TiO₂, which means that d-d transition of Mn³⁺ at the octahedral site does not contribute to photo-catalytic activity. This results are useful to design photo-catalytic and pigment materials.

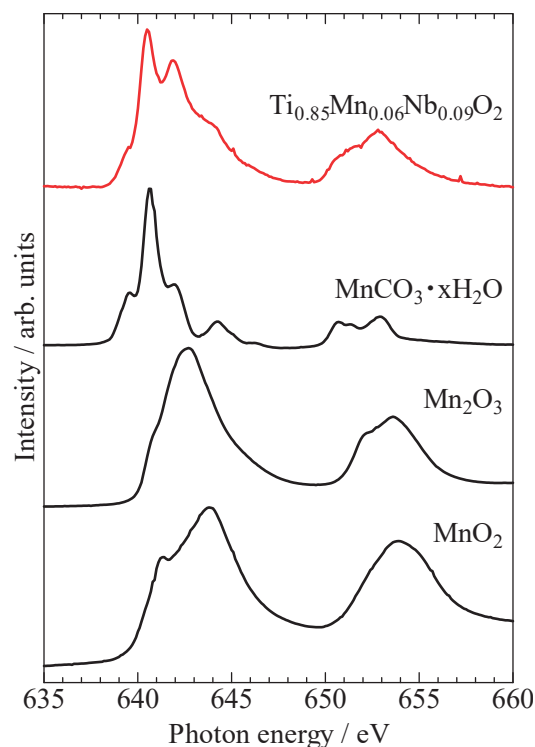


Fig. 1. Mn-L₃ XANES of Ti_{0.85}Mn_{0.06}Nb_{0.09}O₂ and reference samples.

- [1] T. Nishio *et al.*, J. Ceram. Soc. Jpn. **131** (2023) 712.
 [2] H. Murata *et al.*, UVSOR Activity Report **50** (2023) 71.

BL4B

Soft X-ray Absorption Study of Semiconductor Photocatalysts under UV Light Irradiation

T. Yoshida¹, N. Ichikuni², H. Onishi^{3,4} and Y. H. Chew³

¹Reserch Center for Artificial Photosynthesis, Osaka Metropolitan University, Osaka 558-8585, Japan

²Graduate School of Engineering, Chiba University, Chiba 263-8522, Japan

³School of Science, Kobe University, Kobe 657-8501, Japan

⁴Division of Advanced Molecular Science, Institute for Molecular Science, Okazaki 444-8585, Japan

Material conversion on semiconductor photocatalysts has been intensively studied worldwide. Downhill reactions, in which the Gibbs free energy decreases during the conversion of reactants to products, have been successfully integrated into our society [1]. Artificial photosynthesis, a category of uphill reactions involving the oxidation of water, is being developed for societal implementation in the near future [2]. In addition, fundamental studies are being conducted to uncover new scientific discoveries related to light-driven, efficient materials conversion [3].

Here, in collaboration with Prof. Hiroshi Iwayama of UVSOR, we apply soft X-ray absorption to the characterization of semiconductor photocatalysts under UV light irradiation for bandgap excitation. A series of metal oxide photocatalysts including sodium tantalate (NaTaO_3), strontium titanate (SrTiO_3), gallium oxide (Ga_2O_3), and titanium oxide (TiO_2) were investigated in two beam times in FY2023.

The photocatalyst particles were formed into disks of 7 mm diameter. The disks were placed in a vacuum chamber, irradiated with incident X-rays, and the fluorescent X-rays were detected with a silicon drift detector (SDD). The detector was capped with a 150 nm thick aluminum film (LUXEL, TF110) to minimize the contribution of stray UV light to the detector response (Fig. 1). The capping device is deposited at UVSOR. Users are encouraged to use the device when operating the SDD under UV or visible light irradiation.

Figure 2 shows a set of fluorescence yield spectra at the oxygen K-edge observed on an anatase TiO_2 photocatalyst (JRC-TIO-19 provided by the Catalysis Society of Japan) in the presence and absence of UV light provided by a Hg–Xe lamp (200 W).

In the oxygen K-edge, electron transition from $\text{O}1s$ to $\text{O}2p$ orbitals of TiO_2 particles was detected. The $\text{O}2p$ orbitals are hybridized with $\text{Ti}3d$ orbitals to form the conduction band in TiO_2 . The hybridized $\text{O}2p$ orbitals are thus split into t_{2g} and e_g levels, one at 531.5 eV and the other at 534.2 eV, according to the ligand field in TiO_6 octahedra.

The t_{2g} and e_g bands shifted to the low energy side under UV irradiation. The shifted bands induced differentiated forms in the difference spectrum shown at the bottom of Fig. 2. A possible reason for the band shifts is the conduction band partially filled with electrons excited across the band gap, where the oxidation state of some Ti cations decreased from 4+ to 3+.

The X-ray absorption of electronically excited metal oxides has been studied using ultrashort light pulses. Here, we showed that the absorption spectrum was also sensitive to steady light irradiation. This study was supported by JSPS KAKENHI (grant number 22H00344).

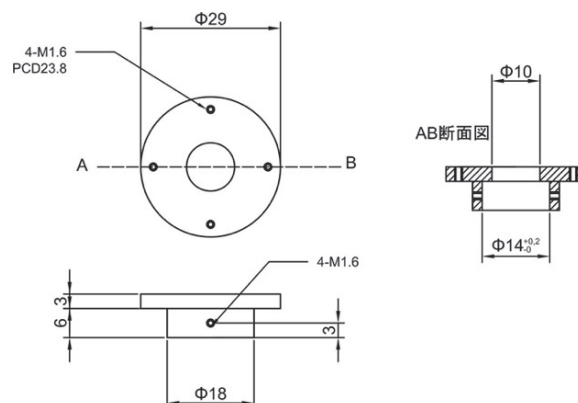


Fig. 1. A devise capping the SDD with the aluminum filter for fluorescence yield detection of oxygen K-edge absorption spectrum under UV-light irradiation.

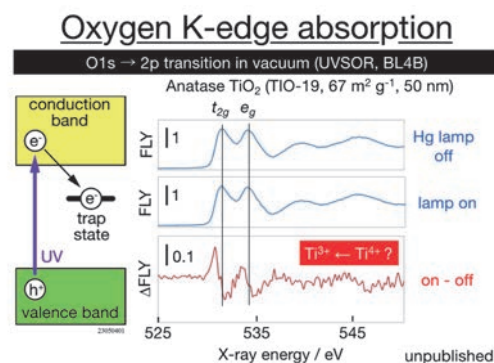


Fig. 2. Oxygen K-edge absorption spectrum of an anatase TiO_2 photocatalyst disk in the absence (upper blue spectrum) and presence (lower blue spectrum) of UV irradiation. The difference spectrum induced by the irradiation is shown in red color at the bottom.

[1] A. Fujishima *et al.*, *J. Photochem. Photobiol.*, C 1 (2000) 1.

[2] H. Onishi, *ChemSusChem* 12 (2019) 1825.

[3] C. Kranz and M. Wächtler, *Chem. Soc. Rev.* 50 (2021) 1407.

Observation of Electronic Reconstruction in Kagome Superconductors

T. Kato¹, K. Nakayama¹, Y. Li^{2,3,4}, Z. Wang^{2,3,4}, S. Souma^{5,6}, K. Tanaka^{7,8}, T. Takahashi¹,
Y. Yao^{2,3} and T. Sato^{1,5,6,9,10}

¹Department of Physics, Graduate School of Science, Tohoku University, Sendai 980-8578, Japan

²Centre for Quantum Physics, Key Laboratory of Advanced Optoelectronic Quantum Architecture and Measurement (MOE), School of Physics, Beijing Institute of Technology, Beijing 100081, P. R. China

³Beijing Key Lab of Nanophotonics and Ultrafine Optoelectronic Systems,
Beijing Institute of Technology, Beijing 100081, P. R. China

⁴Material Science Center, Yangtze Delta Region Academy of Beijing Institute of Technology,
Jiaxing 314011, P. R. China

⁵Advanced Institute for Materials Research (WPI-AIMR), Tohoku University, Sendai 980-8577, Japan

⁶Center for Science and Innovation in Spintronics (CSIS), Tohoku University, Sendai 980-8577, Japan

⁷UVSOR Synchrotron Facility, Institute for Molecular Science, Okazaki 444-8585, Japan

⁸School of Physical Sciences, The Graduate University for Advanced Studies (SOKENDAI),
Okazaki 444-8585, Japan

⁹International Center for Synchrotron Radiation Innovation Smart (SRIS), Tohoku University,
Sendai 980-8577, Japan

¹⁰Mathematical Science Center for Co-creative Society (MathCCS), Tohoku University, Sendai 980-8578, Japan

Kagome lattice provides a fertile playground to explore exotic quantum phenomena originating from intriguing interplay between electron correlation and unique band topology, as exemplified by the coexistence of topological flat band, Dirac cone band, and van Hove singularities. Among kagome lattice materials, kagome metals AV_3Sb_5 ($A = K, Rb, \text{ and } Cs$) [1] are recently attracting particular attention because of the experimental observations of fascinating properties such as possible unconventional superconductivity, charge density wave (CDW), and anomalous Hall effect. The CDW state of AV_3Sb_5 is characterized by three-dimensional lattice distortions with $2 \times 2 \times 2$ or $2 \times 2 \times 4$ periodicity. Its unconventional nature has been suggested by additional symmetry breakings inside the CDW phase. Examples include rotational symmetry breaking that is termed nematicity, additional translational symmetry breaking due to pair density wave, and time-reversal symmetry breaking. The origins of these symmetry breakings in AV_3Sb_5 are a central topic in the study of kagome lattice materials.

In this study, to search for the electronic signatures of the symmetry breakings in the CDW state, we have carried out high-resolution angle-resolved photoemission spectroscopy (ARPES) measurements of KV_3Sb_5 . High-quality single crystals of KV_3Sb_5 were grown by the self-flux method. High-resolution ARPES measurements were performed by using a MBS-A1 spectrometer at BL5U with linearly-polarized energy-tunable photons of 90-150 eV.

Figure 1 shows the second-derivative ARPES intensity at the Fermi level (E_F) measured at $T = 20$ K, well below T_{CDW} . Circular and hexagonal intensity distributions at the center and corner of the Brillouin zone, respectively, are the remnant Fermi surfaces. The former is of $Sb\ p$ orbital character and the latter is of $V\ d$ orbital character. In addition to these remnant Fermi

surfaces that are also recognized in the normal state above T_{CDW} , we found additional intensity distribution, i.e., a small pocket near the K point indicated by white dashed ellipse, which is not expected in the normal state band structure of KV_3Sb_5 [1]. This pocket shows a holelike character. According to recent studies, the formation of such hole pocket produces new nesting channel in the CDW state, possibly leading to additional symmetry breaking. To examine the validity of such a scenario, we have performed detailed temperature-dependent study across T_{CDW} and quantitative data analysis.

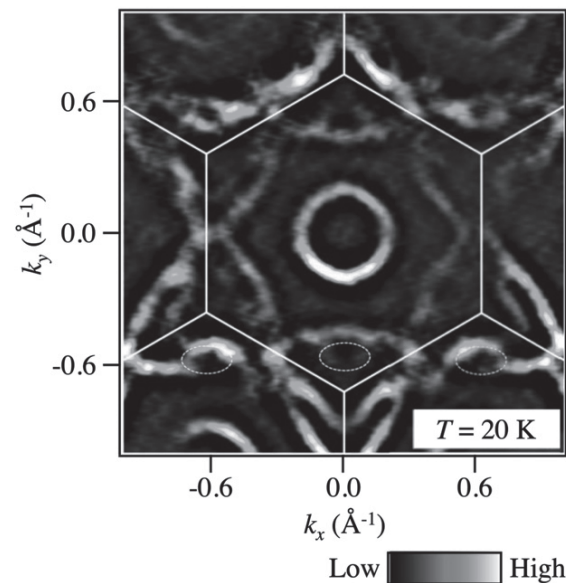


Fig. 1. Second-derivative ARPES intensity at E_F measured in the CDW state of KV_3Sb_5 .

[1] T. Kato *et al.*, Commun. Mater. **3** (2022) 30.

BL5U

ARPES Study of Monolayer Germanene Grown on Ag

T. Terasawa^{1,2}, S. Suzuki¹, D. Katsube³, S. Tanaka⁴ and K. Tanaka⁵

¹Advanced Science Research Center, Japan Atomic Energy Agency, Tokai 319-1195, Japan

²Institute of Industrial Science, The University of Tokyo, Meguro 153-8505, Japan

³Cluster for Pioneering Research, RIKEN, Wako 351-0198, Japan

⁴SANKEN, The Institute of Scientific and Industrial Research, Osaka University, Ibaraki 567-0047, Japan

⁵UVSOR Synchrotron Facility, Institute for Molecular Science, Okazaki 444-8585, Japan

Germanene, a two-dimensional honeycomb lattice composed of Ge atoms in one monolayer, has attracted attention because the ultrahigh carrier mobility and bandgap are expected to coexist in germanene [1]. To prove the existence of such fascinating characteristics of germanene, the band structure of germanene should be revealed to have the linear band dispersion (and Dirac cone) and the bandgap, which would be realized by angle-resolved photoemission spectroscopy (ARPES) on high-quality samples. However, the ARPES intensity map of germanene on Ag(111) single crystal substrates showed diffuse bands, which is attributed to the Ag and Ge hybridization and the quality of the sample [2]. In 2018, J. Yuhara *et al.* reported that the annealing and cooling processes of Ag(111) thin films on Ge(111) substrates resulted in germanene segregation [3]. In their report, scanning tunneling microscopy images showed an R30 epitaxial relation between germanene and Ag and a $7\sqrt{7} \times 7\sqrt{7}$ R19.1 superlattice, indicating the long-range order and weak interaction. Consequently, the ARPES measurements of the germanene on the Ag(111) surface have become available.

Here, we report the ARPES measurement on the segregated germanene on Ag surfaces. The Ag thin films were deposited on Ge(111) substrates in Japan Atomic Energy Agency. The sample was introduced in the load lock chamber of the BL5U beamline without any preparations. The cycles of the Ar⁺ sputtering and annealing of the samples resulted in a clean surface. After the annealing at 500°C for 30 min, germanene formed on the sample surface, as confirmed by low-energy electron diffraction. For comparison, the corrugated Ag₂Ge alloy, the so-called striped phase, was prepared by annealing the samples at 300 °C for 30 min. The ARPES measurements were carried out at 8 K using the incident light energy of 40-110 eV and the horizontal polarization. The + θ and - θ rotation of the sample corresponded to the P- and S- polarization, respectively.

Figure 1(a) shows the ARPES intensity map using 60 eV and P-polarization for Γ -M_{Ag} (equal to Γ -K_{germanene} due to the R30 epitaxial relation) of the striped phase. All the bands are assigned to those in the previous reports of the striped phase [4]. In Fig. 1(b), on the other hand, the electron pocket-like structure around the Γ point was observed for germanene samples, which is consistent with the germanene band on Al(111) [5] and entirely different from that of the striped phase. We thus concluded that we observed the band structure

of the germanene segregated on the Ag(111) thin film. Unfortunately, the Ag bulk bands overlapped on the K point of the germanene, as shown in Fig. 1(b). Further discussion is required to exclude the effect of the Ag bulk band and to reveal the electronic structure of germanene.

In summary, we carried out the ARPES measurement of germanene segregated on Ag(111) thin films deposited on Ge(111) substrates. The ARPES intensity maps showed that the germanene band structure, different from that of the striped phase, was observed. Further experiments and discussion are required to reveal whether the germanene band structure has linear band dispersion and bandgap.

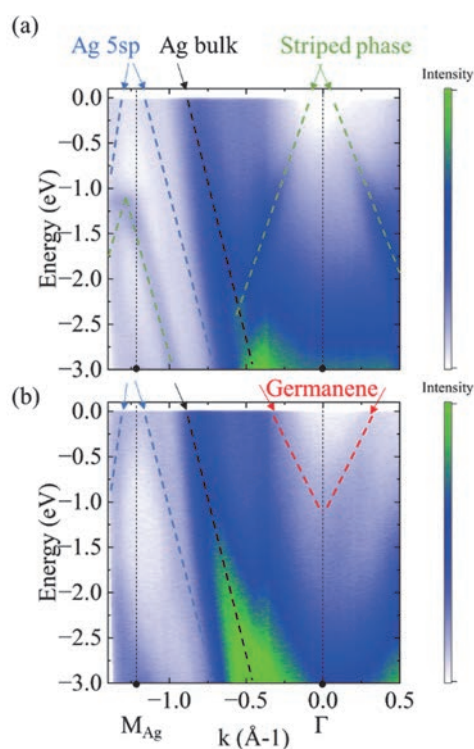


Fig. 1. (a) ARPES intensity map of striped phase and (b) germanene segregated on Ag thin film deposited on Ge(111) substrates.

- [1] C. C. Liu *et al.*, Phys. Rev. B: Condens. Matter **84** (2011) 195430.
- [2] C. H. Lin, *et al.*, Phys. Rev. Mater. **2** (2018) 024003.
- [3] J. Yuhara *et al.*, ACS Nano **12** (2018) 11632.
- [4] E. Golias *et al.*, Phys. Rev. B: Condens. Matter **88** (2013) 075403.
- [5] J. Yuhara *et al.*, 2D Mater. **8** (2021) 045039.

Pure Electron-Doping Effect in the T'-type Cuprate High-Temperature Superconductors Studied by Angle-Resolved Photoemission Spectroscopy

M. Miyamoto¹, M. Horio¹, K. Moriya², A. Takahashi³, K. Tanaka⁴, Y. Koike³, T. Adachi² and I. Matsuda¹

¹Institute for Solid State Physics, University of Tokyo, Kashiwa, Chiba 277-8581, Japan

²Department of Engineering and Applied Sciences, Sophia University, Tokyo 102-8554, Japan

³Department of Applied Physics, Tohoku University, Sendai 980-8579, Japan

⁴UVSOR Synchrotron Facility, Institute for Molecular Science, Okazaki 444-8585, Japan

Although it has been widely believed that carrier doping is necessary to induce superconductivity in cuprates, electron-doped cuprates $\text{RE}_{2-x}\text{Ce}_x\text{CuO}_{4+\delta}$ (RE: rare earth) with so-called T'-type structure do not show superconductivity without reduction annealing [1,2]. Previous studies suggested that annealing removes excess impurity oxygen atoms at the apical site [3,4]. Stronger annealing, which implies more thorough removal of apical oxygen impurities, leads to higher transition temperature T_c [5]. Horio *et al.* found that efficient annealing dramatically suppresses the pseudogap which is believed to compete with superconductivity [6]. The superconducting properties of the T'-type cuprates thus strongly depend on the degree of annealing.

On the other hand, recent studies have pointed out the importance of electron doping through annealing. ARPES studies revealed the increase of electron concentrations probably due to the creation of oxygen deficiencies in the regular sites by reduction annealing [6,7]. Song *et al.* [8] reported that the pseudogap depends only on the electron doping level after sufficient reduction annealing. Therefore, the key factor of the pseudogap and superconductivity in electron-doped cuprates remains elusive.

In order to separate the effects of annealing and electron doping on the pseudogap, we previously carried out angle-resolved photoemission spectroscopy (ARPES) measurements of the electron-doped cuprate $\text{Pr}_{1.22}\text{La}_{0.7}\text{Ce}_{0.08}\text{CuO}_4$ with doping electrons by dosing K without changing the crystal structure. Consequently, we found a signature of pseudogap suppression [9]. This time, we improved the measurement procedure to evaluate the Fermi surface and the pseudogap from a single sample within limited measurement time.

We have carried out ARPES measurements on the as-grown $\text{Pr}_{1.22}\text{La}_{0.7}\text{Ce}_{0.08}\text{CuO}_4$ sample and the annealed $\text{Pr}_{1.2}\text{La}_{0.7}\text{Ce}_{0.10}\text{CuO}_4$ at BL5U at $T=20$ K. After the K deposition, the Fermi surface of the as-grown sample originally disconnected by the pseudogap opening became almost continuous like that of the annealed sample. From the Fermi surface area, the electron concentration after K deposition amounts to ~ 0.20 , which is significantly larger than the Ce concentration of 0.08. The concomitant increase and suppression of the electron concentration and pseudogap, respectively, suggests their intimate connection, though further

quantitative evaluation is necessary to conclude the influence of apical oxygen removal through reduction annealing.

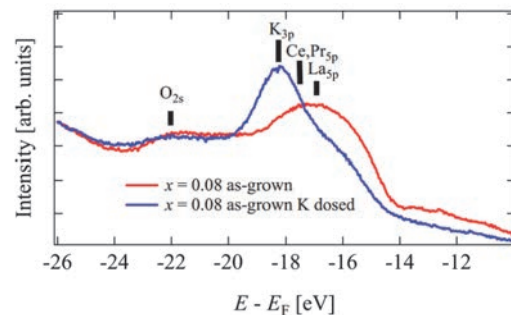


Fig. 1. Core-level photoemission Spectra of the as-grown $\text{Pr}_{1.22}\text{La}_{0.7}\text{Ce}_{0.08}\text{CuO}_4$. After potassium deposition, the K 3p peak is enhanced, which indicates K absorption on the surface of the sample.

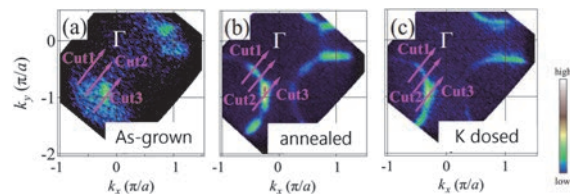


Fig. 2. Fermi surface maps for (a) the as-grown $\text{Pr}_{1.22}\text{La}_{0.7}\text{Ce}_{0.08}\text{CuO}_4$ sample, (b) the annealed $\text{Pr}_{1.2}\text{La}_{0.7}\text{Ce}_{0.10}\text{CuO}_4$ sample, and (c) the K-dosed as-grown $\text{Pr}_{1.22}\text{La}_{0.7}\text{Ce}_{0.08}\text{CuO}_4$ sample. After K dosing, the Fermi surface of the as-grown sample becomes circular like that of the annealed sample.

- [1] Y. Tokura *et al.*, Nature **337** (1989) 345.
- [2] H. Takagi *et al.*, Phys. Rev. Lett. **62** (1989) 1197.
- [3] P. Radaelli *et al.*, Phys. Rev. B: Condens. Matter **49** (1994) 15322.
- [4] A. Schultz *et al.*, Phys. Rev. B: Condens. Matter **53** (1996) 5157.
- [5] J. Kim *et al.*, Physica C **209** (1993) 381.
- [6] M. Horio *et al.*, Nat. Commun. **7** (2016) 10567.
- [7] M. Horio *et al.*, Phys. Rev. B: Condens. Matter **98** (2018) 020505.
- [8] D. Song *et al.*, Phys. Rev. Lett. **118** (2017) 137001.
- [9] M. Miyamoto *et al.*, UVSOR Activity Report **50** (2023) 98.

BL5U

Surface Electronic State of Single Crystal Mg Surface Treated by Ar Sputtering and Annealing

T. Akatsuka, H. Miyazaki, T. Tokunaga and K. Hagihara

Department of Physical Science and Engineering, Nagoya Institute of Technology,
Gokiso-cho, Showa-ku, Nagoya, Aichi 466-8555, Japan

Mg alloys with transition metals, TM, and rare earth, RE, elements, Mg–TM–RE, with a long-period stacking structure (LPSO structure) developed by Kawamura *et al.* have gained increasing attention as next-generation lightweight structural materials with high strength compared to Al alloys and flame resistance that overcomes the low ignition temperature of Mg alloys^[1,2]. The superior functionality of Mg–TM–RE is thought to be due to the formation of localized clusters of TM–RE in Mg, which affect the electronic structure of the parent phase Mg. Although the electronic structure of Mg–TM–RE has been observed by Miyazaki *et al.* using hard X-ray photoemission spectroscopy to elucidate its functionality, the detailed electronic structure near the Fermi level, which is closely related to the functionality, has not been observed^[3]. Photoelectron spectroscopy is a very promising method to directly observe the electronic structure that is the mechanism of the functionality, but it is necessary to establish a method to clean the surface in order to observe the electronic structure near the surface. Therefore, in this study, we observed the electronic structure of the Mg surface by Ar⁺ sputtering and annealing conditions in order to investigate the process of surface cleaning in Mg single crystal.

Mg (0001) single crystals were prepared by the Czochralski method. Mg (0001) single crystals were polished so that the surfaces were mirror-like. The orientation was confirmed by the back Laue method, and the sample was installed in the 3D angle-resolved photoemission spectrometer, UVSOR BL-5U. Photoelectron spectroscopy measurements were performed at 20 K. Ar⁺ sputtering and annealing were performed in the sample preparation chamber, and after surface treatment, the sample was immediately transported to the measurement chamber under ultra-high vacuum.

Initially, we attempted to remove the surface oxide layer of MgO on the Mg (0001) single crystal by repeated Ar⁺ sputtering for 30 mins with acceleration voltage of 3 kV and $P_{Ar} = 1.0 \times 10^{-4}$ Pa and annealing for 30 mins at 450 °C, but this did not remove. Therefore, we decided to perform Ar⁺ sputtering and annealing simultaneously. Figure 1 shows the photoelectron spectra of Mg 2*p* core electrons of Mg (0001) single crystals during Ar⁺ sputtering and annealing at 5, 10, and 15 hours. MgO at the binding energy $E_B = 52$ eV and the Mg 2*p* peak attributed to Mg near $E_B = 50$ eV are identified; the Mg 2*p* peak attributed to MgO gradually decreased with the sputtering and annealing

processing time. Finally, the surface oxide layer, was removed significantly compared to Mg, about 5 %. However, the Mg-attributed peaks split into two, suggesting the presence of another Mg state different from Mg-metal. Figure 2 shows the angle-resolved photoelectron spectrum after removal of the MgO surface oxide layer; a distinct energy dispersion due to the bulk state of Mg is observed, indicating that an intrinsic bulk electronic state has been obtained.

This study allowed us to determine the conditions for the removal of the surface oxide layer in Mg single crystals. However, since there are two components of the Mg core electron state, it is clear that it will be necessary to determine the further optimal processing conditions in the future.

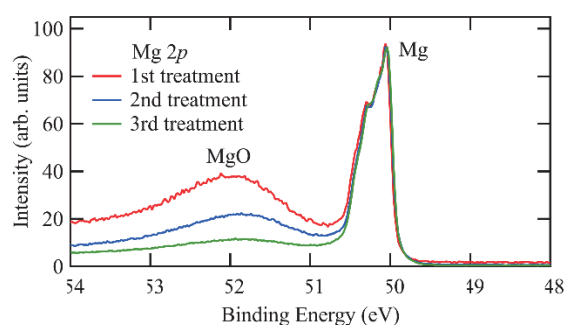


Fig. 1. Core-level photoelectron spectra of Mg 2*p* for various surface treatment conditions in Mg (0001) single crystal measured at $h\nu = 120$ eV.

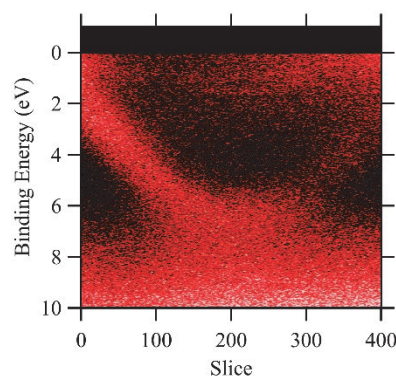


Fig. 2. Intensity mapping of angle-resolved photoemission spectra in Mg (0001) single crystals measured at $h\nu = 60$ eV.

- [1] M. A. Inoue *et al.*, *J. Mater. Res.* **16** (2001) 1894.
- [2] Y. Kawamura *et al.*, *Mater. Trans.* **42** (2001) 1172.
- [3] H. Miyazaki *et al.*, *Mater. Trans.* **64** (2023) 1194.

Measurement and Development of the Analytical Method to Determine the 3D Fermi Surface of TiSe₂

S. Tanaka

SANKEN, Osaka University, Ibaraki 464-0056, Japan

In the reciprocal space of electron momentum, the Fermi surface forms boundaries that separate the occupied and empty states. Its shape (e.g., anisotropic or isotropic) in the momentum space strongly affects the dynamical properties of matter. Therefore, methods to detect the Fermi surface are highly desirable. The photon energy dependent angle resolved photoelectron spectroscopy (ARPES) is now considered to be the most direct and convenient.

In the ARPES, the photoelectron momentum parallel to the sample surface is given by

$$k_x = \frac{\sqrt{2m_e E_k}}{\hbar} \sin \theta \cos \phi, k_y = \frac{\sqrt{2m_e E_k}}{\hbar} \sin \theta \sin \phi.$$

In the photon-energy dependent ARPES, it is assumed that the final state of the photoelectron emission is the free-electron state, and the momentum of the emitted electron can be determined as

$$k_z = \frac{\sqrt{2m_e}}{\hbar} (E_k \cos^2 \theta + V_0),$$

where V_0 (inner potential) is a fitting parameter.

Although this method is well established, the measurement of the 3D Fermi surface has rarely been performed. Its main reason seems to be that it takes huge amount of time for measurement and data. Therefore, it is necessary to develop an analytical software for this purpose, which can deal with huge data up to 100 GBytes. In this report, I describe the development of the analytical software and the results applied to a single-crystalline transition metal dichalcogenides TiSe₂.

The measurement for each ARPES was performed in the so called fix-mode with the deflector-scan, which allowed us to measure the 3D (ϕ, θ, E_k) ARPES in several minutes for each photon energy which is varied in a range of, typically, ~ 60 eV in 1 eV steps. The data were first analyzed with the automatic Fermi-Dirac fitting programs, which is necessary to determine the position of the Fermi level (in other words, the precise photon energies within errors of meV). Then, the detection efficiency of the CCD, and the photon intensity must be calibrated. After these calibrations, the photoelectron intensity just at the Fermi level is converted into the volumetric data in k_x, k_y, k_z axes. For the calibrating and converting, I wrote a specific program in Python with a help of the libraries, such as “numpy” and “scipy” (for calculation), “lmfit” (for fitting), qt and pyqtgraph (graph presentation), and so on. Especially the presentation of the volumetric 3D data is crucial, and an opengl program had to be written.

The DFT calculation is also essential. In this study, I used the Quantum Espresso codes installed in the Computer Center in the Institute for Molecular Science. Programs to handle the calculated result were also written similarly to the experimental data.

Figure 1 shows the experimental (a) and the calculated (b) 3D Fermi level. The shape around the L-point is in agreement, demonstrating the power of these methods. However, the rod-like structure around the Γ -A line is only observed in the calculation. This indicates that the Coulomb interaction works for the band near the Γ -A line, and the band gap is created even at room temperature.

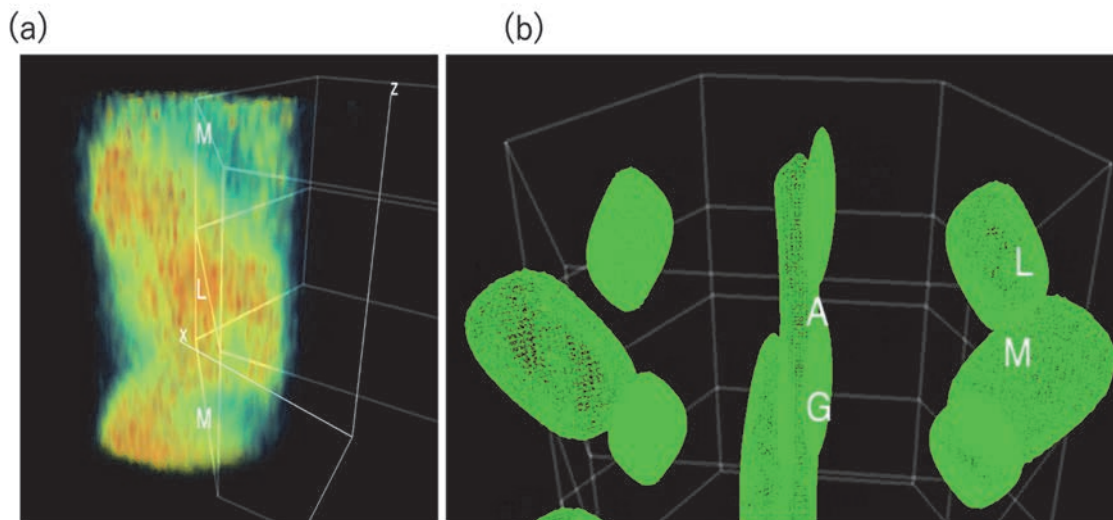


Fig. 1. (a) The experimentally determined 3D Fermi surface of TiSe₂ at room temperature. (b) Calculated Fermi Surface of TiSe₂.

BL5U

High-Resolution ARPES Study of the Electronic Structure in a Kagome Superconductor

T. Kato¹, T. Osumi¹, A. Honma¹, K. Nakayama¹, S. Souma^{2,3}, T. Takahashi¹ and T. Sato^{1,2,3,4,5}

¹Department of Physics, Graduate School of Science, Tohoku University, Sendai 980-8578, Japan

²Advanced Institute for Materials Research (WPI-AIMR), Tohoku University, Sendai 980-8577, Japan

³Center for Science and Innovation in Spintronics (CSIS), Tohoku University, Sendai 980-8577, Japan

⁴International Center for Synchrotron Radiation Innovation Smart (SRIS), Tohoku University, Sendai 980-8577, Japan

⁵Mathematical Science Center for Co-creative Society (MathCCS), Tohoku University, Sendai 980-8578, Japan

In recent years, new material phases and quantum phenomena have been explored based on the symmetry of matter, such as quantum Hall effect originating from Dirac fermions protected by chiral symmetry in graphene and quantum spin Hall effect due to spin-polarized edge states protected by nontrivial band topology and time-reversal symmetry. In this context, the kagome lattice is an intriguing structural motif because its geometric symmetry of corner-sharing triangles results in strong frustration and peculiar electronic structures such as Dirac cones, topological flat bands, and van Hove singularities. Theoretically, these characteristics have been predicted to play key roles in realizing various quantum phenomena such as spin liquids, unconventional superconductivity, density waves, and topological properties. On the other hand, due to the limited number of kagome lattice materials discovered so far, only a few phenomena, mostly magnetic ones, have been observed experimentally.

The recent discovery of superconductivity in kagome metals AV_3Sb_5 ($A = K, Rb, \text{ and } Cs$) opened the door to experimental studies in kagome lattice superconductors. Besides superconductivity, three-dimensional charge ordering has been discovered in AV_3Sb_5 , and the relationship between the mechanism of these properties and the unusual electronic states has been intensively studied. Furthermore, several new types of kagome superconductors have been discovered recently, and the study of superconductivity in the kagome lattice has become an important issue in condensed matter physics.

Here we focus on $LaRh_3B_2$, a superconductor that has been studied extensively since its discovery in the 1980s. Recently, there has been a revival of intensive study on $LaRh_3B_2$, prompted by a theory that pointed out the formation of an ideal Rh kagome lattice [1]. The replacement of La with rare-earth elements such as Ce induces ferromagnetism, which makes RRh_3B_2 a rare material family that provides a fertile playground to study the relationship between superconductivity and magnetism in the kagome lattice. However, although first-principles calculations have predicted the appearance of Dirac cone bands and flat bands protected by kagome lattice symmetry in this material, their experimental detections are still absent.

In this study, we have conducted high-resolution angle-resolved photoemission spectroscopy (ARPES)

of $LaRh_3B_2$ to directly observe its electronic band structure. High-resolution ARPES measurements were performed by using a MBS-A1 spectrometer at BL5U with linearly-polarized energy-tunable photons.

Figure 1 shows a representative ARPES result measured in the valence band region of $LaRh_3B_2$. We observed many dispersive bands such as holelike and electronlike bands centered at the Γ and M points, respectively. The observed band structure near the Γ point is reasonably explained by first-principles calculations. However, we found that the electron pockets around the M point disagree with the calculations, as suggested in previous ARPES study [2]. To clarify the origin of this disagreement and search for kagome-symmetry-related peculiar band structures, we have performed detailed photon energy and polarization dependent measurements.

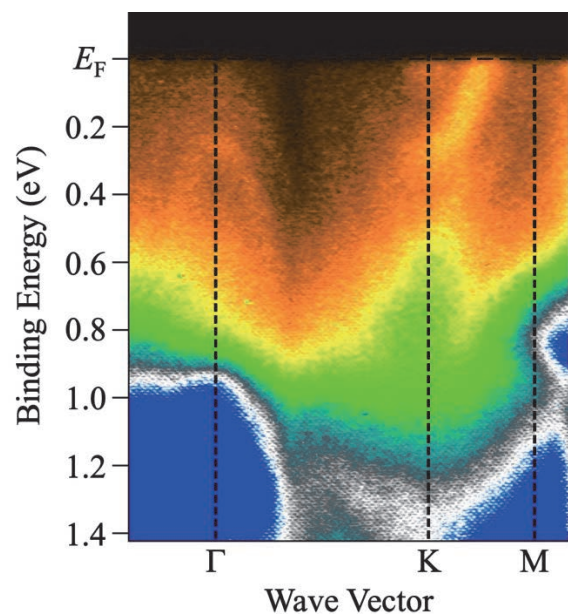


Fig. 1. ARPES intensity plot along the Γ KM line measured in the normal state of $LaRh_3B_2$.

[1] S. Chaudhary *et al.*, Phys. Rev. B: Condens. Matter **107** (2023) 085103.

[2] Y. Iida *et al.*, Physica B **351** (2004) 271.

Enantiomeric Differentiations in Chiral Ferroelectric Oxides by Angle-Resolved Photoemission Circular Dichroism

K. Fukutani^{1,2}, F. Nishino^{1,2}, S. Makita^{1,2}, K. Tanaka^{1,2} and S. Kera^{1,2,3}

¹Institute for Molecular Science, Okazaki 444-8585, Japan

²School of Physical Sciences, The Graduate University for Advanced Studies, Okazaki 444-8585, Japan

³Graduate School of Science and Engineering, Chiba University, Chiba 263-8522, Japan

Symmetry is one of the most fundamental elements interweaved in the laws of nature, which enables us to decipher a range of physical phenomena from behaviors of elementary particles to properties of solids. Recently, so-called chirality, which is a particular spatial symmetry classification arising from lack of inversion and reflection symmetries in a physical system, has been shown to play crucial roles in various exotic quantum phenomena, such as chiral nodes in topological materials, chiral phonons carrying pseudo angular momentum [1], as well as chirality-induced spin selectivity effects [2].

On the other hand, despite their conceptual simplicity and importance in quantum phenomena mentioned above, efficient differentiation between the opposite enantiomers of chiral system remains a long-standing problem. Various methods have been utilized, such as crystallography, chromatography, as well as chiroptical (absorption) spectroscopy. More, recently, photoemission circular dichroism (PECD) has attracted much attentions due to its high sensitivity to enantiomeric differences and have been used extensively for enantiomeric differentiation of chiral molecules. On the other hand, for chiral crystalline materials, the use of angle-resolved photoemission circular dichroism (CD-ARPES) has been proposed as a highly effective method of enantiomeric differentiation [3].

An interesting question in this regard is how sensitive and robust CD-ARPES is in differentiating the handedness of the crystalline material. In answering this question, we take a model case of chiral ferroelectric oxide crystal NbOI₂, for which the left-handed and the right-handed crystals differ only by the small displacements (~ 0.1 Å) of Nb atoms. Figure 1 shows the theoretical expectations on how the CD-ARPES map, $I_{CCW}(k_x, k_y) - I_{CW}(k_x, k_y)$, should generally be related between right- and left-handed crystals (enantiomers). It can be seen from the simple symmetry arguments that under the reversal of the crystalline chirality, the CD-ARPES map should undergo a sign-reversal of the CD map, followed by the reflection about the mirror plane which turns left-handed crystal into right-handed crystal or *vice versa*, as shown in the bottom panel of Fig. 1. Our experimental results on CD-ARPES at a constant energy are shown in Fig. 2 for NbOI₂, which is in excellent agreement with the theoretical expectations.

Our study demonstrates the strong sensitivity of CD-ARPES, down to sub-angstrom scale, in enantiomeric differentiations of chiral crystals.

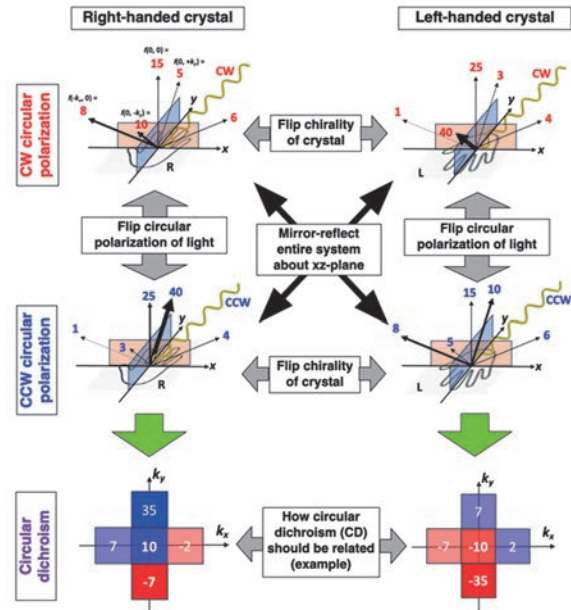


Fig. 1. [Top panel] Example schematic illustrations describing how the photoemission signals $I(k_x, k_y)$ should be related between right-handed (R) and left-handed (L) chiral crystals under the excitations of clockwise (CW) and counter-clockwise (CCW) circularly polarized lights. [Bottom panel] Schematic illustration of the resultant circular dichroism map $I_{CCW}(k_x, k_y) - I_{CW}(k_x, k_y)$.

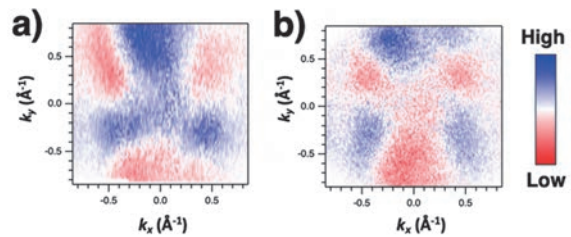


Fig. 2. Angle-resolved photoemission circular dichroism (CD-ARPES) map, $I_{CCW}(k_x, k_y) - I_{CW}(k_x, k_y)$, at a constant binding energy obtained for two samples of NbOI₂ crystals are shown in (a) and (b). The measurements were performed at $h\nu = 54$ eV at $T = 300$ K.

- [1] H. Ueda *et al.*, Nature **618** (2023) 946.
- [2] S.-H. Yang *et al.*, Nat. Rev. Phys. **3** (2021) 328.
- [3] G. H. Fecher *et al.*, Materials **15** (2022) 5812.

BL5U, 7U

Origin of High Thermopower in Heavy Fermion Yb-Based Compounds

D. Goto¹, K. Kuga¹, M. Matsunami^{1, 2, 3, 4} and T. Takeuchi^{1, 2, 3, 4}

¹Toyota Technological Institute, Nagoya 468-8511, Japan

²Research Center for Smart Energy Technology, Toyota Technological Institute, Nagoya 468-8511, Japan

³CREST, Japan Science and Technology Agency, Tokyo 102-0076, Japan

⁴MIRAI, Japan Science and Technology Agency, Tokyo 102-0076, Japan

From an energy harvesting point of view, the thermoelectric materials, which are capable of converting heat and electricity using Seebeck and Peltier effects, have been considered as one of the most promising technologies. However, thermoelectric generation has not been widely applied in our society due to its low energy conversion efficiency. For evaluating the performance of thermoelectric materials directly related to conversion efficiency, the dimensionless figure of merit $ZT = S^2T/\rho\kappa$ or the power factor $PF = S^2/\rho$ where S , ρ , and κ are the Seebeck coefficient, electrical resistivity, and thermal conductivity, respectively, of constituent materials, are frequently used [1]. Therefore, it is necessary to search for materials possessing large ZT or PF by addressing the trade-off relationship between low ρ and large $|S|$.

It is known that in intermetallic compounds called heavy fermion systems, the low ρ and large $|S|$ coexist, resulting in a large PF . This can be caused by the characteristic electronic structure formed by the hybridization between conduction and f electrons directly related to the heavy fermion nature. However, there is a serious problem concerning the sign of S , which cannot be determined solely in terms of the energy dependence of the electron density of states as in most simple metals. Therefore, the energy dependence of the relaxation time and group velocity of quasiparticles, both which are the terms in Mott formula and are neglected in many cases [1], should be taken into account.

The main purpose of this research is to establish a methodology for experimentally evaluating the energy dependence of the relaxation time and group velocity of quasiparticles in the vicinity of the Fermi level (E_F) using angle-resolved photoemission spectroscopy (ARPES). In this study, we focus on the typical heavy fermion system YbCu_2Si_2 , which is known to show relatively high large $|S|$ [2]. Generally, in the heavy fermion Yb-based compounds, the main part of $4f$ electrons and their hybridized bands locates just below E_F . This feature has high affinity with ARPES.

Single crystals of YbCu_2Si_2 were prepared by the Sn-flux method [2]. Clean (001) surface of single crystals was obtained by *in-situ* cleaving under ultra-high vacuum condition. The ARPES measurements were performed with the photon energy of 20 eV at the undulator beamline BL7U and 40, 80, and 121 eV at

BL5U of UVSOR facility.

Figure 1 shows the obtained ARPES image of YbCu_2Si_2 (001) surface at 9 K measured with the photon energy of 121 eV. In addition to the free electron-like parabolic dispersion of the (bulk) conduction bands mainly consist of Cu $3d$ electrons, the localized dispersion less Yb $4f$ bands are clearly observed in this energy range [3]. From the line width of the band dispersion near E_F providing a significant impact on the thermoelectric properties, the energy dependence of the relaxation time and group velocity of quasiparticles for YbCu_2Si_2 can be successfully evaluated.

As a future perspective, we will extend our research target to Ce-based materials to obtain comprehensive knowledge of the anomalous thermoelectric properties of heavy fermion systems, which will lead to the development of next-generation high-performance thermoelectric materials.

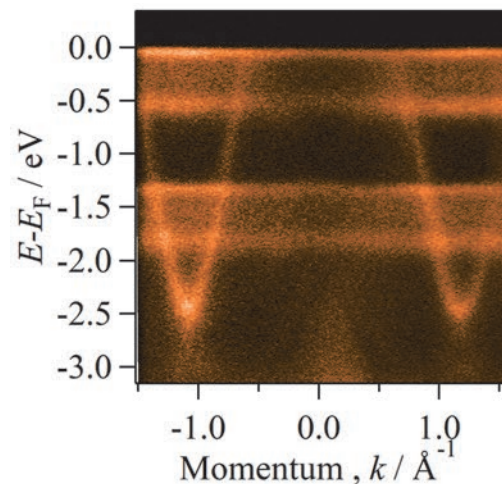


Fig. 1. ARPES image of YbCu_2Si_2 along $\bar{\Gamma} - \bar{X}$ direction at 9 K measured with the photon energy of 121 eV.

[1] T. Takeuchi, J. Thermoelectrics Soc. Jpn. **9** (2012) 1.

[2] N.D. Dung *et al.*, J. Phys. Soc. Jpn. **78** (2009) 084711.

[3] M. Matsunami *et al.*, Phys. Rev. B: Condens. Matter **87** (2013) 165141.

Angle-Resolved Photoemission Study of Layered MAX Phase Compound Zr_2SnC

M. Mita¹, K. Tanaka², M. Nakatake³, T. Ouisse⁴ and T. Ito^{1,5}

¹Graduate School of Engineering, Nagoya University, Nagoya 464-8603, Japan

²UVSOR Synchrotron Facility, Institute for Molecular Science, Okazaki 444-8585, Japan

³Aichi Synchrotron Radiation Center, Seto 489-0965, Japan

⁴Univ. Grenoble Alpes, CNRS, Grenoble INP, LMGP, F-38000 Grenoble, France

⁵Nagoya University Synchrotron Radiation Research Center (NUSR), Nagoya University, Nagoya 464-8603, Japan

MAX phase compounds, i.e., $M_{n+1}AX_n$ where M is a transition metal, A belongs to groups 13-16 and X is the C or N element, have recently been attracted much attention due to their possible application for new class of two-dimensional systems called MXenes by removing A atoms [1]. On the other hand, the bulk electronic structure of MAX phase has been studied mostly by calculations, mainly because of lack of well-established single crystalline samples. In this study, we have performed angle-resolved photoemission spectroscopy (ARPES) on MAX phase compound Zr_2SnC to investigate the systematic electronic structure change from Zr_3SnC_2 , in which Sn and Zr surface dominated electronic structure has been reported recently [2].

ARPES measurements were performed at the UVSOR-III BL5U. Data were acquired at $T = 30$ K with $h\nu = 71.5$ eV which enables us to trace around the Γ KM plane with inner potential of $V_0=20.6$ eV estimated from the photon energy dependent measurement (not shown).

Figures 1 (a) and (b) show the obtained band structure and the Fermi surface image along the $M\Gamma$ KM line of Zr_2SnC , respectively. For comparison, the band structure and Fermi surfaces of Zr_3SnC_2 obtained from measurements under identical conditions using $h\nu = 71.5$ eV are shown in Figs. 1(c) and (d), respectively. According to previous reports on Zr_3SnC_2 [2], two hole-pockets around the Γ point are attributed to the bulk-projected Fermi surfaces. On the other hand, three distinct surface-originated bands of Sn-terminated surface and Zr subsurface have been observed: the bottom of the hole-like band B1 around Γ point, the flat dispersive feature B2 just below the Fermi level (E_F) along KM lines, and the band forming a characteristic saddle like dispersion B3 around the M points (see Fig.1(f)), respectively.

From the comparison between Zr_2SnC and Zr_3SnC_2 , we have found that electronic structure of Zr_2SnC appears quite similar with one of Zr_3SnC_2 , not only for bulk projected hole-pockets but also for surface states B1, B2, and B3. On the other hand, we have found that the Fermi momenta of α , β , and SS (w-shaped electron pockets connecting with B3 along Γ M and another Fermi surface formed by B2 along Γ K line) become

smaller from Zr_3SnC_2 to Zr_2SnC , respectively. This suggests a chemical potential shift to low binding energy side, resulting in an electron-doping effect from Zr_3SnC_2 to Zr_2SnC . It should be noted that the crystal structure of Zr_2SnC becomes more three-dimensional due to the thin Zr_2C layer than the Zr_3C_2 layer. As a result, the appearance of a three-dimensional Fermi surface formed by flat electron pocket around the Γ point (or hole-like Fermi surface around the A point which has flat bottom just below E_F around the Γ point) has been expected by DFT calculation [3]. To clarify the relation between surface states and inter-layer interactions on these systems, further studies are intended.

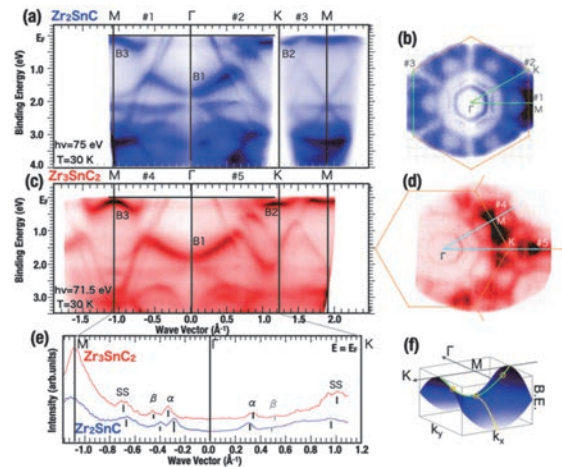


Fig. 1. (a-d) Band structures (a,c) and Fermi surface images (b,d) along the $M\Gamma$ KM line of Zr_2SnC (a,b) and Zr_3SnC_2 (c,d), respectively. ARPES measurement lines along the high-symmetry lines in Fig. 1(b) and (d) are indicated as green (#1~#3) and light blue lines (#4, 5) respectively. (e) Comparison of MCD spectra at E_F of Zr_2SnC and Zr_3SnC_2 . (f) Image of the saddle-like surface state around the M point.

[1] M. Basoum, *MAX phases* (Wiley, Weinheim 2013).

[2] T. Ito *et al.*, Phys. Rev. B: Condens. Matter **108** (2023) 235145.

[3] M. A. Hadi *et al.*, Comput. Mater. Sci **168** (2019) 203.

BL5U

ARPES Study of the CDW and Anisotropic Band Splitting in 4H-NbSe₂ and NbSeS

Y. Kumar¹, S. Ideta^{1,2} and K. Shimada^{1,2}

¹Graduate School of Advanced Science and Engineering, Hiroshima University, Hiroshima 739-0046, Japan

²Hiroshima Synchrotron Radiation Centre (HiSOR), Hiroshima University, Hiroshima 739-0046, Japan

In recent years, the study of the electronic structure of topological insulators and topological semimetals has emerged as a major research area in condensed matter physics. Recently, Dirac and Weyl Semimetals have generated great interest in spintronics due to their enriched properties [1, 2].

Layered transition-metal dichalcogenides (TMDs) AB₂ (A = transition metal, B = chalcogen) are good candidates since these materials exhibit a variety of physical properties, such as superconductivity and charge density waves (CDWs). Among these materials, 2H-NbSe₂ exhibits a unique ground state, where an incommensurate CDW and superconductivity coexist below 7 K. This makes this material ideal for studying the origin of charge density waves and to look for the interaction between superconductivity and charge density waves. Researchers have been trying to replace and dope/intercalate chemical elements and the number of atomic layers to control physical properties and to understand the relation between superconductivity and charge density waves' interaction mechanism.

We have grown high-quality single crystals of 4H-NbSe₂ and NbSeS. We have measured XRD and found that both the samples are in a single phase. We have measured the electronic band structure using ARPES at BL5U at UVSOR-III Synchrotron.

The objective of this study was to conduct ARPES measurements on 4H- NbSe₂ and NbSeS samples. The aim was to observe the material's band dispersion and Fermi surface to look for CDW and anisotropic band splitting in the electronic band structure. We have prepared 4H-NbSe₂ and NbSeS samples and aligned them in a high-symmetry direction using the Laue diffraction (XRD) available at the UVSOR facility to accurately measure the band dispersion in the high-symmetry direction.

We have cleaved several samples of 4H- NbSe₂ to obtain a clean surface but faced challenges in achieving a pristine surface, resulting in unclear band dispersion. A good cleave was observed for NbSeS samples. We have performed the ARPES experiment and mapped the fermi surface at different photon energies from $h\nu = 30$ eV to 60 eV with a 10 eV-energy step. Also, we

observe high symmetry cuts in ΓM directions to investigate the electronic band structure as shown in Fig. 1. We have performed the photon energy-dependent measurement from $h\nu = 30$ eV to 60 eV to observe the k_z dependence. We have also optimized the beam slit to improve the data quality and resolution. Further measurements of high energy resolution are needed to look for the band anisotropy and complete the data set.

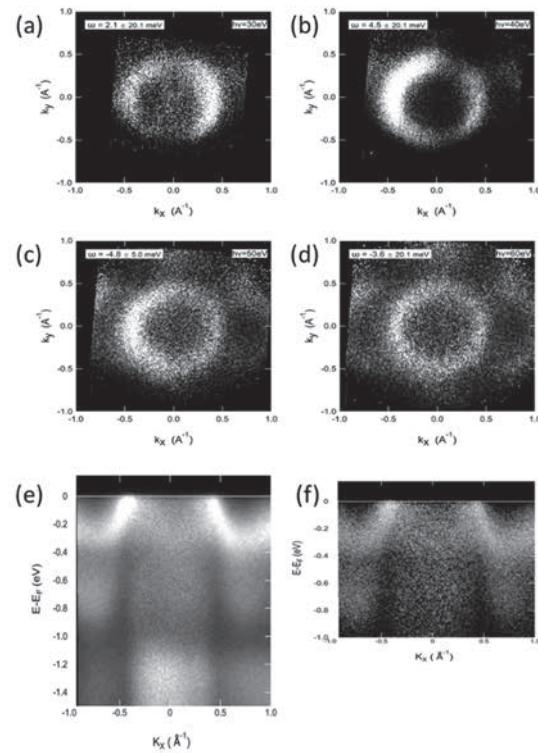


Fig. 1. Panels (a), (b), (c), and (d) show Fermi surface-mapping taken at $h\nu = 30, 40, 50,$ and 60 eV, respectively, for NbSeS samples. Panels (e) and (f) are high-symmetry cuts in the ΓM direction.

[1] N. P. Armitage, E. J. Mele and A. Vishwanath, Rev. Mod. Phys. **90** (2018) 015001.

[2] A. A. Burkov, Nat. Mater. **15** (2016) 1145.

[3] Y. Nakata *et al.*, npj 2D Mater. Appl. **2** (2018) 12.

Upgrading of the Photoelectron Momentum Microscope at BL6U of UVSOR to Integrate Data to be Reliably Analyzable by Theories

S. Suga¹, K. Hagiwara² and F. Matsui^{2,3}

¹SANKEN, Osaka University, Osaka 567-0047, Japan

²UVSOR Synchrotron Facility, Institute for Molecular Science, Okazaki 444-8585, Japan

³The Graduate University for Advanced Studies(SOKENDAI), Okazaki 444-8585, Japan

The upgraded double-hemispherical-deflection-energy-analyzer-type photoelectron momentum microscope (DHDAs-PMM) in UVSOR produced much better experimental results in 2023 than the first introduced single-HDA-type PMM in 2020. The momentum and energy resolution were much improved and systematic measurements became easier. Then measurements of the interesting materials were repeated again by this system. We have so far recognized the difficulty of theoretical analyses of the data obtained in the off-normal light incidence ($\sim 68^\circ$) because of the dipole selection rules depending upon the optical configuration including the polarization direction as well as the light incidence angle. Then we facilitated the normal incidence configuration measurement by use of the branched light from BL7U. This light is incident normally onto the sample by using the input from the back side of objective lens connected to the first HDA along the PEEM objective lens axis by properly opening the electron apertures as shown in Fig. 1. Still the spatial and momentum resolutions are realized by other apertures [1].

In particular the normal incidence configuration facilitates the reliable theoretical analyses of SP-PMM results to be obtained after the installation of a 2D spin filter to this instrument.

The results of 1T-TaS₂ by single-HDA PMM are shown in Fig. 2 in both NC- and C-CDW phases. The chirality not observed in the NC-CDW phase is recognized in the C-CDW phase at 30 K. Much clearer

fine band mapping became possible by DHDAs-PMM as will be published soon. The $(\sqrt{13}\times\sqrt{13})R13.90^\circ$ superlattice structure indicated in Fig. 3 is recognized in Fig. 2 and more clearly in recent studies by DHDAs-PMM [2], where the domain structures with opposite chirality were also recognized.

From now on fruitful SP-PMM by use of 2D spin filter must be commissioned to do the world best SP-PMM for $E_{\text{binding}}(k_x, k_y, k_z)$ measurements.

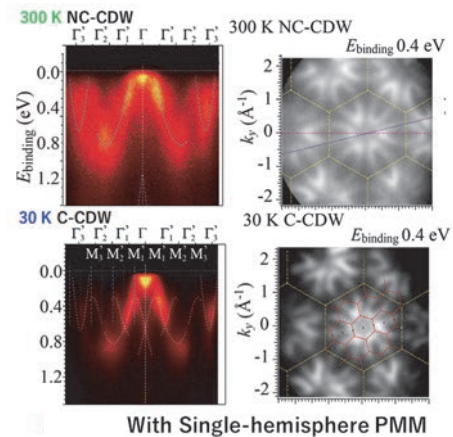


Fig. 2. 1T-TaS₂ results at 300 and 30K by single HDA PMM.

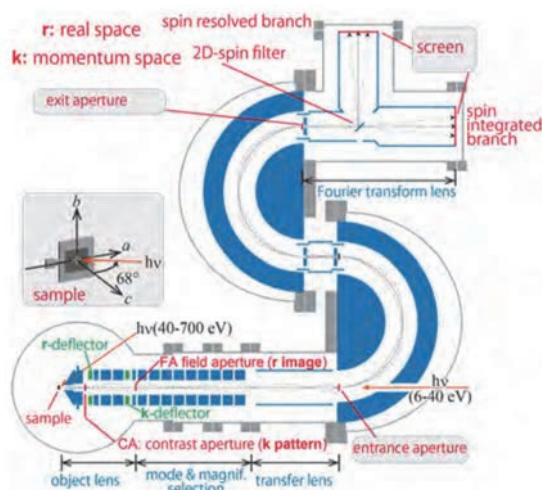


Fig. 1. Optical configuration of DHDAs-PMM for both 68° and normal incidence [1].

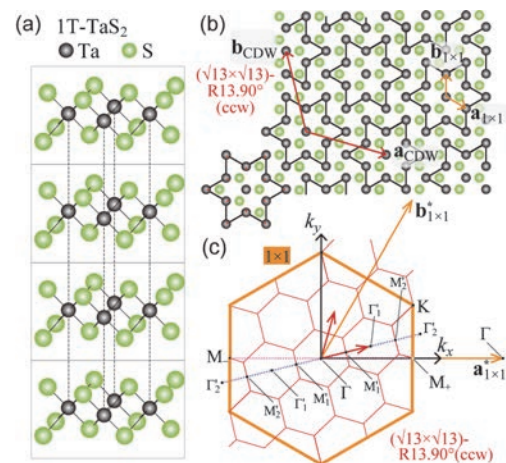


Fig. 3. Atomic structure of 1T-TaS₂. Counter-clockwise $(\sqrt{13}\times\sqrt{13})R13.90^\circ$ in C-CDW phase is shown.

[1]K. Hagiwara *et al.*, J. Synchrotron Radiat. **31** (2024) 540.

[2]F. Matsui *et al.*, to be published.

BL6U

Electronic States of a Weyl Semimetal Candidate Revealed by Momentum Microscope

Y. Morita¹, K. Nakayama¹, K. Hagiwara², F. Matsui², T. Takahashi¹, K. Kudo³ and T. Sato^{1,4,5,6,7}

¹*Department of Physics, Graduate School of Science, Tohoku University, Sendai 980-8578, Japan*

²*UVSOR Synchrotron Facility, Institute for Molecular Science, Okazaki 444-8585, Japan*

³*Department of Physics, Graduate School of Science, Osaka University, Toyonaka, Osaka 560-0043, Japan*

⁴*Advanced Institute for Materials Research (WPI-AIMR), Tohoku University, Sendai 980-8577, Japan*

⁵*Center for Science and Innovation in Spintronics (CSIS), Tohoku University, Sendai 980-8577, Japan*

⁶*International Center for Synchrotron Radiation Innovation Smart (SRIS), Tohoku University, Sendai 980-8577, Japan*

⁷*Mathematical Science Center for Co-creative Society (MathCCS), Tohoku University, Sendai 980-8578, Japan*

Recent discoveries of outstanding properties such as the half-integer quantum Hall effect in graphene and the surface Dirac electronic state of topological insulators have attracted a great deal of attention. Novel quasiparticles with energy degenerate points in the band structure often play a key role to search and demonstrate these exotic quantum phenomena and materials. For instance, graphene possesses two-dimensional Dirac fermions whose linear band dispersion degenerate at a single point in the momentum space due to chiral symmetry of the honeycomb lattice. In topological insulators, the appearance of spin-polarized two-dimensional Dirac fermions, which dominate surface conduction, is ensured by nontrivial band topology and time-reversal symmetry. Motivated by the discoveries of graphene and topological insulators, the exploration of exotic nodal fermions beyond Dirac fermions is a hot topic in condensed matter physics. An intriguing research target is Weyl fermions, a spin-polarized analogue of three-dimensional Dirac fermions. Weyl fermions are quite robust against perturbations and predicted to trigger many exotic properties such as chiral anomalies, magnetoelectric effects, and surface Fermi arcs. The realization of Weyl fermions requires the breaking of either space inversion symmetry or time-reversal symmetry. Owing to intensive research, Weyl fermions have been indeed discovered in some materials, e.g., Mn_3Si and TaAs.

Here we focus on a new Weyl-fermion material candidate, PtBi_2 which lacks the space-inversion symmetry. According to first-principles band structure calculations, Weyl fermions are located in the vicinity of Fermi level (E_F). Recent angle-resolved photoemission spectroscopy (ARPES) measurements actually reported a signature of Weyl fermions formation, though their direct observation remains a challenge. If PtBi_2 indeed hosts Weyl fermions, Fermi arc surface states should appear, and their shape are inequivalent between two opposite surfaces due to the space-inversion symmetry breaking. To clarify the Weyl material nature and the details of Fermi-arc-related physics, we determined bulk and surface electronic states over a wide momentum space using

momentum-microscopy technique at BL6U in UVSOR. For this sake, we prepared a set of crystals with two different surface terminations.

Figure 1 shows a representative equi-energy contour plot in two-dimensional momentum space, k_x and k_y . We observed the electronic structure whose periodicity matches well with the symmetry of the Brillouin zone. For example, a triangular intensity distribution is seen at each K point. We also see a six-fold symmetric characteristic intensity pattern at the Γ point. We found that, in the crystal with different termination, the intensity distribution shows remarkable differences compared to that in Fig. 1. This result indicates the presence of termination-dependent surface electronic states which might be related to Weyl-fermion physics. To investigate this point in more detail, we have performed photon-energy dependent measurements and compared the results with first-principles band structure calculations.

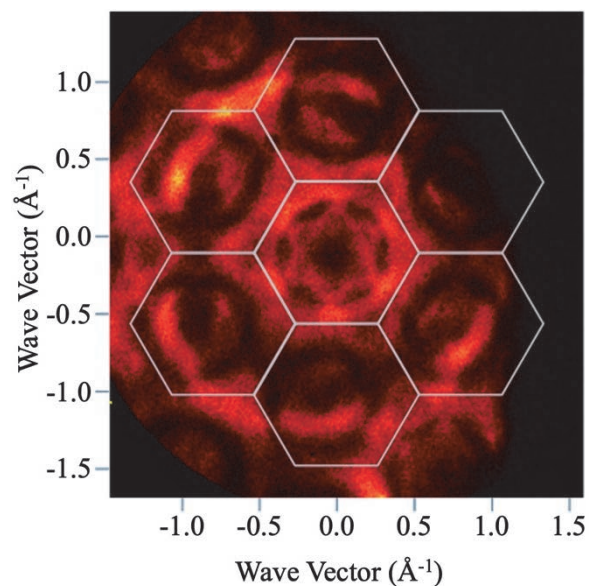


Fig. 1. ARPES intensity at a constant energy plotted as a function of two-dimensional wave vector. The measurement has been carried out using linearly polarized photons of $h\nu = 72$ eV.

Electronic Structure of a Nodal Line Semimetal IrO_2 Proved via Optical Spectroscopy

D. Hirai, K. Maruyama, Y. Kusanose and K. Takenaka
Department of Applied Physics, Nagoya University, Nagoya 464-8603, Japan

Topological semimetals have linear conduction and valence bands which intersect at points and lines each other near the Fermi energy (E_F) and exhibit unique transport properties such as ultrahigh mobility and extremely large magnetoresistance. However, at the intersections, an energy gap is often open due to spin-orbit interactions, etc. Therefore, there are only a few materials in which such characteristic electronic structures are experimentally verified. ZrSiS is one of the nodal-line semimetals whose properties have been clarified both theoretically and experimentally. It has been observed that the optical conductivity is constant over a wide photon energy range of 0.03 ~ 0.3 eV [1]. This peculiar optical property is thought to be due to interband transitions in the Dirac band near the E_F and is experimental evidence for the existence of a nodal line.

The transition-metal rutile oxide RO_2 has recently attracted attention as a candidate for nodal line semimetals. Among them, IrO_2 is predicted to have a Dirac nodal line (DNL) near the E_F , and it has been argued that the previously reported large spin Hall effect is due to the contribution of the DNL [2-4]. Although DNLs have been observed by angle-resolved photoemission spectroscopy measurements [5,6], a detailed characterization of the low-energy electronic states is needed to understand their transport properties.

In this study, in order to investigate the topological electronic structure of IrO_2 , optical reflectivity $R(\omega)$ spectra of IrO_2 single crystals in a wide energy range (from far infrared to ultraviolet) were measured. We grew high quality and large single crystals of IrO_2 by chemical vapor transport method. Normal incident reflectivity spectra were collected by using Fourier-type interferometer (0.07-2.1 eV) installed with a microscope. For the measurements in the far infrared region (0.005-0.1 eV), we used Fourier-transform infrared spectrometer (Bruker VERTEX 70V) with a synchrotron radiation at BL6B of UVSOR, Institute for Molecular Science. Optical conductivity $\sigma(\omega)$ spectra were deduced from the $R(\omega)$ using the Kramers-Kronig relation.

As shown in Fig. 1, reflectivity $R(\omega)$ of IrO_2 below 0.1 eV is close to 1, indicating the presence of high mobility carriers. There are two dips at approximately 0.6 and 2 eV, which are independent of the polarization direction, and a large decrease in reflectivity is observed. The $\sigma(\omega)$ spectra (Fig. 2) has a sharp upturn below 0.16 eV, corresponding to Drude response and three peaks at 0.5, 1.2, and 1.9 eV, possibly corresponding to inter-band transitions. On the other

hand, because of the overlap of these peaks, the energy-independent optical conductivity expected for DNL could not be observed in this study. Comparison with first-principles calculations will clarify the characteristics of DNL in the future.

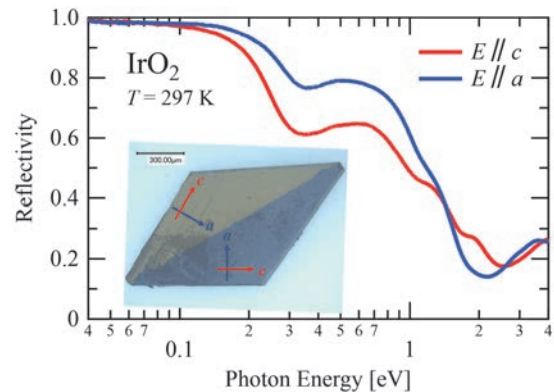


Fig. 1. Photon energy dependences of reflectance of IrO_2 at room temperature with $E \parallel a$ and c . The inset shows photograph of a single crystal of IrO_2 observed via polarized microscope, showing twin domain structure.

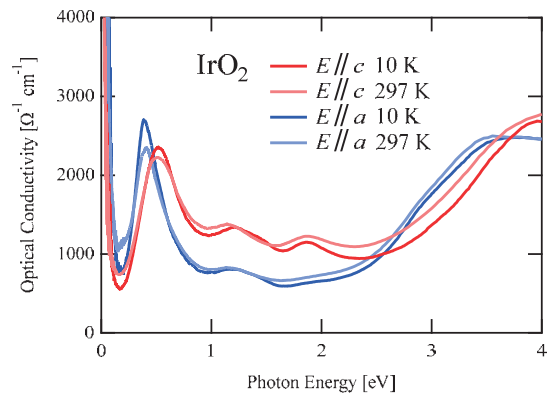


Fig. 2. Optical conductivity spectra of IrO_2 at 10 and 279 K with $E \parallel a$ and c .

- [1] M. B. Schilling *et al.*, Phys. Rev. Lett. **119** (2017) 187401.
- [2] K. Fujiwara *et al.*, Nat. Commun. **4** (2013) 2893.
- [3] Y. Sun *et al.*, Phys. Rev. Lett. **117** (2016) 146403.
- [4] Y. Sun *et al.*, Phys. Rev. B: Condens. Matter **95** (2017) 235104.
- [5] J. N. Nelson *et al.*, Phys. Rev. Mater. **3** (2019) 064205.
- [6] X. Xu *et al.*, Phys. Rev. B: Condens. Matter **99** (2019) 195106.

BL7U

ARPES Study of Pure Electronic Nematicity in Epitaxial FeSe Thin Films Grown on LaAlO₃

K. Nakayama¹, T. Kobayashi², F. Nabeshima², S. Souma^{3,4}, T. Takahashi¹,
A. Maeda² and T. Sato^{1,3,4,5,6}

¹Department of Physics, Tohoku University, Sendai 980-8578, Japan

²Department of Basic Science, the University of Tokyo, 3-8-1 Komaba, Meguro, Tokyo 153-8902, Japan

³Center for Spintronics Research Network, Tohoku University, Sendai 980-8577, Japan

⁴WPI Research Center, Advanced Institute for Materials Research, Tohoku University, Sendai 980-8577, Japan

⁵International Center for Synchrotron Radiation Innovation Smart (SRIS), Tohoku University,
Sendai 980-8577, Japan

⁶Mathematical Science Center for Co-creative Society (MathCCS), Tohoku University, Sendai 980-8578, Japan

An iron-based superconductor FeSe has attracted great attention because of its unique properties distinct from those of other iron-based superconductors, such as high-temperature superconductivity in monolayer films and extremely strong coupling superconductivity in bulk crystals. Of particular interest is the emergence of electronic nematicity characterized by the rotational symmetry breaking from C_4 in the normal state to C_2 in the nematic state. While the electronic nematicity in other iron-based superconductors develops almost simultaneously with the antiferromagnetic ordering and the tetragonal-orthorhombic structural transition, the electronic nematicity in FeSe is not accompanied by any antiferromagnetic ordering. Since the antiferromagnetic phase is located next to the superconducting phase in almost all high-temperature superconductors discovered so far, antiferromagnetic interactions have been considered a candidate to realize high-temperature superconductivity. In contrast, the results for FeSe indicate that the electronic nematicity may be the parent phase of high-temperature superconductivity. Therefore, understanding the origin of the nematic phase is an important issue to elucidate the mechanism of high-temperature superconductivity in iron-based superconductors.

Although the antiferromagnetic ordering is absent in FeSe, the tetragonal-orthorhombic transition is known to occur as in other iron-based superconductors. This indicates that the lattice in the nematic state in FeSe has the C_2 symmetry as the electronic state. Therefore, strictly speaking, the electronic state does not break the rotational symmetry of the system. In other words, it is not an ideal nematic state. In contrast, we have recently discovered that FeSe thin films fabricated on LaAlO₃ substrates exhibit pure electronic nematicity without even a structural phase transition [1].

In this study, we performed high-resolution angle-resolved photoemission spectroscopy (ARPES) measurements of FeSe/LaAlO₃ with the aim of elucidating the mechanism of the novel pure electronic nematicity. High quality FeSe/LaAlO₃ samples were prepared by pulsed laser deposition, and their clean surfaces necessary for the ARPES measurements were obtained by cleaving the samples in vacuum. High-

resolution ARPES measurements were carried out using an A1 spectrometer at BL7U in UVSOR.

Figure 1 shows the result of temperature-dependent second-derivative ARPES intensity measured at the M point of the Brillouin zone in FeSe/LaAlO₃. It is well known in FeSe that there are spin-orbit coupled d_{xz} and d_{yz} bands at the M point in the normal state, and their energy separation is enhanced upon entering the nematic state. The result plotted in Fig. 1 shows such enhancement in the energy separation between d_{xz} and d_{yz} bands below $T \sim 90$ K, where the lattice still preserves the tetragonal symmetry. This supports the emergence of the pure nematic state. We also investigated the rotational symmetry of the band dispersion and Fermi surface utilizing variable photon polarization and very high momentum resolution of low photon energies at BL7U. Through a detailed analysis of the evolution of the rotational symmetry as a function of temperature and a comparison with the results in bulk FeSe and other iron-based superconductors, we investigated similarities and differences. The obtained results are compared with theoretical models.

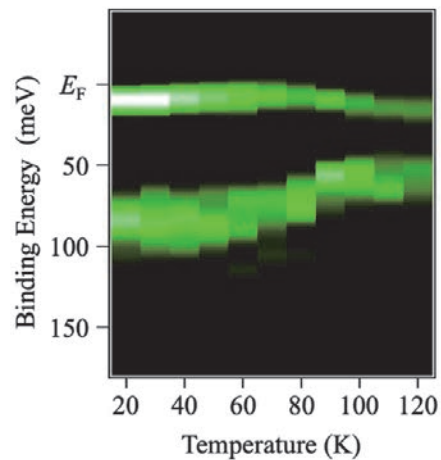


Fig. 1. Temperature dependence of ARPES intensity at the M point measured in FeSe/LaAlO₃.

[1] Y. Kubota *et al.*, Phys. Rev. B: Condens. Matter **108** (2023) L100501.

Photoemission Measurements on Crystalline Thin-Films of a Tetrabenzoporphyrin with Alkylsilyl Side Groups

Y. Nakayama^{1,2}, T. Tasaki¹, K. Teranishi³, H. Hattori¹, K. Matsuo³ and H. Yamada³

¹Department of Pure and Applied Chemistry, Tokyo University of Science, Noda 278-8510, Japan

²Institute for Molecular Science, Okazaki 444-8585, Japan

³Institute for Chemical Research, Kyoto University, Uji 611-0011, Japan

One of the most important advantages of organic semiconductor electronics is its potential for fabrication by cost-effective solution processes such as printing, roll-to-roll production, and so on. In this context, tetrabenzoporphyrins functionalized by alkylsilyl side groups are promising p-type organic semiconductor molecules because of the concomitance of the charge carrier mobility exceeding $1 \text{ cm}^2/\text{Vs}$ and good solubility [1-3]. On the other hand, to develop promising materials for the use of electronic devices, understanding the electronic structures, in particular the valence and conduction bands, of the semiconductors is indispensable. In this study, the valence electronic states of crystalline thin-films of Copper(II) 5,15-bis(*n*-octyl(dimethyl)silylethynyl)-tetrabenzoporphyrin (C8DMS-CuBP, Fig. 1) formed from its solutions [3] were measured by angle-resolved photoelectron spectroscopy (ARPES).

Crystalline thin-films of C8DMS-CuBP were produced by dip coating on Au/Si substrates pre-covered with a self-assembled monolayer at room temperature (RT). An optical micrograph image of the sample is shown in Fig. 2 inset. The samples were then introduced to the ARPES measurement system at BL7U of UVSOR. For the present measurements, the excitation photon energy was set at 8.0 eV, and the photoelectrons were collected by an electron analyzer (A-1, MB-Scientific). For the sake of canceling photoemission-induced charging of the sample, the photon flux was reduced by intentional diversion of the undulator gap width from the optimized conditions, and the sample was illuminated by a continuous-wave laser (wavelength of 405 nm) during the measurements [4]. The sample temperature was controlled in a range of 300 K – 8 K by a combination of a liquid-He flow and backside heating of the sample.

Figure 2 shows variations in the photoemission spectra of a C8DMS-CuBP thin-film depending on the sample temperature. Spectral components shifted toward the Fermi level upon cooling, while overall spectral profiles were maintained even at low temperatures. Taking into consideration that, if the photoemission-induced sample charging emerges, the spectral features are prone to be smeared out and to move away from the Fermi level, the present results indicate that the meaningful ARPES measurements unhampered by the sample charging are possible even at low temperatures, where the ARPES measurements for semiconductors generally become more difficult due to the decline in the electronic conductivity. Even

though the apparent energy dispersion of the valence bands was hardly resolved on the present samples, more accurate ARPES analyses are a future challenge.

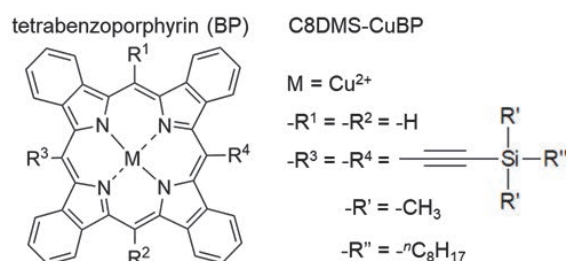


Fig. 1. Molecular structure of C8DMS-CuBP.

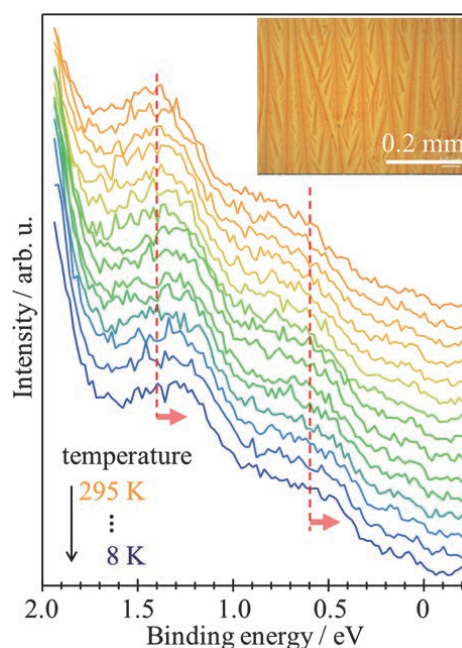


Fig. 2. Temperature-dependent evolution of the photoemission spectra of the C8DMS-CuBP crystalline thin-film sample shown in the inset image. Peak positions for the spectra obtained at RT are indicated by dashed lines.

- [1] K. Takahashi *et al.*, ACS Appl. Mater. Interfaces **9** (2017) 8211.
- [2] J. Zhu *et al.*, J. Mater. Chem. C **10** (2022) 2527.
- [3] E. Jeong *et al.*, ACS Appl. Mater. Interfaces **14** (2022) 32319.
- [4] Y. Nakayama, S. Kera and N. Ueno, J. Mater. Chem. C **8** (2020) 9090.

BL5U, 7U

Unexpected Two-Fold Symmetry of the Electronic Structure in Heavily Overdoped Bi2201 Observed by Angle-Resolved Photoemission Spectroscopy

Y. Miyai¹, S. Ideta², T. Kurosawa³, M. Oda⁴, M. Arita², K. Tanaka⁵ and K. Shimada⁴

¹Graduate School of Advanced Science and Engineering, Hiroshima University,

Higashi-Hiroshima 739-8526, Japan

²Hiroshima Synchrotron Radiation Center, Hiroshima University, Higashi-Hiroshima 739-8526, Japan

³Faculty of Science and Engineering, Muroran Institute of Technology, Muroran, 050-8585, Japan

⁴Department of Physics, Hokkaido University, Sapporo 060-0809, Japan

⁵UVSOR Synchrotron Facility, Institute for Molecular Science, Okazaki, 444-8585, Japan

High transition-temperature (T_c) cuprate superconductors have attracted much interest for their high T_c as well as unusual physical properties such as the superconducting gap, pseudogap [1], and nematicity [2]. Superconductivity occurs in the CuO_2 plane and the $\text{Cu } 3d_{x^2-y^2}$ state forms Fermi surfaces (FSs), and it has been widely believed that the CuO_2 plane shows the four-fold symmetry (C_4) so far. Recently, however, the reduction of the C_4 symmetry in the electronic structure has been reported in Bi-based high- T_c cuprate superconductors [2, 3]. Note that the breaking of the C_4 symmetry or nematicity has been also found in the electronic structure of iron-based superconductors [4]. Although, the nematicity has attracted much interest, rotational symmetry breaking in the electronic structure of high- T_c cuprate superconductors has not been directly clarified yet.

In this study, we examine the symmetry of the electronic structure of the cuprate superconductors using high-resolution angle-resolved photoemission spectroscopy (ARPES). Here, for this study, we have selected heavily overdoped Bi-based cuprates, $(\text{Bi,Pb})_2\text{Sr}_2\text{CuO}_{6+\delta}$ (Pb-Bi2201) which has a single CuO_2 plane in the unit cell. In addition, the superstructure reflections are suppressed by Pb doping. Furthermore, the pseudogap disappears in the heavily overdoped sample and one can clearly see the entire FS in the normal state.

By mechanically rotating the sample, we find the difference of the nodal distances between the two nodal directions (#1 and #2 in the inset of Fig. 1(a)) at the Fermi level (E_F). In addition, the ARPES spectral intensities at the E_F are different for these two nodal directions. To investigate many-body interactions in the direction of #1 and #2, we have evaluated the self-energies ($\Sigma^{(\#1)}$, $\Sigma^{(\#2)}$) as shown in Figs. 1(a) and 1(b) along the two nodal directions. Since the real and imaginary parts of the self-energies satisfy the Kramers-Kronig relation, the anisotropy of the self-energy should be intrinsic, indicating that the many-body interactions such as the electron-electron and electron-boson (phonon) interactions are anisotropic in these two nodal directions. Note that the observed two-fold

symmetry of the electronic structure is independent of temperature in the range of $T = 20 \text{ K} - 260 \text{ K}$.

The observed two-fold symmetry of the electronic structure may be related to a charge order formation in heavily overdoped Pb-Bi2201 as observed by resonant inelastic X-ray scattering [5]. Our results provide an insight for the intriguing physical properties such as the nematicity [2] and the ferromagnetic fluctuation of the heavily overdoped Bi2201 [6].

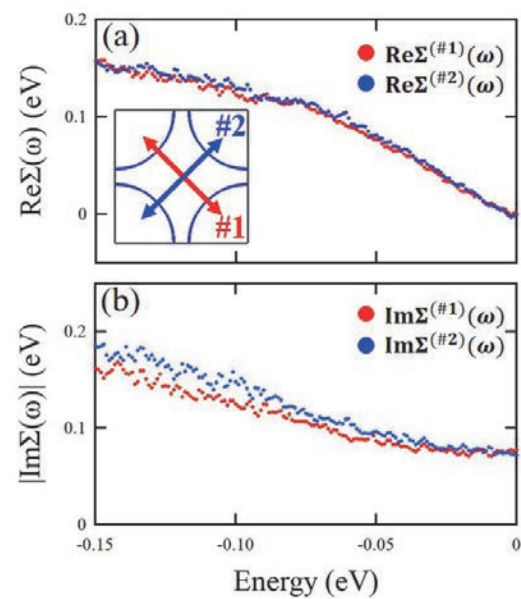


Fig. 1. Evaluation of the self-energy of Bi2201. (a), (b) Self-energy (Σ) obtained by the present study along the orthogonal two nodal directions. Red and blue dots indicate $\Sigma^{(\#1)}$ and $\Sigma^{(\#2)}$ extracted from the #1 and #2 directions as shown in the inset of panel (a), respectively.

- [1] M. Hashimoto *et al.*, Nat. Phys. **10** (2014) 483.
- [2] S. Nakata *et al.*, npj Quantum Mater. **6** (2021) 86.
- [3] N. Auvray *et al.*, Nat. Commun. **10** (2019) 5209.
- [4] H. C. Xu *et al.*, Phys. Rev. Lett. **117** (2016) 157003.
- [5] Y. Y. Peng *et al.*, Nat. Mater. **17** (2018) 697.
- [6] K. Kurashima *et al.*, Phys. Rev. Lett. **121** (2018) 057002.

Estimation of the Hole Concentration in the Normal State of Overdoped Bi2212 by Angle-Resolved Photoemission Spectroscopy

Y. Tsubota¹, Y. Miyai², S. Kumar², K. Tanaka³, S. Ishida⁴, H. Eisaki⁴,
S. Nakagawa⁵, T. Kashiwagi⁵, M. Arita², K. Shimada^{1,2} and S. Ideta^{1,2}

¹Graduate School of Advanced Science and Engineering, Hiroshima Univ., Higashi-Hiroshima 739-0046, Japan

²Hiroshima Synchrotron Radiation Center (HiSOR), Hiroshima Univ., Higashi-Hiroshima 739-0046, Japan

³UVSOR Synchrotron Facility, Institute for Molecular Science, Okazaki, Aichi 444-8585, Japan

⁴National Institute of Advanced Industrial Science and Technology (AIST), Tsukuba, Ibaraki 305-8560, Japan

⁵Graduate School of Science and Technology, Tsukuba Univ., Tsukuba, Ibaraki 305-8577, Japan

It has been known that the cuprate superconductors show a high superconducting (SC) transition temperature (T_c) and exotic physical properties. However, the SC mechanism has been unclear yet. In order to understand the mechanism of high- T_c cuprates, $\text{Bi}_2\text{Sr}_2\text{CaCu}_2\text{O}_{8+\delta}$ (Bi2212) is one of the promising candidates to study the electronic structure and reveal the physical properties. Bi2212 has two CuO_2 planes in the unit cell. Superconductivity occurs upon hole doping into the CuO_2 plane and the amount of hole doping can control T_c , and therefore, carrier doping (hole/electron concentration) plays an important key parameter in cuprates [1, 2]. The electronic phase diagram of hole-doped high- T_c cuprate superconductors plotted as a function of temperature and carrier concentration has been reported as an empirical and universal phase diagram which is a dome-like shape centered at ~ 0.16 of hole concentration [1]. However, our previous ARPES experiments suggest that its empirical phase diagram is not universal and shifted toward the overdoped region. Bi2212 has the SC gap in the anti-nodal region in the SC state, and the energy gap opens above T_c called pseudogap in the anti-nodal region in the normal state. In our previous study, the hole concentration has been quantitatively determined from the area of the Fermi surfaces, but it is difficult to determine the Fermi momentum (k_F) precisely when the energy gap is open. In order to verify the method how to estimate the hole concentration, we have measured the electronic structure of three compositions of Bi2212 in the temperature which the pseudogap is completely closed, and compared it with the hole concentration shown in the Fermi surface in the SC state.

In this study, we have performed ARPES measurements to directly investigate the electronic structure of the overdoped Bi2212. ARPES experiments were carried out at BL5U and BL7U. Samples were follows: $\text{Bi}_{2.3}\text{Sr}_{1.7}\text{CaCu}_2\text{O}_{8+\delta}$ ($T_c \sim 78$ K), $\text{Bi}_{2.1}\text{Sr}_{1.9}\text{CaCu}_2\text{O}_{8+\delta}$ ($T_c \sim 72$ K) and $\text{Bi}_{2.1-x}\text{Pb}_x\text{Sr}_2\text{CaCu}_2\text{O}_{8+\delta}$ ($T_c \sim 65$ K) in the SC and the normal states (above T^*). High quality single crystals of Bi2212 were cleaved *in-situ* in the ultrahigh vacuum $\sim 5 \times 10^{-9}$ Pa.

Figure 1 (a) shows the Fermi surface taken at $h\nu =$

17.8 eV and $T = 30$ K in the SC state for overdoped $\text{Bi}_{2.1-x}\text{Pb}_x\text{Sr}_2\text{CaCu}_2\text{O}_{8+\delta}$. Figure 1 (b) shows the Fermi surface taken at $h\nu = 17.8$ eV and $T = 150$ K in the normal state for overdoped $\text{Bi}_{2.1-x}\text{Pb}_x\text{Sr}_2\text{CaCu}_2\text{O}_{8+\delta}$.

We have analyzed the ARPES spectra from the nodal to the anti-nodal region for each sample and determined the k_F 's or each Fermi surface by fitting of momentum-distribution curves (MDCs) with single Lorentzian. Around the nodal region, k_F is defined at Fermi level (E_F) by single Lorentzian. In the off-nodal to the anti-nodal region, k_F is defined at the momentum which shows the gap minimum by single Lorentzian in the SC state. On the other hand, in the normal state (above T^*), k_F is defined at Fermi level (E_F) by single Lorentzian in the off-nodal to the anti-nodal region. The k_F points are plotted as shown by red dots (Fig. 1. (a), (b)). We have fitted Fermi-surface shape (red dots) by tight binding model (white curve) and estimated the hole concentration of each sample from the Fermi surface area and compared them quantitatively.

As a result, the Fermi-surface shapes observed by the SC and normal states in each composition can be fitted with the same tight binding parameters, and there is no significant change in the shape of the Fermi surface observed in temperature.

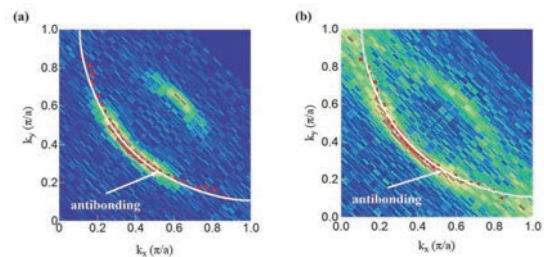


Fig. 1. (a) Fermi surface of overdoped $\text{Bi}_{2.1-x}\text{Pb}_x\text{Sr}_2\text{CaCu}_2\text{O}_{8+\delta}$ in the superconducting state ($T = 30$ K). (b) Fermi surface of overdoped $\text{Bi}_{2.1-x}\text{Pb}_x\text{Sr}_2\text{CaCu}_2\text{O}_{8+\delta}$ in the normal state ($T = 150$ K, above T^*).

[1] J. L. Tallon *et al.*, Phys. Rev. B: Condens. Matter **51** (1995) 12911.

[2] I. M. Vishik *et al.*, PNAS **6** (2012) 18332.

BL7U

Electronic Structure of Garnet-Type Solid Electrolytes $\text{Li}_{6.5}\text{La}_3\text{Zr}_{1.5}\text{Ta}_{0.5}\text{O}_{12}$ Bulk Single Crystal

K. Masuda¹, S. Koyama¹, S. Takakura², M. Nakatake³, K. Tanaka⁴, K. Kataoka⁵, J. Akimoto⁵,
Y. Iriyama¹ and T. Ito^{1,2}

¹Graduate School of Engineering, Nagoya University, Nagoya 464-8603, Japan

²Nagoya University Synchrotron Radiation Research Center (NUSR), Nagoya University,
Nagoya 464-8603, Japan

³Aichi Synchrotron Radiation Center, Seto 489-0965, Japan

⁴UVSOR Synchrotron Facility, Institute for Molecular Science, Okazaki 444-8585, Japan

⁵National Institute of Advanced Industrial Science and Technology (AIST), Ibaraki 305-8565, Japan

With the recent expansion of the use of lithium-ion secondary batteries, development of all-solid-state batteries using lithium-ion conductive inorganic solid electrolytes has been progressing to realize further safety, high energy density, and high output, etc. On the other hand, the valence-band electronic structure, which is essential to understand the relation between lithium-ion and electron conductivity in inorganic solid electrolytes, has not been well elucidated yet, though the chemical analysis using operando X-ray photoemission has intensively been applied on the system [1,2]. To clarify the effect of lithium on the electronic structure of solid electrolytes, we have performed angle-resolved photoemission spectroscopy (ARPES) measurements on garnet-type solid electrolytes $\text{Li}_{6.5}\text{La}_3\text{Zr}_{1.5}\text{Ta}_{0.5}\text{O}_{12}$ (LLZTO) in which high Li ion conductivity (1.27×10^{-3} S/cm) along the looped pathway due to the shorter Li-Li distance and deficient Li-site arrangement at room temperature have been reported [3].

ARPES measurements were performed at the UVSOR-III BL7U. Data were acquired at room temperature with $h\nu = 31$ eV which enables us to trace around the ΓMX plane with inner potential of $V_0=10.2$ eV estimated from the photon energy dependent measurement (not shown). To minimize spectral modulation due to photo-irradiation, photon flux was sufficiently reduced ($<3\text{E}+10$ photons/s) during all measurements. Single crystals were cleaved *in situ* along (011) plane.

Figure 1 (a) and (b) show ARPES spectra and band structure along the ΓM line of LLZTO, respectively. We have found that the valence band electronic structure of LLZTO is formed by a broad peak feature around 6 eV with a peak width of about 3.5 eV. This broad feature exhibits weak dispersive characteristics as a function of momentum (angle). Through a qualitative assessment of the continuous energy shift and intensity changes observed in broad peak and shoulder features, we anticipate the possible existence of several bands, as indicated by the gray lines in Fig. 1(a) and (b) respectively.

Figure 1 (c) and (d) show the DFT PDOS and band structure along the ΓM line of tetragonal $\text{Li}_7\text{La}_3\text{Zr}_2\text{O}_{12}$ with space group $I4_1/acd$ [4]. From the comparison between ARPES and calculations, we observe that the

valence band width of DFT appears to be similar to the observed spectral peak width. Furthermore, the energy positions of three peaks on PDOS of O orbital components seem to be consistent with the overall peak dispersions expected from the present ARPES. However, it remains challenging to resolve the complex band dispersion resulting from the overlap of numerous states. These results suggest the potential utility of ARPES for investigating the electronic structure of solid electrolytes single-crystals.

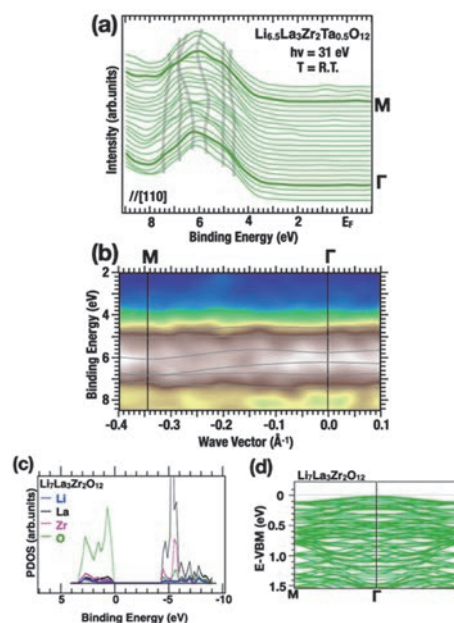


Fig. 1. (a, b) ARPES spectra (a) and band structures (b) along the ΓM line of $\text{Li}_{6.5}\text{La}_3\text{Zr}_{1.5}\text{Ta}_{0.5}\text{O}_{12}$. Solid lines are guides for eyes. (c, d) The partial density of states (c) and band structure along the ΓM line of $\text{Li}_7\text{La}_3\text{Zr}_2\text{O}_{12}$ [4].

[1] K. Hikima *et al.*, *Commun. Chem.* **5** (2022) 52.

[2] K. N. Wood *et al.*, *Nat. Commun.* **9** (2018) 2490.

[3] K. Kataoka and J. Akimoto, *ChemElectroChem* **5** (2018) 2551.

[4] The Materials Project. *Materials Data on $\text{Li}_7\text{La}_3\text{Zr}_2\text{O}_{12}$ by Materials Project*. United States: N. p., 2020. Web. doi:10.17188/1313215.

ARPES Study of the Coexistence of Superconductivity and Pure Electronic Nematicity in FeSe Thin Films on LaAlO₃

K. Nakayama¹, T. Kobayashi², F. Nabeshima², S. Souma^{3,4}, T. Takahashi¹,
A. Maeda² and T. Sato^{1,3,4,5,6}

¹Department of Physics, Tohoku University, Sendai 980-8578, Japan

²Department of Basic Science, the University of Tokyo, 3-8-1 Komaba, Meguro, Tokyo 153-8902, Japan

³Center for Spintronics Research Network, Tohoku University, Sendai 980-8577, Japan

⁴WPI Research Center, Advanced Institute for Materials Research, Tohoku University, Sendai 980-8577, Japan

⁵International Center for Synchrotron Radiation Innovation Smart (SRIS), Tohoku University,
Sendai 980-8577, Japan

⁶Mathematical Science Center for Co-creative Society (MathCCS), Tohoku University, Sendai 980-8578, Japan

The iron-based superconductor iron selenide (FeSe) has attracted attention due to its unique properties, such as high-temperature superconductivity in monolayer films on SrTiO₃ and strong-coupling superconductivity in BCS-BEC crossover regime in bulk samples, distinguishing it from other iron-based superconductors. Of particular interest in FeSe is the nematic state, where the rotational symmetries of various properties and electronic state decrease from C₄ to C₂. Unlike nematic states in other iron-based superconductors, which typically develop almost simultaneously with antiferromagnetic ordering and tetragonal-to-orthorhombic structural transition, the nematic state in FeSe lacks antiferromagnetic ordering [1]. Moreover, recent x-ray diffraction and angle-resolved photoemission spectroscopy (ARPES) measurements revealed that FeSe thin films grown on LaAlO₃ substrates exhibit nematicity while keeping the tetragonal lattice symmetry [2]. This decoupling of the nematic state from magnetic and structural instabilities provides an excellent opportunity to investigate the origin of nematicity and the interplay between nematicity and superconductivity.

In this study, we conducted ARPES measurements of FeSe/LaAlO₃ to clarify the relationship between superconductivity and nematicity. Since FeSe/LaAlO₃ exhibits superconductivity within the pure nematic state, we tried direct observations of the electronic reconstruction in the nematic state and a superconducting gap below T_c, by utilizing high-energy and momentum resolution capability realized with low-energy photons at BL7U in UVSOR. High quality FeSe/LaAlO₃ samples were prepared by pulsed laser deposition, and the clean surfaces necessary for the ARPES measurements were obtained by cleaving the samples in ultrahigh vacuum. High-resolution ARPES measurements were carried out using an Al spectrometer.

Figure 1 shows ARPES spectra measured in the nematic state along the Γ M high-symmetry line. We observed a holelike dispersion which produces a small pocket centered at the Γ point. We also observed two holelike bands topped at the M point. These holelike bands at the M point are attributed to the Fe 3d_{xz} and

3d_{yz} orbitals. Their energy separation of ~ 50 meV is much larger than the spin-orbit gap of 20-30 meV. Such a large energy separation is the spectroscopic evidence for the occurrence of electronic nematicity. Since the electronic reconstruction in the nematic state has been successfully observed, we next performed high-resolution measurements in the superconducting state.

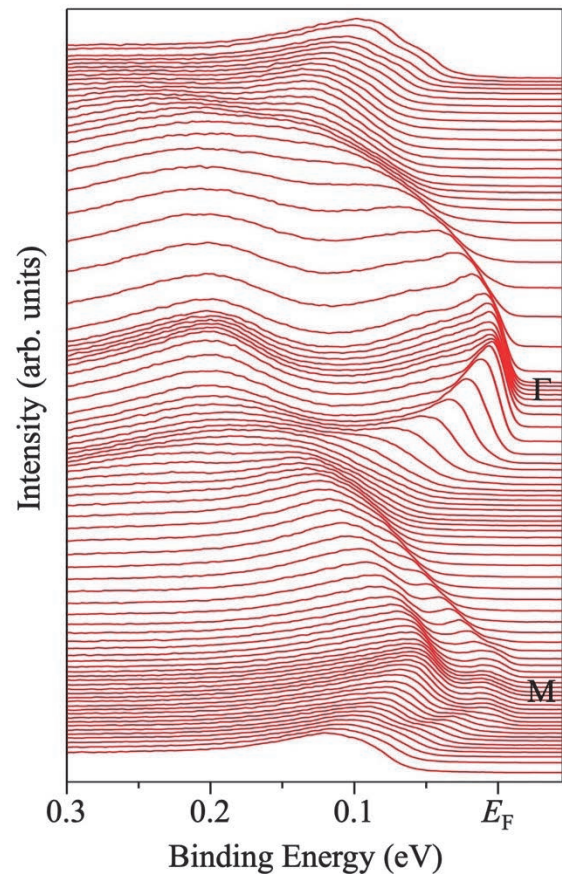


Fig. 1. ARPES intensity along the Γ M cut measured in the pure nematic state of FeSe/LaAlO₃.

[1] K. Nakayama *et al.*, Phys. Rev. Lett. **113** (2014) 237001.

[2] Y. Kubota *et al.*, Phys. Rev. B: Condens. Matter **108** (2023) L100501.

BL7U

High-Resolution ARPES Study of Monolayer Germanene Grown on Ag

T. Terasawa^{1,2}, S. Suzuki¹, D. Katsube³, S. Tanaka⁴ and K. Tanaka⁵

¹Advanced Science Research Center, Japan Atomic Energy Agency, Tokai 319-1195, Japan

²Institute of Industrial Science, The University of Tokyo, Meguro 153-8505, Japan

³Cluster for Pioneering Research, RIKEN, Wako 351-0198, Japan

⁴SANKEN, The Institute of Scientific and Industrial Research, Osaka University, Ibaraki, 567-0047, Japan

⁵UVSOR Synchrotron Facility, Institute for Molecular Science, Okazaki 444-8585, Japan

Based on the angle-resolved photoemission spectroscopy (ARPES), the band structure of germanene, a two-dimensional honeycomb lattice composed of a monatomic layer of Ge atoms, has been discussed so far because of its expected coexistence of ultrahigh carrier mobility and a band gap [1]. However, the germanene sample deposited on Ag(111) substrates showed a defective structure, so the obtained germanene bands were diffuse even in the best ARPES in the earlier reports [2]. In 2018, J. Yuhara and colleagues introduced a novel germanene preparation method. This process involves the segregation of germanene on Ag(111) thin film on Ge(111) substrate during the annealing and cooling process [3]. The scanning tunneling microscopy images in their report showed that germanene formed on Ag in R30 epitaxial relation together with $7\sqrt{7}\times 7\sqrt{7}$ R19.1 superlattice formation, indicating the long-range order and weak interaction between germanene and Ag surface. As the high-quality sample was realized, the ARPES measurement of the segregated germanene on Ag(111) is required.

Here, we report ARPES measurements of germanene segregated on Ag surfaces. Ag thin films were deposited on Ge(111) substrates at the Japan Atomic Energy Agency. The sample was introduced into the load lock chamber of the BL7U beamline without any preparation. The sample surface was cleaned by repeated Ar⁺ sputtering and annealing. After annealing at 500°C for 30 min, germanene formed on the sample surface, as confirmed by low-energy electron diffraction. ARPES measurements were performed at 8 K using the incident light energy of 8-28 eV.

Figure 1(a) shows the ARPES intensity map on the Γ -M_{Ag} line (equal to Γ -K_{germanene}) of the germanene grown on the Ag surface by 500 °C annealing with the incident light energy of 21.2 eV. As the obtained bands were diffuse, we carried out the second derivation of the ARPES intensity map along the energy direction, as shown in Fig. 1(b). After the second derivation, the electron pocket-like band above -1.0 eV was observed, consistent with the band structure of germanene grown on Al(111) and our results in BL5U [4,5]. In addition, we also observed the hole-like bands below the electron pocket. This is qualitatively consistent with the density functional calculation in the previous report [1]. Note that these diffuse bands were not observed for the so-called “striped phase,” corrugated Ag₂Ge surface alloy grown by 300°C anneal but observed for 500°C anneal samples in 10-28 eV. The second derivatives of the maps resulted in the similar structures. Thus, we

concluded that the obtained bands originate from germanene on Ag. Unfortunately, the Ag bulk bands overlapped around the K point of germanene. Further experiments are required to reveal the band structure of germanene around its K point.

In summary, we performed high-resolution ARPES measurements of germanene segregated on Ag(111) thin films deposited on Ge(111) substrates. The ARPES intensity maps show that the germanene band structure is similar to the DFT-calculated germanene bands. Further analysis and discussion are needed to clarify whether the germanene band structure has a linear band dispersion and band gap.

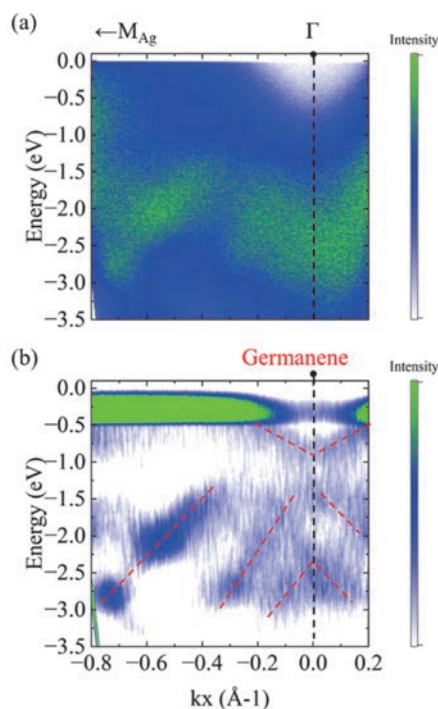


Fig. 1. (a) ARPES intensity map of germanene segregated on Ag thin film deposited on Ge(111) substrates. (b) second derivative along the energy direction of (a). Red dashed lines are eye guides.

- [1] C. C. Liu *et al.*, Phys. Rev. B: Condens. Matter **84** (2011) 195430.
- [2] C. H. Lin *et al.*, Phys. Rev. Mater. **2** (2018) 024003.
- [3] J. Yuhara *et al.*, ACS Nano **12** (2018) 11632.
- [4] J. Yuhara *et al.*, 2D Mater. **8** (2021) 045039.
- [5] UVSOR Activity Report **51** (2024) 97.

Measurement of Valence Band Dispersion in 2-*n*-Octyl-[1]benzothieno[3,2-*b*]naphtho[2,3-*b*]thiophene (2-C8-BTNT) Crystals

T. Tasaki¹, S. Inoue², K. Kikuchi¹, H. Hattori¹, T. Hasegawa² and Y. Nakayama^{1,3}

¹Department of Pure and Applied Chemistry, Tokyo University of Science, Noda, Chiba 278-8510, Japan

²Department of Applied Physics, The University of Tokyo, Tokyo 113-8656, Japan

³Institute for Molecular Science (IMS), Okazaki 444-8585, Japan

Organic semiconductor devices including organic solar cells and organic transistors are expected to find applications due to their advantages such as lightness, mechanical flexibility, and printability [1,2]. It has been reported that materials exhibiting band-like transport, rather than intermolecular hopping, lead to charge carrier mobility of high levels for organic semiconductor devices [3]. To understand the transport nature, it is essential to the nature of the conduction mechanism of such organic semiconductor materials. 2-*n*-Octyl-[1]benzothieno [3,2-*b*]naphtho[2,3*b*]thiophene (2-C8-BTNT) (Fig. 1) was reported to exhibit high charge carrier mobility of over $10 \text{ cm}^2\text{V}^{-1}\text{s}^{-1}$ in its single-crystal field-effect transistors [4]. In this study, angle-resolved photoelectron spectroscopy (ARPES) experiments were performed to measure the valence bands of the 2-C8-BTNT crystals.

2-C8-BTNT crystals were prepared by a drop-casting method, one of the solution growth methods, from its chlorobenzene solution of 0.5 mg/mL on Au-coated Si substrates under a solvent atmosphere at room temperature. The ARPES measurements were performed at BL7U of UVSOR-III. The photon energy was set at 8 eV, and laser light (wavelength of 375 nm) was illuminated on the sample for the cancellation of the sample charging during the photoelectron spectroscopy measurements. The emission angle θ is defined as 0° when the sample was facing normal to the analyzer and as positive when the surface was rotated toward the synchrotron light source. The range of photoelectron emission angles that can be collected by the analyzer at $\theta = 0^\circ$ was approximately $\pm 16^\circ$. The ARPES measurements were performed in the θ range from -10° to $+40^\circ$ for every 5° , and eleven ARPES spectra obtained were integrated to map out a resulting total ARPES data in a photoelectron emission angle range from -26° to $+56^\circ$ used in the analysis.

Figure 2 shows the ARPES results of 2-C8-BTNT in the Γ -X direction taken at room temperature. In an energy-wavenumber (E - k) region shown in yellow, the spectral features shifted to the deeper binding energy side as moving from the Γ point to the X point. This indicates that the energy dispersion of the valence was successfully measured. The observed band width seemed to be larger than the previously reported energy dispersion of the single crystal rubrene (approximately

0.5 eV [3]). In the future, we plan to investigate in detail the valence band structures of 2-C8-BTNT and the temperature dependence to elucidate relationships with the transport properties and electron-photon (vibration) couplings.

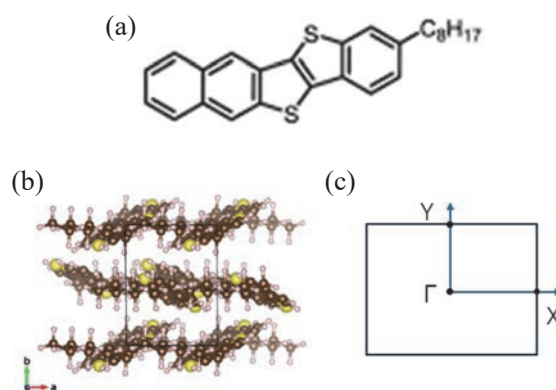


Fig. 1. (a) Molecular structure, (b) single-crystal molecular arrangement in the crystal ab plane ($a = 6.019 \text{ \AA}$, $b = 7.878 \text{ \AA}$ [4]), and (c) surface Brillouin zone of 2-C8-BTNT.

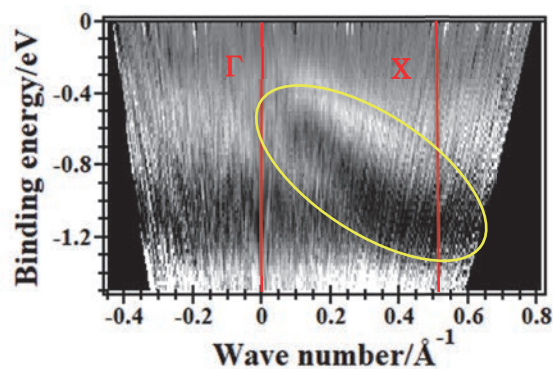


Fig. 2. ARPES d^2I/dE^2 (where I is photoelectron intensity) map of the 2-C8-BTNT crystal plotted on the E - k plane in the Γ -X direction (black: negative d^2I/dE^2 , white: positive d^2I/dE^2).

- [1] H. Minemawari *et al.*, Nature **475** (2011) 364.
- [2] J. Mei *et al.*, J. Am. Chem. Soc. **18** (2013) 6724.
- [3] Y. Nakayama *et al.*, J. Mater. Chem. C. **8** (2020) 9090-9132.
- [4] S. Inoue *et al.*, Chem. Sci. **11** (2020) 12493.

BL7U

Orbital-Resolved Observations of Molecular Electronic Structures and Many-Body Interactions in Rubrene Single Crystal

K. Fukutani^{1,2}, F. Nishino², P. I. Jaseela², N. Kasuya³, J. Takeya³, S. Makita¹,
K. Tanaka^{1,2} and S. Kera^{1,2}

¹Institute for Molecular Science, Okazaki 444-8585, Japan

²The Graduate University for Advanced Studies (SOKENDAI), Okazaki 444-8585, Japan

³Graduate School of Frontier Science, University of Tokyo, Chiba 277-8561, Japan

Recent developments in the field of functional organic molecular semiconductors have rapidly expanded the realm of organic materials into practical device applications, and they play an indispensable role in our electronic industry today, owing to their physical flexibility, low cost of fabrication, high biodegradability in the environment, as well as the abundance of the constituent elements (mostly carbon and hydrogen) that are, in principle, inexhaustive.

Among such organic semiconductors, rubrene ($C_{42}H_{28}$) is known for its particularly high hole carrier mobility ($40 \text{ cm}^2/\text{Vs}$ [1]) and is considered one of the most important organic semiconductor materials for the future of organic electronics. However, despite its success in various device applications, our knowledge of their electronic structure, one of the most fundamental building blocks for understanding and controlling their properties, is far from complete.

In fact, various experimental investigations on the electronic band structures of rubrene have reported qualitatively different results [2] and the true band structure of this material remains elusive.

In the crystal structure of rubrene, it is known that a unit cell is occupied by two rubrene molecules, and hence its band structure must exhibit two distinct electronic states (bands), arising from bonding and anti-bonding phase relations of the molecules. Furthermore, these two electronic states must be degenerate at the Brillouin zone edge (e.g., X and Y points) due to the crystal symmetry.

However, the electronic band structures reported from various experiments show either a single band or two bands that are qualitatively inconsistent with the rubrene crystalline symmetry. Thus, in our study, we performed a series of polarization-dependent high-resolution angle-resolved photoemission spectroscopy (ARPES) to investigate the orbital-resolved band structure of rubrene single crystal.

Figure 1 shows the results of our ARPES measurements (second derivatives) using photons with linear horizontal, vertical, and circular polarizations. It can be seen that in the horizontal and vertical polarization, two distinct bands exhibiting different dispersion widths can be seen. Furthermore, in the circular polarization, both of these two bands are observed and they appear to be degenerate near the

Brillouin zone edge, at the Y point.

Such band structure is fully consistent with the previous band structure calculations [3] predicting the presence of the two bands arising from the bonding and anti-bonding molecular orbitals. Our detailed analysis using the photoemission selection rules also reveal the electronic symmetries of the observed two bands in the horizontal and vertical polarizations are consistent with the orbital symmetries of anti-bonding and bonding electronic states, respectively.

Furthermore, our results also show the presence of the intra-band gap, known to arise from the coupling between the electrons and the molecular vibrations, in both of the bands. Thus, our results not only resolve the long-standing discrepancy between the calculated and the observed band structures, but also opens up a pathway to further understand the many-body interactions in organic molecular semiconductors.

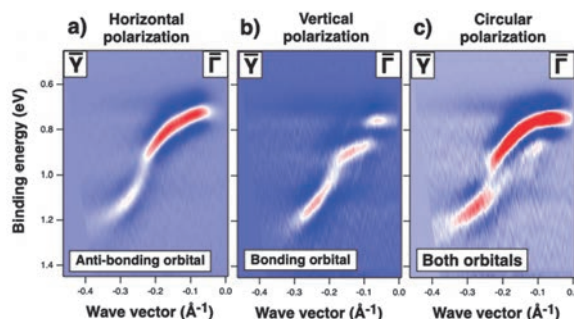


Fig. 1. The results of polarization-dependent ARPES measurements (second derivative plots) for rubrene single crystal, using (a) linear horizontal, (b) linear vertical, and (c) circular polarizations. The measurements were performed at $h\nu = 8 \text{ eV}$.

- [1] J. Takeya *et al.*, Appl. Phys. Lett. **90** (2007) 102120.
 [2] S. Machida *et al.*, Phys. Rev. Lett. **104** (2010) 156401.; H. Ding *et al.*, Appl. Phys. Lett. **96** (2010) 222106.; Y. Nakayama *et al.*, Appl. Phys. Express **5** (2012) 111601.; A. Vollmer *et al.*, J. Electron Spectrosc. Rel. Phenom. **185** (2012) 55.; F. Bussolotti *et al.*, Nat. Commun. **8** (2017) 173; J. Nitta *et al.*, Sci. Rep. **9** (2019) 9645.
 [3] S. Yanagisawa *et al.*, Phys. Rev. B: Condens. Matter **88** (2013) 115438.

Excitation Spectra and Decay Curves of Plastic Scintillators with VUV Excitation

M. Koshimizu

Research Institute of Electronics, Shizuoka University, Hamamatsu 432-8011, Japan

Plastic scintillators are composed of polymer host and organic phosphors. The scintillation process in the plastic scintillators is described as (1) ionization of the host polymer, (2) recombination of the ionized polymer to form electronic excited states, (3) excitation energy transfer from the host polymer to the organic phosphors, and (4) luminescence of the organic phosphors. In general, the scintillation light yields of plastic scintillators are significantly lower than those of commercially available inorganic scintillators. A main cause of the lower scintillation light yields of plastic scintillators is low energy transfer efficiency at the stage (3).

Prior to the stage (3), two kinds of excited states are formed upon recombination at the stage (2): singlet and triplet excited states. Among them, triplet excited states are not effectively used because of the two reasons: one is low energy transfer efficiency from the host to the organic phosphors. For the singlet excited states, the excitation energy is transferred to organic phosphors via dipole-dipole interaction, which is a long-range interaction. On the contrary, the triplet excited states have low energy transfer efficiency because of the short range of the exchange interaction, which is responsible for the energy transfer of the triplet excited states. There was a small number of examples of the analysis of the contribution of the triplet excited states.

Recently, we found that the excitation spectra of plastic scintillators had a characteristic feature representing formation of multiple excitations and triplet excited states [1]. In this study, we further explored the analysis with VUV excitation based on decay curve measurements.

Polystyrene-based plastic scintillators containing DPO and POPOP as the organic phosphors at different concentrations were used as the samples. The photoluminescence decay curves were obtained using a time-correlated single photon counting technique at BL7B of UVSOR operated in a single bunch mode. The photoluminescence decay curves at 60–210 nm were obtained.

The photoluminescence decay curves of the plastic scintillators are presented Figs. 1 and 2. For all the excitation wavelengths, the polystyrene host is initially excited. The slow decay component originates from triplet-triplet annihilation, which results in a delayed formation of singlet excited states. With excitation at 210 nm, the decay behaviors were the fastest among the surveyed excitation wavelengths. The decay became

slower with excitation at 180 nm, and subsequently became faster at 150 nm. This is in line with the excitation spectra [1]. The former change can be explained by the enhanced formation probability of the triplet excited states. On the contrary, the latter change can be explained with the enhanced formation probability of the singlet excited states with multiple excitation formation. Further shortening of the excitation wavelength resulted in slow decay curves. These results strongly suggest that the formation probability of the triplet excited states has a complicated formation spectrum in the VUV region, which in turn can be an effective tool to analyze the contribution of the triplet excited states.

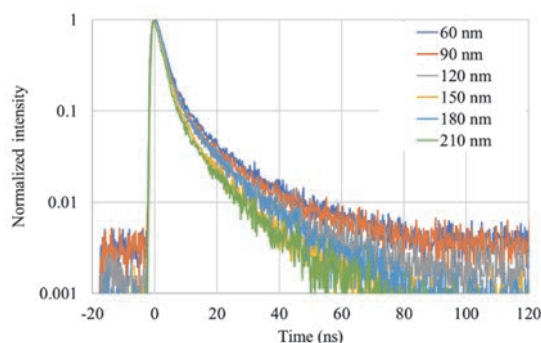


Fig. 1. Photoluminescence decay curves of polystyrene-based plastic scintillators containing DPO and POPOP as organic phosphors at 0.5 wt%.

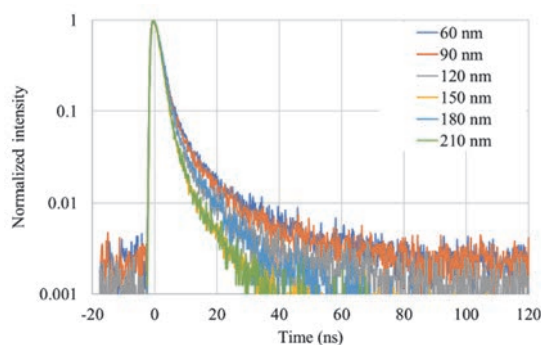


Fig. 2. Photoluminescence decay curves of polystyrene-based plastic scintillators containing DPO and POPOP as organic phosphors at 2.0 wt%.

[1] M. Koshimizu, Y. Fujimoto and K. Asai, UVSOR Activity Report **50** (2023) 112.

BL7B

Vacuum Ultraviolet Characterization of Li-Glass as a Potential Neutron Scintillator

T. Shimizu, K. Shinohara, K. Yamanoi and N. Sarukura

Institute of Laser Engineering, Osaka University, 2-6 Yamadaoka Suita, Osaka 565-0875 Japan

In fusion research, neutron detection is important for evaluating efficiency and safety. There are different types of neutrons produced, but primary neutrons in particular are easily detected with conventional plastic scintillators due to their large quantity. On the other hand, scattered neutrons are detected later than X-rays and primary neutrons generated by nuclear reactions, and their quantity is much lower than that of primary neutrons, making the measurement of scattered neutrons difficult. Therefore, a scintillator with high sensitivity to scattered neutrons and fast response that quickly attenuates X-ray and primary neutron signals is needed.

Scattered neutron energies range from 0.2 to 0.6 MeV. For neutrons of this energy, ${}^6\text{Li}$ has a large absorption cross section. ${}^6\text{Li}$ has long been widely used as a glass scintillator for thermal neutrons, and glasses containing ${}^6\text{Li}$ and doped with Ce as a luminescent material are now in practical use. The conventionally used Li glass scintillators are $\text{Li}_2\text{O-SiO}_2$ glass doped with Ce_2O_3 (GS2, GS20, KS20, etc.). Neutrons are generally measured by time-of-flight (TOF), and this technique requires a time resolution of 25 ns to separate the signal from the transient neutrons. However, the emission lifetime of GS2, GS20, and KS20 is 50-70 ns, which does not meet this requirement.

To solve this problem, a scintillator using $20\text{Al}(\text{PO}_3)_3\text{-}80\text{LiF}$ (APLF) glass as a base material was developed instead of $\text{Li}_2\text{O-SiO}_2$. Shortening the emission wavelength is effective in shortening the lifetime of luminescence. APLF is an excellent base material for short wavelength scintillators because of its high transparency in the ultraviolet region and no risk of self-absorption. Therefore, we have succeeded in shortening the lifetime of APLF by using Pr^{3+} instead of Ce^{3+} , which is a commonly used luminescent nucleus, and by shifting the emission wavelength to the short wavelength side (Ce^{3+} : 300~350 nm \rightarrow Pr^{3+} : 250~300 nm).

Although APLF is excellent candidate for scintillators for scattered neutrons, there are other candidates for lithium-based glasses. We are currently developing lithium glasses with new compositions under a collaborating researcher, and characterization of scintillators using these glasses is currently underway.

In this study, we have prepared new lithium glasses with Pr luminescent nuclei such as $20\text{Li}_2\text{O-}20\text{CaO-}60\text{SiO}_2\text{+}0.3\text{Pr}_2\text{O}_3$ (LCSO+0.3Pr), $30\text{Li}_2\text{O-}70\text{B}_2\text{O}_3\text{+}$

$0.3\text{Pr}_2\text{O}_3$ (LBO+0.3Pr) and $30\text{Li}_2\text{O-}60\text{P}_2\text{O}_5\text{-}10\text{Al}_2\text{O}_3\text{+}0.3\text{Pr}_2\text{O}_3$ (LPAO+0.3Pr) and characterized.

Since the luminescence and absorption are in the VUV to UV region, we will use the UVSOR VUV line to obtain luminescence and absorption spectra and evaluate at what wavelengths they should be designed for use as scintillators. The emission and excitation spectra were obtained at the BL7B beamline. Each glass was placed inside a vacuum chamber maintained at 10⁻⁶ Pa and was excited by wavelengths chosen using the beamline's 3-m normal incidence monochromator that has a dynamic range from 50 nm (VUV) to 1000 nm (IR). The emission was then fibered to an Acton SpectraPro-300i spectrometer coupled with a liquid N_2 -cooled PyLoN 400BR_eXcelon charge-coupled device (CCD) camera for emission spectroscopy and with a photomultiplier tube (PMT) for excitation spectroscopy.

Figure 1 is an example of the measurement results and shows the transmittance in VUV of new samples. Among the samples measured this time, the one with LPAO showed promising results, so we will prepare samples with different concentrations of Pr for further optimization. We are currently compiling the analysis and discussion of the X-ray absorption near edge structure (XANES) spectroscopy for the presence of Pr ions in the glasses with a oxidation state.[1]

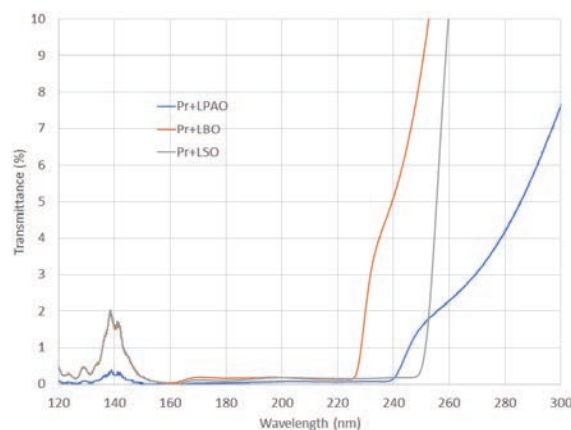


Fig. 1. Transmission spectra of Li-glass.

[1] K. Shinohara *et al*, the 9th International Symposium on Optical Materials (IS-OM'9), Tarragona (Spain), from June 26 to 30, 2023.

UVSOR User 4

